EFFECTS OF PRINT PARAMETERS AND HEAT TREATMENT ON FATIGUE OF LASER POWDER BED FUSED INCONEL 718

A Thesis

by

ANTHONY PHILIP MARINO

Submitted to the Graduate and Professional School of
Texas A&M University
in partial fulfillment of the requirements for the degree of

MASTER OF SCIENCE

Chair of Committee,	Bryan Rasmussen
Committee Members,	Miladin Radovic
	Justin Wilkerson
Head of Department,	Guillermo Aguilar

December 2022

Major Subject: Mechanical Engineering

ABSTRACT

Laser Powder Bed Fusion (L-PBF) allows for complex geometry parts to be fabricated without sacrificing mechanical properties/behaviors. Though this process is greatly beneficial, it is still hindered by its build volume capabilities as well as the present of detrimental particles and defects in its microstructure after the printing process. This research applies to the printing parameters and post processing of L-PBF'ed Inconel 718 (IN718) and their effect on fatigue performance of the material. Samples were printed with laser speed varying from 1000-1500 mm/s while varying energy density per volume from 45.5-68.2 J/mm^3. Samples were grouped and subject to different heat treatment (HT) combinations including homogenization (HG), hot isostatic pressing (HIP), and solution aging (SA). The porosity and microstructures of the samples were analyzed through optical and scanning electron microscopes (OM and SEM, respectively) to determine optimal print parameter and heat treatment strategy. The lowest amount of porosity with the smallest average pore diameter (15.58μm) was observed in samples printed with 54.5 J/mm^3 energy density. Laves phase particles were present in both as-printed and HG samples. Al_2O_3 defects were present in all samples but were controlled in samples subjected to the SA treatment. HIP+SA samples exhibited optimal microstructure and grain boundary development. Fatigue results showed the HIP+SA was able to increase fatigue life >100% when compared to the as-printed state.

ACKNOWLEDGEMENTS

I would like to thank my committee chair, Dr. Bryan Rasmussen, and my committee members, Dr. Justin Wilkerson, and Dr. Miladin Radovic, for their guidance and support in my defense of this research. Dr. Wayne Hung also played an important role in my career at A&M by giving me an opportunity to develop as a researcher as he guided this project. I will always be grateful for the opportunity he gave me as well as the help he gave along the way. I would also like to thank Shyam Balasubramanian for giving me advice and support during my time at A&M, I am not too sure where I would be if he had not been so willing to help me over these last two years. I am also very thankful for the opportunity to teach the Manufacturing and Assembly Processes Lab here at A&M and it has led me to a deeper appreciation for educators and the students as well. I have to thank Alejandro Mendez, Andrew Russell, Trenton Schoonmaker, Keelan Lindsey, Aren Davis, Michael Craig, Sai Raghava Bhargavi Suri, and all of the other student workers that I have had the pleasure of working with for the past two years.

Thanks also go to all of my friends and the faculty members that supported me at Auburn University. A huge part of my career is owed to the AUBE Lab and all of the members. Dr. Michael Zabala has been an exceptionally large factor in the development of my interests, and he opened a lot of doors for me to succeed. I also owe a lot of thanks to Jacob Larson for taking the time to put up with me for two years. I found my true interests while working in that lab and it will always hold a special place in my heart.

I would also like to thank some of my close friends for being there for me throughout my life. Mitchell Ledbetter has been my best friend since fourth grade, and I

am beyond lucky to have had him by my side since then. He and his family have become my second family and I love and respect all of them so much. He and I have always been motivated to work hard and be successful in life while always entertaining the idea of working together one day, in whatever industry or field that may be. Going to different schools or living in different states has never and will never cause us to lose contact with each other and we will always find a way to hang out, whether it's just timing home visits perfectly or planning three day trips to Atlanta to see Uncle Tommy that end up lasting six. I also need to mention Henry Kendrick for being an amazing friend. He doesn't really know how to respond over text but that has never gotten in the way of us reconnecting as if we had just seen each other last the day before. I am really lucky to have both him and Mitch in my life. Thanks are also very necessary for all of my roommates throughout my time at Auburn: BF Daves, Ben DiPiazza, Katie Moore, Sam Norton, Bay Robinson, and my cousin Kate. You are all responsible for some of my favorite memories at Auburn from Rock Band, gameday mornings, being locked out (238 forever), and trying to scare my cousin every time she opened the front door to come home. For my friends in PT, thank you for the best year and a half of my college career. I always say that I wish I could've met them all a lot sooner, but I am still so thankful to have had the time that I did with all of them. I'll always be looking forward to the next spring break trip or burning man experience at Genelda. Out of that group I have to thank the Pilates Pals: Adam Hoesley, Connor Weldon, and J.P. Steele are best friends that I left Auburn with, and I will always appreciate them. As for my friends that made the wrong decision and went to Alabama, I am also very thankful for them even with that fault in mind. JoJo Meineke has been a brother of mine since our days at OLV and he has always been there for me when I needed it most. A huge thank you goes to my absolute favorite duo: Cecilia Ragusa and Anna Runyan. They have both been with me since freshman year of high school and I am hoping that I am lucky enough to keep them with me for an exceptionally long time. This same sentiment goes to Camryn Lyster. Through my fear of her and her subtle hatred of me, we have developed one of my favorite friendships that has kept me sane throughout any challenging times I’ve had. Lastly, I have to thank Jordan Zarzaur, not only because he has been a great friend to me since high school, but mainly because I think I would get in trouble if he found out that I didn’t mention him at all.

Finally, I would not be where I am or who I am today without my family. My parents have allowed me to pursue any and every path that I have wanted to pursue, and they have done it with the utmost support and love. I am extremely lucky to have had the freedom that I did have and the comfort in knowing that they had my back no matter what I decided to do with my life. I hope that I have done them justice and made them proud of who I have become and what I have been able to accomplish in my life so far, I really owe every single ounce of success to them. I also owe a lot to my amazing grandparents. Both of my grandmothers have shown me so much love and support throughout my life and I am incredibly lucky to have been able to spend so much time with them. Outside of my parents, I owe the greatest thanks to my grandfather. My initial interest in engineering came from the time that I spent with him growing up. He has taught me so much and I have always admired his desire and ability to learn so much about so many things. Being the only male grandchild on my dad’s side of the family, my grandfather taught me what it meant to always put in hard and respectable work no matter what it was that I was doing. Even if I didn’t realize it at the time and I was complaining, he instilled values in me that have gotten me to where I am in life and I plan to take them with me forever. To my favorite sister, I also owe her a great amount of thanks for being an amazing role model. Whether she was aware of it or not, her success in her career as a student and now in her work has shown me that I am also capable of success if I put in the work. When she moved to Pennsylvania for graduate school, it showed me that I could do the same when I left Auburn, and it made me so much more comfortable in my decision to move to Texas.

I really owe everything to the people that I have mentioned here, and even to those that I did not mention specifically. I have been incredibly lucky to be surrounded by the people I have in my life, both family and friends, and I can only hope that I can hold on to these people and these relationships throughout my life.

CONTRIBUTORS AND FUNDING SOURCES

Contributors

This work was supervised by a thesis committee consisting of Dr. Bryan Rasmussen and Dr. Justin Wilkerson of the Department of Mechanical Engineering, and Dr. Miladin Radovic of the Department of Material Science and Engineering.

Dr. Rodney Inmon of the Department of Aerospace Engineering assisted in the fatigue testing and Dr. Stanislav Vitha of the Microscopy and Imaging Center aided in the gold coating and the use of the SEM and EDS systems.

Funding Sources

This work was also made possible in part by Knust-Godwin SBO out of Houston, Texas, as they provided the Laser Powder Bed Fused samples and other fabrication services.

NOMENCLATURE

AM	Additive Manufacturing
ASTM	American Society for Testing and Materials
EBW	Electron Beam Welding
EDM	Electrical Discharge Machining
EDS	Energy Dispersive Spectroscopy
HAZ	Heat Affected Zone
HT	Heat Treatment
HIP	Hot Isostatic Pressing
IN718	Inconel 718
L-PBF	Laser Powder Bed Fusion
OM	Optical Microscope
RH	Rockwell Hardness
SEM	Scanning Electron Microscope
SLM	Selective Laser Melting
SA	Solution Aging
SR	Stress Relieved
UTS	Ultimate Tensile Strength
VH	Vickers Hardness
YS	Yield Strength

TABLE OF CONTENTS

Page

LIST OF FIGURES

Page

LIST OF TABLES

Page

1. INTRODUCTION

Additive manufacturing (AM) allows for the fabrication of complex geometries while avoiding labors of traditional subtractive machining processes. Among the prominent AM technologies used for fabrication of metal components, laser powder bed fusion (L-PBF) has become one of the most common across aerospace, automotive, energy, and nuclear industries. L-PBF is a process that allows for the production of near net-shaped parts while limiting the constraints in the design of complex geometry components. Though greater freedom is achieved in the geometric capabilities of fabrication, the largest constraint on production of L-PBF'ed parts is found in the chamber size in powder bed fusion machines. Because of this restriction in component volume, the L-PBF process is not able to fulfill requirements for larger components of complex geometry that are desired by the above mentioned industries. The study of effective ways to join smaller L-PBF'ed components has been conducted before, but with little success in terms of the mechanical performance of the material. To fully take advantage of the benefits of the L-PBF process, it is necessary to further investigate the microstructure of L-PBF'ed materials in an attempt to optimize performance.

Inconel 718 (IN718) is a nickel-based super alloy that has become a prominent material across a wide range of industry applications. The combination of a superior high-temperature mechanical strength and corrosion resistance only support this. Because this alloy is found in such a variety of applications, there is a need to be able to fabricate complex geometries that can be difficult through traditional manufacturing methods on such a strong material. Though taking advantage of L-PBF in the fabrication of IN718 parts can solve an issue in creating elaborate geometry, the rapid heating and cooling during the L-PBF process can lead to the development of brittle phases and defects that can hinder proper grain boundary development. Due to this factor, it is necessary to understand the effects of the L-PBF process parameters on the material as well as to implement post-processing methods to remove detrimental particles/defects and improve the mechanical properties of L-PBF IN718 to meet the ASTM standard. The objectives of this research are:

1. To optimize L-PBF print parameters for reduction in porosities/defects present after fabrication.
2. To evaluate heat treatment strategies' effects on microstructural development.
3. To compare fatigue performance to as-printed L-PBF IN718.
4. To identify issues for future work and improvement.

2. LITERATURE REVIEW

The IN718 superalloy has characteristics of high strength and corrosion resistance that make it a desirable choice for various industries. The components of the alloy's composition led to the development of proper strengthening phases in the microstructure during solidification that allow for these superior properties. The chemical composition of IN718 is outlined in Table 2.1.

Table 2.1 Chemical composition of IN718 (wt%), adapted from [1]

Ni	Cr	Fe	Nb	Mo	Ti	Al	C	Co	Cu	Si	Mg
50-55	17-21	~17	4.75-5.5	2.8-3.3	0.65-1.15	0.2-0.8	<0.8	<1.0	<0.3	<0.35	<0.35

IN718 components fabricated by AM methods have gained popularity as the field has evolved and advanced in terms of technology over the past 15 years. Specifically, L-PBF of IN718 has been studied widely in research along with the effects of process parameters on the quality of the printed samples. Along with the L-PBF process parameters, post-processing techniques have been studied including homogenization, hot isostatic pressing (HIP), solution treatments, and aging/dual aging treatments to further improve the quality of these components by reducing the number of detrimental phases and particles within the material matrix. The joining of IN718 has also been studied through a variety of joining methods by many researchers. Electron Beam Welding (EBW) has become prominent in studies involving the joining of IN718. Other methods, such as laser welding and tungsten inert gas welding, have been investigated for the joining of L-PBF'ed materials to satisfy the growing need for large parts of complex geometry, but only one study has explored EBW of L-PBF IN718.

2.1. Microstructure of IN718

IN718 was developed to provide high strength and tensile properties in various temperature conditions. The alloying elements in IN718's composition are responsible for providing favorable properties to the metal, with Ni, Fe, and Mo yielding solid-solution strengthening in the γ-matrix, C contributing to the formation of carbides, and Al, Ti, and Nb forming strengthening precipitates γ' and γ'' [2,3]. The γ' and γ'' phases were found on the grain boundaries of IN718 and were found to be responsible for the high temperature strength property. Laves and δ phase particles were extremely brittle and weakened the IN718. All these phases consisted of Niobium and shared the Nb present in IN718 material matrix. With the dissolving of the prime phases, the Nb was absorbed by the weakening phases. With the introduction of additive manufacturing (AM) processes such as L-PBF, further heating of the adjacent regions within the material led to aging of γ phase to form δ precipitates, which resemble Laves phase in its segregation of Nb, as well as other γ' and γ'' precipitates [4]. Improper precipitation of these particles reduces the strength properties of the material. AM processes also increase the propagation of other defects such as porosities, cracks, and lack-of-fusion defects [5–7].

2.1. Laser Powder Bed Fusion of IN718

To fully understand formation mechanics of porosity and other defects that are detrimental to the mechanical performance of a material, it is necessary to investigate the effects of energy density and process parameters on these formations. Because defects can have an effect on the surface level as well as a volumetric effect, the following equations (1,2) have been used to analyze the effects of print parameters on porosity development and distribution:

$$ED = \frac{P}{H\,S\,T} \qquad (1)$$

$$LED = \frac{P}{S} \qquad (2)$$

where ED is energy density (J/mm^3), LED is linear energy density (J/mm), P is the laser power (W), H is the hatch distance (mm), S is the scanning speed (mm/s), and T is the layer thickness (mm).

Volumetric Energy Density (VED) was investigated to relate print process parameters to mechanical and surface properties of L-PBF IN718 and was calculated using Equation (1) [8]. Cylindrical samples (40mm diameter x 20mm height) were printed with varying laser power, laser speed, and hatch distance to produce a range of VED from 23-480 J/mm^3. The surface roughness of the top of the samples was measured in the following three directions: along the scanning direction during printing, along the hatch direction, and a 45º-tilted direction with respect to the first two. Vickers microhardness values were obtained on polished surfaces with a load of 300 gf and 10 sec dwell time. The surface roughness and number of pores reduced with an increasing VED until reaching the far bound of 480 J/mm^3 where the number of pores showed an increase. Higher Vickers microhardness values were also achieved in the middle of the VED spectrum evaluated around 46-90 J/mm^3. A study on 316L stainless steel supported these findings where VED was varied by 75 J/mm^3 on either side of the manufacturer standard [9]. The porosity decreased from 8.84% to 0.38% when VED increased from 41.81 J/mm^3 to 104.52 J/mm^3. When increased again to 209.03 J/mm^3, porosity increased to 6.51%. Both studies also showed similar detrimental results in terms of porosity and microhardness occurring at both the lower and upper bounds of VED values, proving that a severe increase in VED can reintroduce voids and soften the material [8,9].

2.2. Microstructural Defects

Many studies have investigated the causes for weakened mechanical properties in both wrought and additive manufactured IN718. Laves phase formation has been shown to be dependent on Nb segregation and the cooling rate during the metal forming process, as well as during welding processes, with a γ/Laves phase eutectic occurring at roughly 1200ºC [3,10–12]. The effect of Laves phase was studied in wrought IN718 and it was shown that the presence of the Nb-rich Laves phase reduced the elongation of the material well below the AMS 5663 minimum requirement [13]. It was found that when Laves is present in a more continuous manner within the matrix, it acts as a preferred crack propagation site that greatly reduces the fatigue life of the material through increased crack growth rates. This same study also produced high temperature tensile results that observed an increase in elongation with the temperature increase in samples where Laves was present. Samples subject to HIP at 1107ºC/103 MPa/2 h contained gross amounts of Laves where HIP at 1191ºC/103 MPa/4 h resulted in a Laves-free matrix. The room temperature results from this study showed reductions in tensile properties with the presence of Laves.

The formation of the brittle δ phase was studied during post-processing heat treatments of L-PBF IN718 [14,15]. Kuo et al. investigated one sample group with solution treatment at 980ºC for 1 h, followed by air cooling (AC), and a dual aging treatment consisting of 718ºC for 8 h, furnace cooling (FC) to 621ºC, holding at 621ºC for 10 h, and AC to room temperature and another subjected to direct aging with no solution treatment. Solution and aged samples produced strength values comparable to those of wrought IN718 at both room temperature and 650ºC. Gao et al. applied solution and aging treatments according to the parameters in Table 2.2.

Table 2.2 Heat treatment schemes for IN718 [15]

Solution Treatment	Dual Aging Treatment
1080ºC * 1.5 h, FC	720ºC * 8 h, FC at 55ºC/h to 620ºC * 8 h, FC
980ºC * 1 h, FC	720ºC * 8 h, FC at 55ºC/h to 620ºC * 8 h, FC
1080ºC * 1.5 h, FC + 980ºC * 1 h, FC	720ºC * 8 h, FC at 55ºC/h to 620ºC * 8 h, FC

Treatments conducted at 1080ºC were almost free of δ phases, as the dissolution temperature of the phases is around 980ºC-1020ºC. Treatment at 980ºC was not sufficient for complete diffusion of Nb precipitates. 1080ºC and 1080ºC + 980ºC samples exhibited higher strength properties. Though, both studies obtained tensile results of severely reduced elongation with the presence of δ phases. These phases along the grain boundaries allowed for dislocations adding up during the tensile testing [15]. Laves phase particles were also shown to be deleterious in IN718 fabricated by selective laser melting (SLM), followed by EBW [3]. These particles were detected after tensile testing in high concentrations at areas of failure propagation, along with Nb-rich carbides.

The porosity and defect propagation in metals fabricated by L-PBF processes were investigated in attempts to understand their origins. These defects (including metallic carbides, unfused layers, and unmelted particles) that were present in the as-built state of the material can lead to poor fatigue performance [16,17]. Many studies related the amount of porosity present in the material to the scanning speed during printing [8,9,18,19]. Other defects, such as aluminum oxides (Al_2O_3), were observed but in far less studies. Al_2O_3 defects were observed in both circular porosity form and less uniform states after L-PBF of IN718 [11,20,21]. It was suggested that these oxides were a result from using recycled IN718 powder and formed on the surface of the powder during previous printing operations. These oxides were found to be unavoidable during the formation of L-PBF IN718 [21].

2.3. Post Processing

The high temperatures achieved in the L-PBF process along with the rapid cooling rates create numerous factors that hinder the mechanical performance of IN718. Because of this, many studies have chosen to focus on the effects of different heat treatment processes to remove, or reduce, these brittle phases, pores, defects, etc. Some studies have analyzed the effects of combining multiple heat treatment process to evaluate their ability to remove detrimental particles and improve mechanical properties [15,22–25]. Standard specimens underwent solution treatment at 980ºC followed by an aging treatment and was evaluated against other specimens with additional homogenization treatment (1080ºC + aging at 720ºC for 8 hours + furnace cooling + 620ºC for 8 hours air cooling) [22]. Microstructural results under an SEM showed that several-step heat treatment was necessary to eliminate Nb segregation and relieve the residual stress. The standard group exhibited greater strength (1090 MPa tensile strength) with lower elongation (7.8%) than the homogenization group (1005 MPa tensile strength and 10.7% elongation). Solution treatment at 1080ºC produced far more suitable results than the standard treatment at 980ºC, as it was observed that treatment at 980ºC was not sufficient enough for the dissolution of Laves phase; this was supported by other studies [15,25,26]. Another study observed that a single homogenization treatment at 1080ºC was not enough to dissolve Laves phase [27]. Though this study still observed the presence of Laves, other studies support that homogenization at 1080ºC followed by standard solution treatment and aging will produce the highest tensile strength of the material [24,25].

Hot isostatic pressing (HIP) has been studied for similar applications as homogenization treatments as well as being used as an aid in reducing porosity and other defects. One study compared samples after fabrication by SLM, standard heat treatment at 850ºC and HIP at 1180ºC, separately, and a final group that was both HIP'ed and heat treated (homogenization at 1065ºC followed by aging at 760ºC) with cast and wrought IN718 [28]. Laser power also varied between 250W and 950W. Samples that underwent a HIP treatment exhibited improvement in the mechanical properties of the material due to the dissolution of Laves and δ phase particles while reducing porosity density. These improved mechanical properties were exceeded by the samples with additional treatment after HIP with those properties being superior to the wrought IN718 material, as shown in the following Table 2.3. Another study compared HIP samples of IN718 at 1163ºC with homogenized samples at 1080ºC [29]. Microstructure analysis showed that both HIP and homogenization are capable of the dissolution of detrimental phases while promoting the growth of strengthening carbides along the grain boundaries. These results were supported by previous work [30].

Table 2.3 Tensile Properties at Room Temperature [28]

Sample name and laser source	Yield strength 0.2%, (MPa)	Elongation (%)	Tensile Strength (MPa)	Hardness, (HV_{1kgf})
		As processed		
Cast	488	11	752	353
Wrought	916	17	1055	353
SLM (250W)	668 ± 16	22 ± 2	1011 ± 27	320
SLM (950W)	531 ± 9	21 ± 5	866 ± 33	287
		SLM + Annealing		
250W	875 ± 11	17 ± 2	1153 ± 4	360
950W	668 ± 7	7 ± 2	884 ± 80	338
		SLM + Hot isostatic pressing		
250W	645 ± 6	38 ± 1	1025 ± 14	310
950W	481 ± 11	34 ± 3	788 ± 12	262
		SLM + Hot isostatic pressing + Homogenization		
250W	1145 ± 16	19 ± 1	1376 ± 14	468
950W	1065 ± 20	15 ± 4	1272 ± 12	451

Although researchers have studied these heat treatments, limited information that compares homogenization, HIP, solution followed by aging treatments, and their combinations was found.

2.4. Effect of Microstructure on Fatigue

The microstructures produced by AM processes have been studied in the context of fatigue performance. Fatigue strength and other mechanical properties of IN718 components are dependent on the microstructure, the defects present, and the surface roughness. The layer-by-layer approach of AM processes resulted in an increased surface roughness (R_z > 100 μm) which led to premature failure under cyclic loading due to increased stress concentrations [16]. Surface finish improvement methods must be employed to improve fatigue strength to the desired performance level. Internal defects, such as Laves and δ phases, also contribute to reduced fatigue life. In low-cycle fatigue tests, Laves phase functioned as a weakening component, separating from the γ phase, and forming microscopic holes that rupture the material interface [16]. Conversely, δ phase improved resistance to fatigue crack growth along the grain boundary due to the intergranular mode of crack growth [2]. The thermal histories experienced by AM'ed components also leads to residual stresses, which develop due to liquid-state cracking mechanisms. Tensile residual stresses (129 ± 20 MPa) present after the SLM process led to thermal cracking during fabrication, therefore accelerated fatigue crack growth. Addition of post-processing annealing reduced tensile residual stress up to 87% [31]. Fatigue life of as-printed IN718 samples has been shown to be much lower than IN718 subjected to heat treatment, due to the remaining presence of defects and residual stresses. In heat treated SLM IN718 samples (homogenization at 1065ºC for 1 h/air cooling), yield strength and ultimate tensile strength were improved by roughly 84% and 48%, respectively [32]. Introduction of solution treatment (980ºC for 1 h/ air cooling) and dual aging (760ºC, 10 h/furnace cooling at 55ºC/h to 650ºC for 8 h/air cooling) improved fatigue strength by 36.5%. To rid specimen of both undesirable defects/phases and residual stresses, post processing techniques must be implemented.

The control of L-PBF process parameters has been shown to have positive effects on print quality, but optimal parameters have not yet been defined for fatigue performance. Post processing treatments such as homogenization, HIP, and solution and aging have proven to be successful in removing detrimental phases and defects present after the L-PBF process, but few have directly compared the combinations of these treatments with success in improving fatigue life. Because of this, an effort has been made through this research to evaluate L-PBF parameters and the combinations of post processing techniques to find an optimal strategy to improve fatigue performance.

3. EXPERIMENTS

The experiment was performed in two main stages. In the first stage, the samples were fabricated using three different process parameter groupings. Following the printing, samples were grouped again and subject to six different heat treatment strategies (HG, HIP, SA) varying in combination. The second stage consisted of the porosity, hardness, and microstructure of each sample being analyzed. Results were verified in fatigue tests conducted in a parallel study. Figure 3.1 shows the experimental process followed for the above mentioned stages.

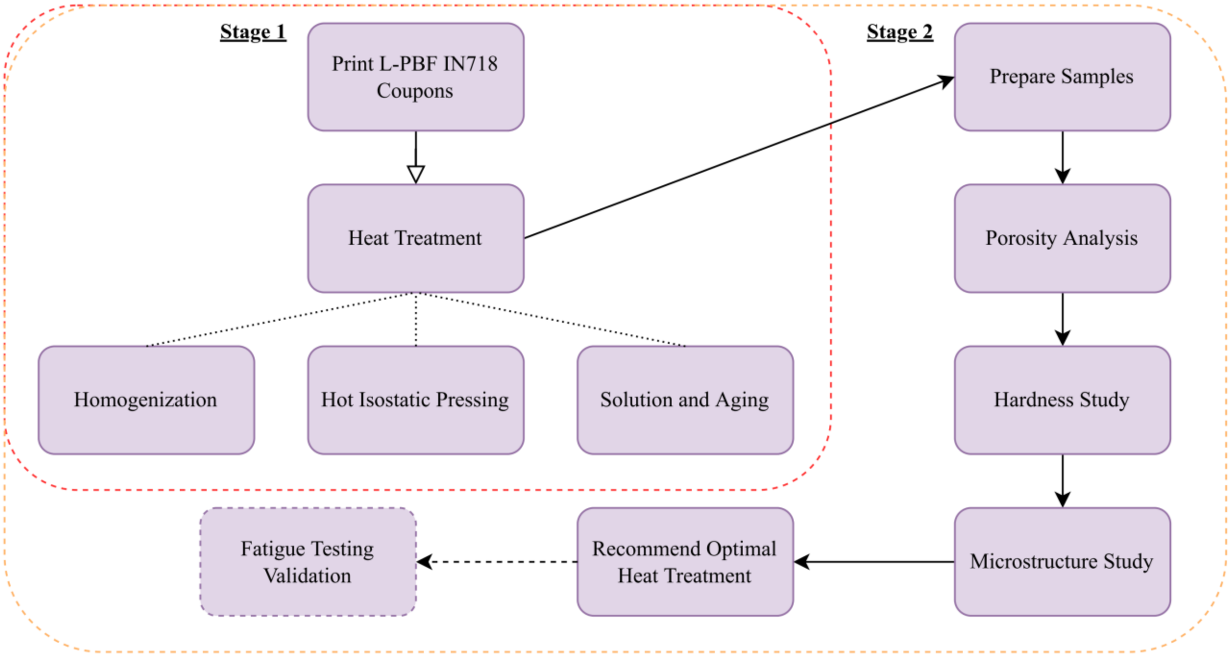

Figure 3.1 Flow diagram of experimental stages

For L-PBF and all post processing, the ranges of parameters were limited based on the constraint given by the industry collaborator KGSBO. The three scanning speeds and their resultant energy densities were chosen based on a range of common values used by the company during normal fabrication of L-PBF components as well as the capabilities of the machine used for sample fabrication. Homogenization, HIP, and solution and aging treatment parameters (such as, all temperatures, timing, types of cooling, etc.) were chosen based on the standard processes used at KGSBO. These restrictions were considered in the development of future work.

3.1. Equipment and Software

The following equipment was used to execute the necessary steps in the experiment:

1. Renishaw AM400 Machine
2. Renishaw AM500Q Machine
3. MTS 100KIP UTM Fatigue System
4. Dremel 4300 Hand Polisher
5. Olympus STM6 Optical Microscope
6. Buehler Handimet Roll Grinder
7. Wilson VH1102 Vickers Hardness Tester
8. Rockwell Hardness Tester
9. Cressington 108 Auto Sputter Coater
10. Vega 3 Tescan Scanning Electron Microscope
11. Oxford Instruments X-Act Energy Dispersive Spectroscopy System

The following software programs were used to aid in necessary data analysis for the experiments:

1. Olympus cellSens
2. Aztec EDS Software
3. ImageJ (Fiji)
4. Microsoft Excel

3.2. Laser Powder Bed Fusion of IN718

Samples were produced by L-PBF using the Renishaw AM400 Machine. Thirty six cylindrical coupons (25 mm x 12.5 mm diameter) and divided into three main groups with respect to the print parameters used during fabrication. Samples were labeled A1-A12, B1-B12, and C1-C12. The A labeled samples were produced with scanning speed of 1500mm/s and energy density 45.5 J/mm^3, B samples were produced with scanning speed 1250mm/s and energy density of 54.5J/mm^3, and C samples were produced with scanning speed 1000mm/s and energy density 68.2J/mm^3. The complete print parameters and their respective labeling are shown in Table 3.1.

Table 3.1 L-PBF print parameters

Label	**A1-A12**	**B1-B12**	**C1-C12**
Laser power (W)	450	450	450
Laser speed (mm/s)	1500	1250	1000
Hatch distance (mm)	0.11	0.11	0.11
Layer thickness (mm)	0.06	0.06	0.06
Energy density per volume (J/mm^3)	45.5	54.5	68.2

For the L-PBF process, a Gas Atomized IN718 powder with average particle size of 50µm was used with the composition listed in Table 3.2.

Table 3.2 Chemical composition (%wt) of IN718 ASM specification [1] and powder used in experiments [33]

Element	ASM Specification	Experiment Powder
Ni	50-55	51.99
Cr	17-21	18.58
Fe	~17	19.73
Nb	4.75-5.5	5.17
Mo	2.8-3.3	3.02
Ti	0.65-1.15	0.99
Al	0.2-0.8	0.49
C	<0.8	0.024
Co	<1.0	0.14
Cu	<0.3	0.12
Si	<0.35	0.073
Mg	<0.35	0.074

3.3. Heat Treatment Strategies

The effects of different heat treatment strategies were to be analyzed along with the effects of the L-PBF print parameters. The experiments utilized homogenization (HG), hot isostatic pressing (HIP), and solution and aging (SA) treatments. The as-printed (AP) samples and the post-processed samples were divided into six sub-groups of different heat treatments: AP, HG, HG+HIP, HG+HIP+SA, HIP, and HIP+SA. The labeling strategy for each combination as well as the treatments included in each combination are listed in Table 3.3.

Table 3.3 Labeling strategy for each heat treatment combination

	Heat Treatment			
Label	**AP**	**HG**	**HIP**	**SA**
ABC 1,2	Yes	x	x	x
ABC 3,4	Yes	Yes	x	x
ABC 5,6	Yes	Yes	Yes	x
ABC 7,8	Yes	Yes	Yes	Yes
ABC 9,10	Yes	x	Yes	x
ABC 11,12	Yes	x	Yes	Yes

3.3.1. Homogenization

Homogenization was analyzed in the experiments as a method to promote the dissolution of Laves phase present after printing. Samples A/B/C 3-8 were subject to the HG treatment with the parameters listed in Table 3.4.

Table 3.4 Homogenization process parameters

Parameter	Value
Temperature [ºC (ºF)]	980
Time (hrs)	1
Cooling Type	Water quenching

3.3.2. Hot Isostatic Pressing

The HIP process was analyzed in the experiments. This method was used to analyze its ability to reduce the porosity present in the printed samples. Samples A/B/C 5-12 were subject to the HIP treatment according to the parameters listed in Table 3.5.

Table 3.5 HIP process parameters

Parameter	Value
Gas	Argon
Temperature [ºC (ºF)]	1163 (2125)
Pressure [MPa (ksi)]	103 (15)
Time (hrs)	4

3.3.3. Solution Aging

Solution and aging treatments were analyzed for their effects on the development of grain boundaries in the printed samples. Samples A/B/C 7,8 and 11,12 were subject to the SA treatment defined in Table 3.6.

Table 3.6 Solution and aging process parameters

	Solution	Aging
Parameter	**Value**	
Temperature [ºC (ºF)]	1066 (1950)	788 (1450)
Time (hrs)	2	7
Cooling Type	Air cooling	Air cooling

3.4. Sample Preparation

The cylindrical coupons were designed to have a conical connection to the L-PBF print plate. This configuration is shown in Figure 3.2.

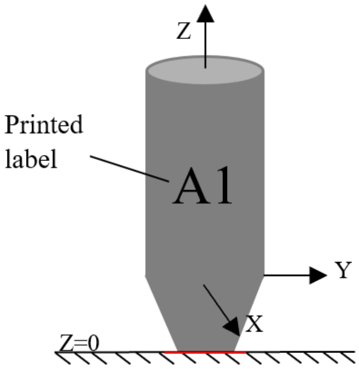

Figure 3.2 Diagram of printed sample

Each sample was sheared off and faced on a lathe at location Z=0 to remove the conical shape connecting the cylinder to the print plate. This process created machine lines on the surface of the part that was to be studied which were to be removed through grinding.

3.4.1. Grinding

A uniform surface free of as-printed/machining lines is necessary to analyze the porosity and hardness of the samples. It is also necessary in preparation for the etching process. A smoother sample surface will also improve the results of observation under an optical microscope. The grinding of the cylindrical coupons was completed by hand on the Buehler Handimet Roll Grinder as shown in Figure 3.3.

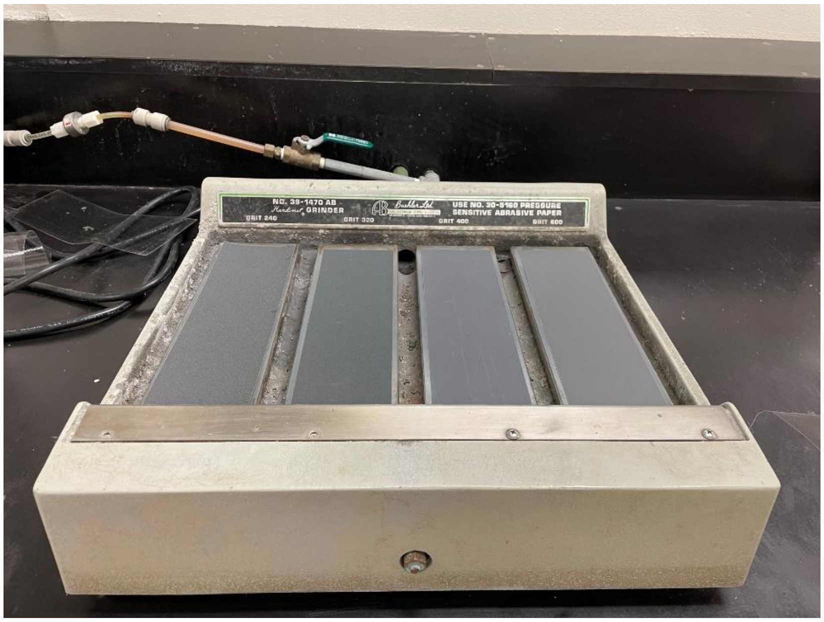

Figure 3.3 Hand grinder with grit paper (from left to right) 240, 320, 400, 600

The hand grinder was connected to a water supply so that each grit paper station was constantly being cleaned. For both the surfaces that were exposed after printing and the surfaces that were faced, grinding operations were performed. A sample was grinded on the 240 grit paper until uniform grind marks were observed on the sample surface. After passing the inspection, the sample was rotated 90 degrees, so that the grind marks obtained from the next grit paper (320 grit) would be perpendicular to the 240 grit marks. This process was repeated for both the 400 and 600 grit papers, inspecting between each step, and rotating by 90 degrees for perpendicular marking. Grinding was deemed complete when only uniform 600 grit paper lines were visible on the surface. Timing for each grit paper varied and was dependent on visual inspection rather than a strict time limit.

3.4.2. Polishing

After grinding was completed, each sample was polished to remove all grinding marks and achieve a smooth, mirror-like surface. Polishing was performed using the Dremel 4300 Hand Polisher. Three types of diamond paste were used for polishing. The polishing equipment is shown in Figure 3.4.

a) **b)**

Figure 3.4 a) Dremel 4300 setup and b) diamond paste for polishing

Samples were polished using the 7/5 micron diamond paste for 60 seconds, or until inspection showed that grind marks were removed, followed by the 1.0 micron and 0.5 micron paste, respectively. To aid the removal of grinding and any smeared polishing lines, small circles were made on the surface when polishing as moving in a straight line will not rid the surface of the streaks. Between each diamond paste step, samples were placed in a small graduated cylinder filled with isopropyl alcohol and cleaned with an ultrasonic cleaner for 120 seconds (setup shown in Figure 3.5).

a) **b)**

Figure 3.5 a) Ultrasonic cleaner and b) setup for cleaning process

After all polishing operations were complete and a mirror-like surface was achieved, the samples were placed in an airtight container to prevent contamination before further experimentation.

3.5. Testing

For the first phase of the experiment, three types of tests were conducted:

1. Microscopy to observe and analyze the present porosities in the surface of the cylindrical coupons.
2. Vickers and Rockwell B hardness tests to compare hardness values between different heat treated samples.
3. Microstructure study on the OM and SEM to analyze the presence of detrimental particles such as Laves phase, δ phase, Nb-rich carbides, and aluminum oxides in the coupons.

3.6. Porosity

Each of the samples were observed under the Olympus STM6 optical microscope (Figure 3.6) for their porosity.

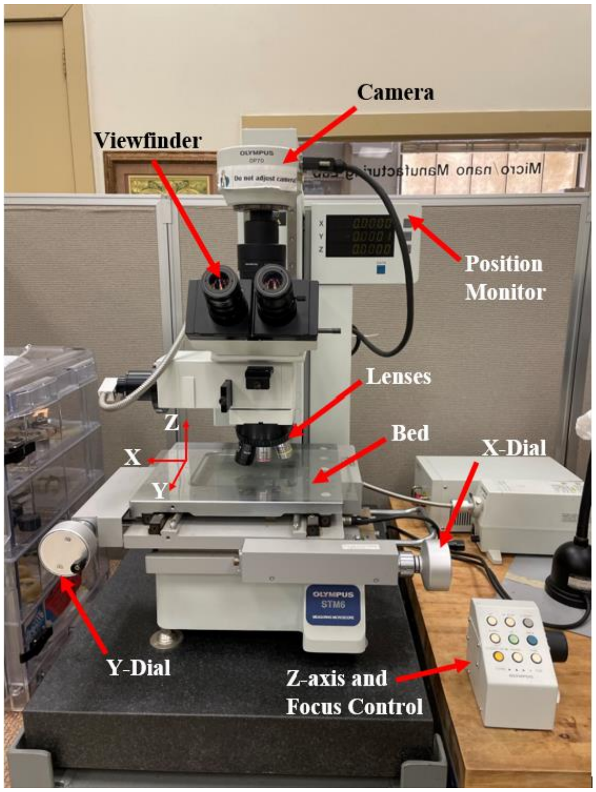

Figure 3.6 Olympus STM6 optical microscope

The microscope was able to focus in four levels of magnification: 5x, 10x, 20x, and 50x. The focus of the lens can be altered by moving the lens along the z-direction. The control panel for the microscope allows for both coarse and fine focusing adjustments. On the microscope bed, there are two handles to allow movement in the x and y directions on the horizontal plane. The monitor readout displays the x, y, and z position of the lens and also allows for the zeroing of any axis value. The surfaces of the coupons were divided into nine sections according to Figure 3.7 and individual pictures were taken using the 5x magnification lens of each section.

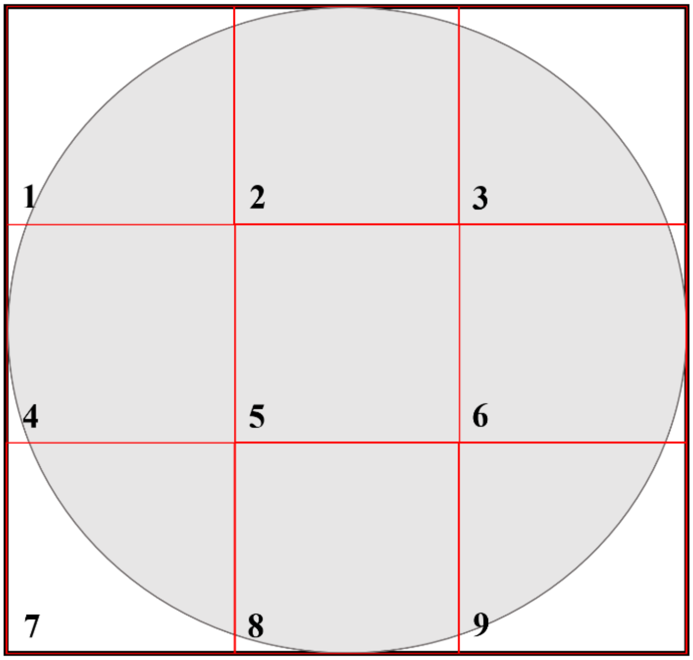

Figure 3.7 Sectioning strategy for porosity imaging on the top surface of samples

The surfaces were sectioned because the lowest magnification did not allow for a complete view of the top surface. The nine sections were grouped and saved following the naming pattern of “PartName_SurfaceSection” (ex. C2_4).

3.6.1. ImageJ Analysis

Following the capture of images on the OM, the nine images for each sample were then fused together using the “Stitching” plugin on ImageJ software. Once the fused images were created, the following step-by-step process was followed to obtain quantitative porosity data through ImageJ:

1. Start ImageJ and open the fused image file of interest (File > Open). Before analysis, the scale must be set for conversion from pixels to desired units.

2. With the image file open, use the “Draw Line” tool across the scale bar on the image and make sure the angle of the line is 0º for an accurate measurement. Take note of the length measurement of the line, the measurement is in pixels (Figure 3.8a and Figure 3.8b).
3. Select Analyze > Set Scale and enter the recorded value for the number of pixels, the known value of the scale bar, and the units listed in the scale bar and click OK (Figure 3.8c).

With the scale conversion set inside the software, proceed with the following steps to perform porosity analysis. If scale was previously set, skip steps 2 and 3.

4. Go to Image > Color > Split Channels, select three channels will open. Close out of the two channels that do not provide desired contrast.
5. On the now greyscale image, select the area of interest with the “Rectangle” or “Circle” tool and crop (Shift+Ctrl+x) (Figure 3.9a and Figure 3.9b).

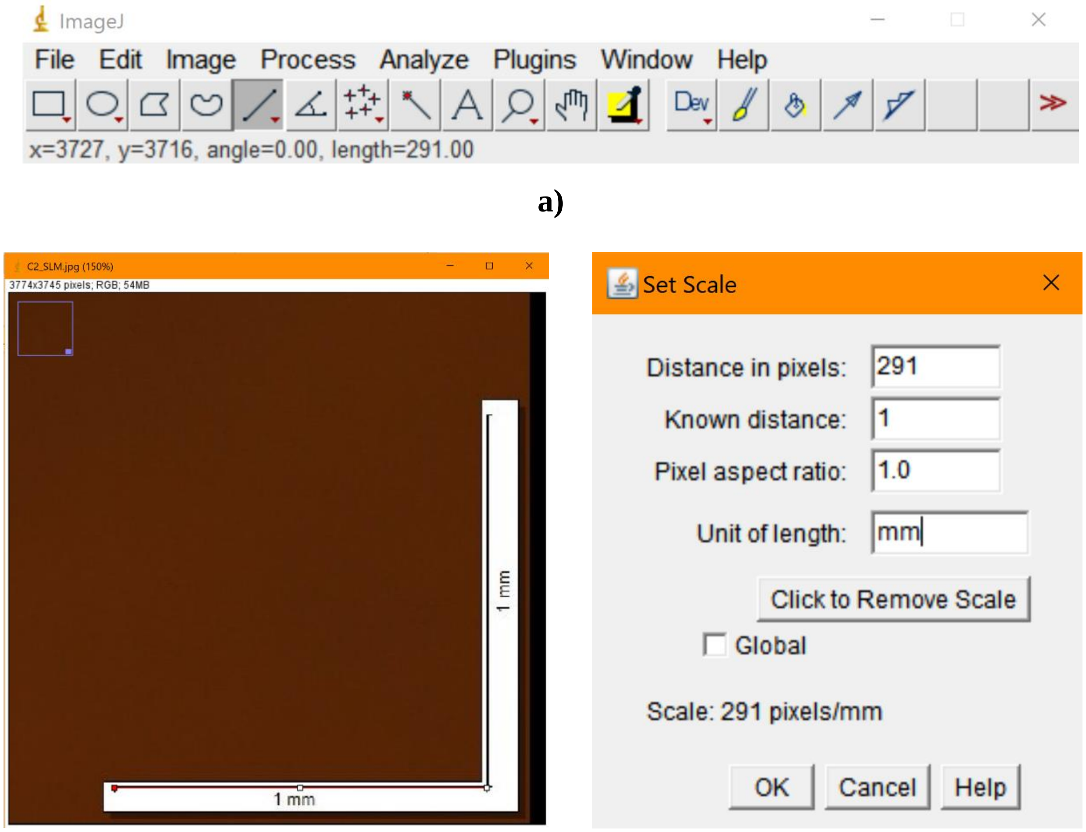

```
x=3727, y=3716, angle=0.00, length=291.00
```

Distance in pixels: 291
Known distance: 1
Pixel aspect ratio: 1.0
Unit of length: mm
☐ Global
Scale: 291 pixels/mm

a)

b)

c)

Figure 3.8 a) "Draw Line" tool selected and angle = 0, b) horizontal line drawn along OM image scale bar, and c) Set Scale window

6. Select Image > Adjust > Threshold and adjust the bar until only the porosities or areas of interest are red (Figure 3.9c and Figure 3.9d). Do not hit apply and leave the Threshold window open.
7. Now select Analyze > Analyze Particles. Set size limits and circularity limits if necessary and in the pull-down menu, choose “Outlines”. Select boxes for “Summarize”, “Include holes”, “Exclude on edges”, “display results”, and hit OK (Figure 3.9e).

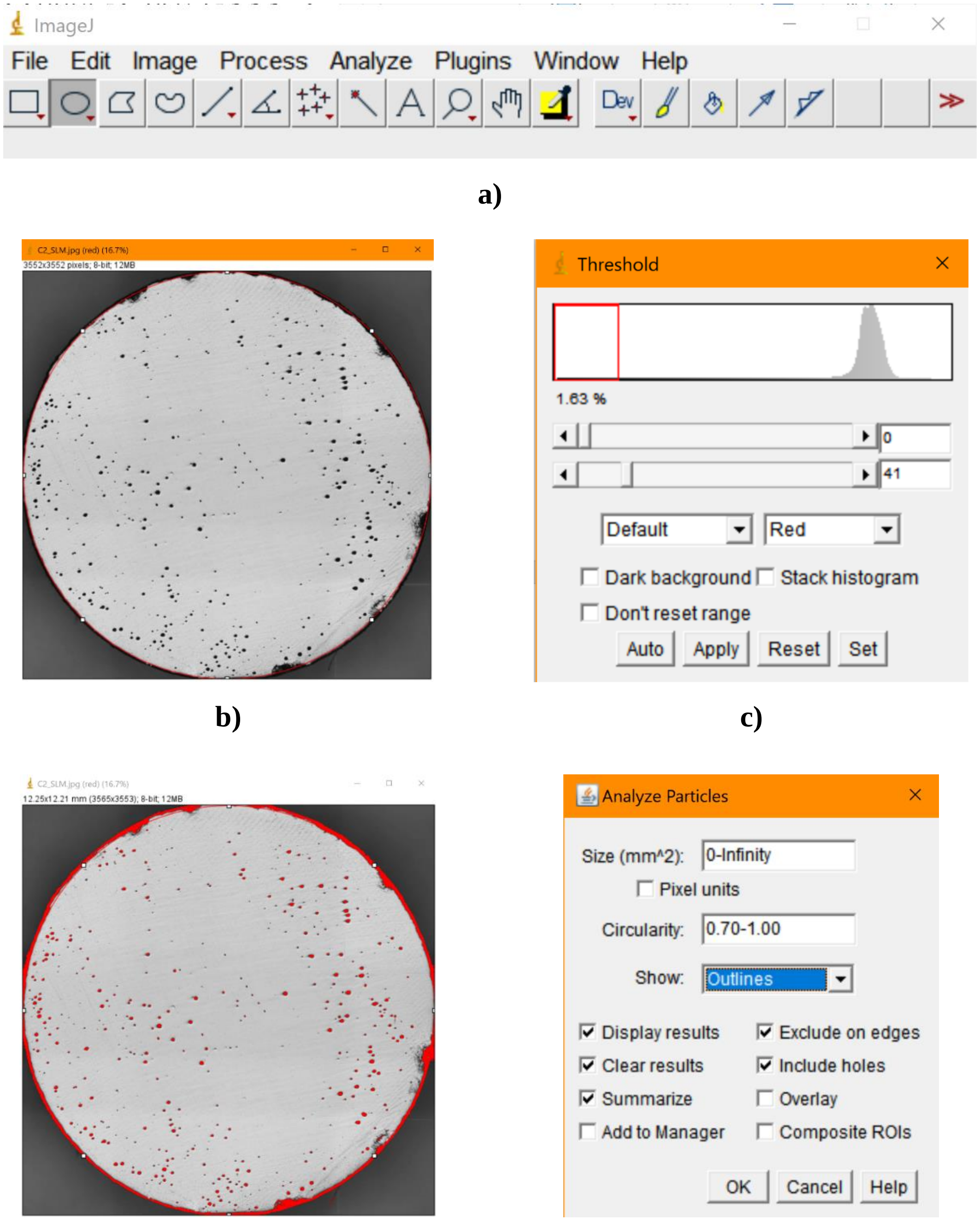

ImageJ

a)

C2_SLM.jpg (red) (16.7%)

3552x3552 pixels; 8-bit; 12MB

b)

Threshold

1.63 %

0

41

Default

Red

☐ Dark background ☐ Stack histogram

☐ Don't reset range

c)

C2_SLM.jpg (red) (16.7%)

12.25x12.21 mm (3565x3553); 8-bit; 12MB

e)

Analyze Particles

Size (mm^2): 0-Infinity

☐ Pixel units

Circularity: 0.70-1.00

Show: Outlines

☑ Display results ☑ Exclude on edges

☑ Clear results ☑ Include holes

☑ Summarize ☐ Overlay

☐ Add to Manager ☐ Composite ROIs

f)

Figure 3.9 a) "Draw Circle" tool selected, b) cropped area of interest for porosity analysis, c) Adjust Threshold window, d) application of red color to all porosities, red on the edge of part excluded, and e) Analyze Particle window to produce data results

Output will provide values for the total pore area, % porosity, and the diameter values for each pore. Save the summary and in-depth results file to process further in Excel.

3.7. Hardness Testing

To avoid the inclusion of hardness indentions in the porosity analysis, hardness tests were performed following the porosity study. Two hardness measurements were achieved for each of the samples: Vickers hardness (VH) and Rockwell B (RB). VH obtained microhardness data while RB obtained a much more representative hardness value for the coupons.

3.7.1. Vickers Microhardness

Microhardness measurements were taken at three random locations across the top surface of the samples. Measurement locations remained close to the center of the part to avoid variance when approaching the edge of the part. Measurements were also spaced so that work-hardening effects of previous measurements would not affect subsequent measurements. The microhardness tests were performed using the Wilson VH1202 Vickers hardness tester (Figure 3.10) with manual controls and three magnification lenses: 5x, 10x, and 50x.

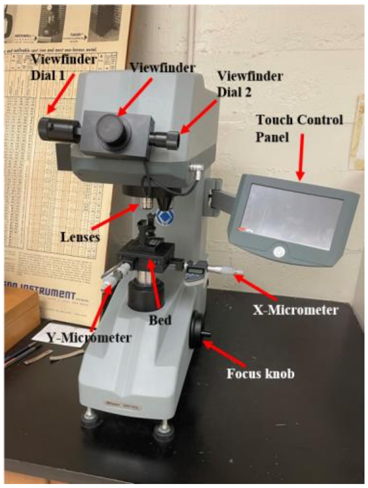

Figure 3.10 Wilson VH1202 Vickers hardness tester

The Vickers machine did not have a fixture that could accommodate the cylindrical coupons, so the fixture shown in Figure 3.11 was fabricated to secure the samples during testing. The fixture was machined so that the surface would be level and the screw on the side of the fixture allowed for each sample to be secured so that it would not move during indentation.

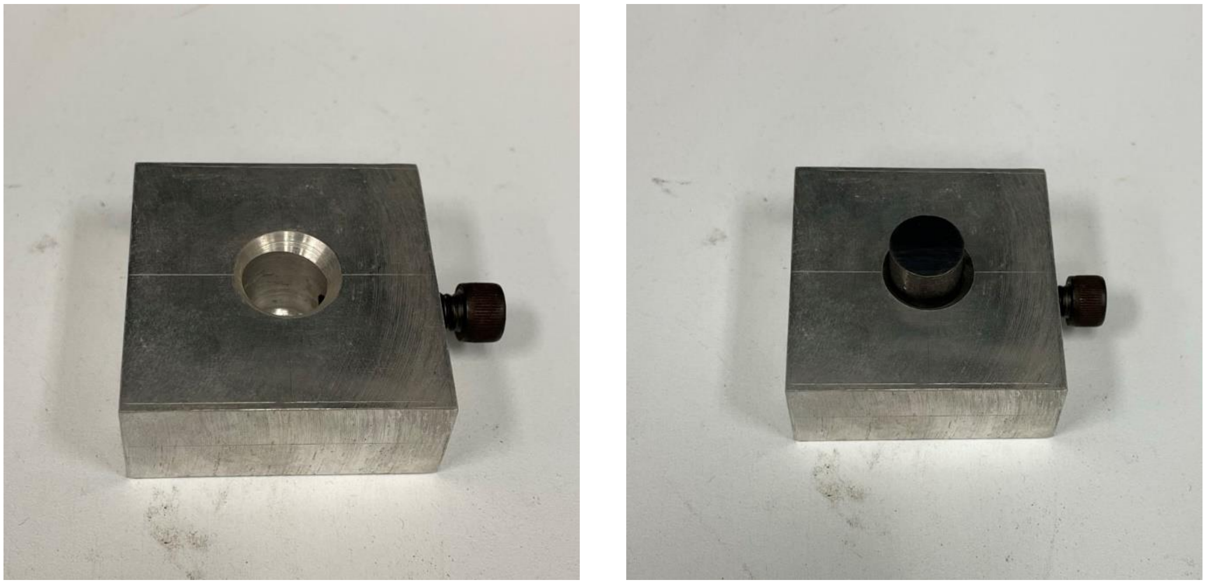

a) **b)**

Figure 3.11 Fabricated aluminum fixture for microhardness testing a) without sample and b) with sample

The two micrometers on the tester bed control movements along the x-axis and y-axis. The z-axis/focus can be controlled using a knob on the side of the machine. The viewfinder can be used to observe the surface of the sample and take measurements for the hardness indention. The digital display allowed for control over the process parameters for the testing. The parameters listed in Table 3.7 were used for Vickers testing.

Table 3.7 Vickers microhardness test parameters

Parameter	Value
Applied Load (gf)	300
Dwell Time (sec)	15

The following procedure was conducted for the microhardness testing:

1. The sample was secured in the custom fabricated fixture, placed under the lens, and the machine was turned on. The parameters were then set according to Table 3.7.
2. By looking into the viewfinder and using the micrometers to translate on the part surface, a new testing position was found using the 10x magnification lens.
3. The indenter is activated on the digital display and the measurement is taken.
4. After indenting, the indentation was observed in the viewfinder.
5. One crosshair is aligned with one of the four corners on the indentation using the viewfinder dial. When positioned, the other dial was used to position the second line on the opposing corner of the indentation. The measurement between the two lines on the opposing corners was recorded using the digital display.
6. Step 5 was repeated for the other two corners and a microhardness value was recorded.

3.7.2. Rockwell Hardness

Rockwell testing was performed on the Rockwell Hardness Tester (Figure 3.12) to function as support of the microhardness data and a more representative value for the material properties.

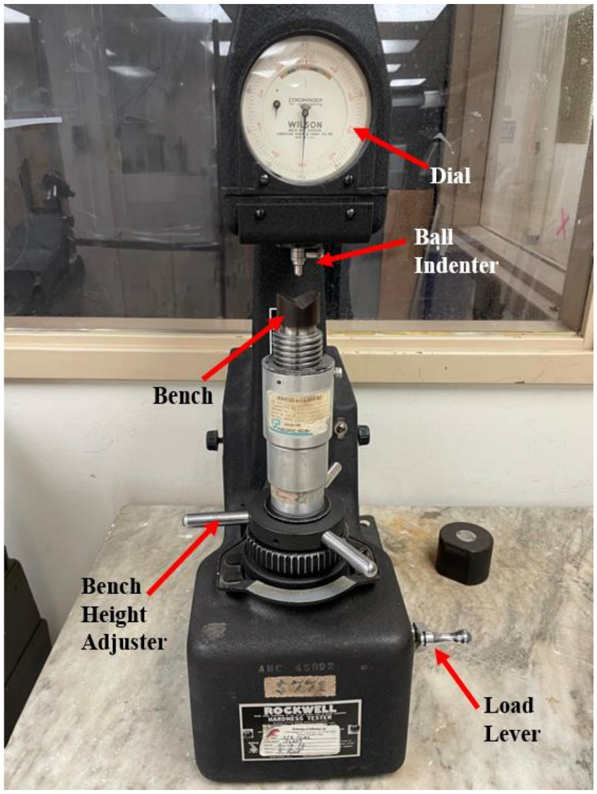

Figure 3.12 Rockwell Hardness Tester

Measurements for RB were taken around the outer sides of the samples in three random locations. After each measurement, the samples were simply rotated by hand to find a new location. No custom fixture was necessary. The parameters listed in Table 3.8 were used for Rockwell testing.

Table 3.8 Rockwell B test parameters

Parameter	Value
Applied Load (g)	100
Ball size (inch)	1/16

The following procedure was followed for Rockwell testing:

1. Insert 1/16” ball indenter into the chuck holder and tighten. Then place the bench that is needed for the specific type of specimen into the machine. For this experiment, a V-shaped bench was used to support the cylindrical geometry.
2. Place specimen on the bench and use feed handle to raise the bench up to the indenter. Make light contact with the sample and continue to slowly raise until the minor load is applied. This load is applied when the small needle on the dial indicator is aimed at the red dot.
3. For B scale measurements, position the dial face so that the needle is aimed at the zero for the inside (red) measurement readings.
4. Apply the major load by pressing the handle down on the side of the machine. Wait for the needle on the dial to settle and release the load. Record RB value from the dial.
5. Repeat in two other random locations around the outer surface of the specimen.

3.8. Microstructure Study

Odd numbered samples chosen for microstructure studies to preserve half of the samples for future porosity studies, if necessary.

3.8.1. Molding

Samples printed with the print parameter that was determined to provide minimal porosity were paired and placed in epoxy molds for ease of analysis. Samples were paired as follows: B1 and B3, B5 and B7, B9 and B11. Each pair was placed in a silicone mold cup to establish position, and an aluminum identification marker was placed above the lower numbered sample (Figure 3.13).

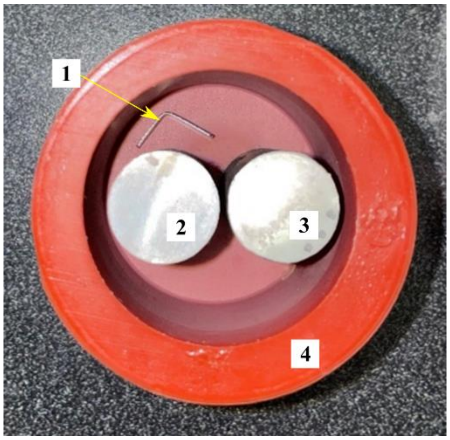

Figure 3.13 Typical mold setup with (1) aluminum marker, (2) B1 sample, (3) B3 sample, and (4) silicone mold

The following procedure was followed to create the epoxy molds for the paired samples:

1. Gather samples, silicone cup, PELCO epoxy resin and hardener, and aluminum markers.
2. Measure the dimensions of the silicone cup and each sample. In order to know the volume of the cup that needs to be filled, subtract the sample volume from the calculated cup volume.
3. From the total volume to be filled with epoxy, ¾ of that volume will consist of resin and the remaining ¼ will consist of hardener (3 parts resin, 1 part hardener).
4. Multiply the epoxy volume by the number of molded pairs needed (in this case, three) and measure out the resin in a graduated cylinder in mL. Measure hardener amount with a pipette and combine with the resin.
5. Mix resin and hardener for 2-3 minutes, or until uniform in color. Do not mix vigorously to avoid formation of air bubbles in mixture.
6. Once completely mixed, distribute the mixture equally among the silicone cups with samples and markers placed in their positions.

7. Leave samples in an airtight container overnight to allow them to dry and harden completely. When hardened, the silicone cup can be peeled off and the molded pairs will be ready.

3.8.2. Etching

Grinded and polished surfaces were etched to enhance microstructural features and defects. All etching work was performed within a fume hood to allow for proper air flow of harsh chemicals. Etching was performed using Kallings etchant (5g CuCl + 100ml HCl + 100 mL H_2C_5OH) and cotton swabs for application over varying time steps, depending on the applied heat treatment. Kallings values were reduced by a factor of 10 to compensate for the smaller volume of samples. Surfaces were etched with a gradient where the lowest section of the surface received the largest etching time, resulting in an over-etched region where defects were more visible, a middle region where the material was etched properly for visible grain boundaries, and the final regions of light to no etching in the upper surface region (Figure 3.14).

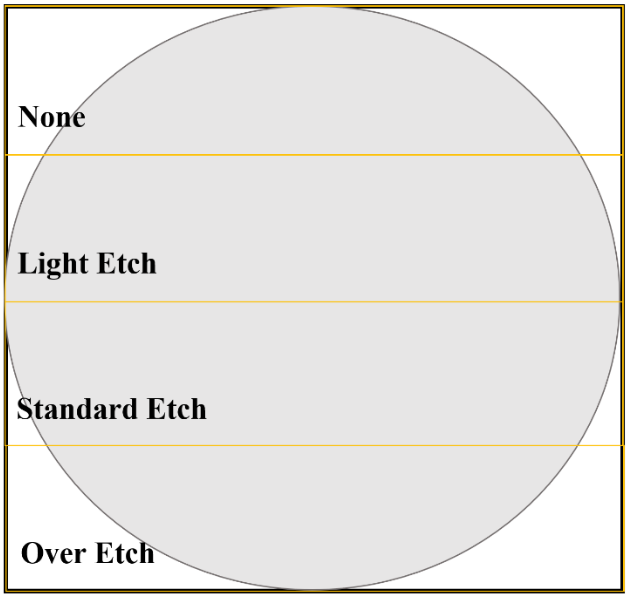

Figure 3.14 Etching gradient applied to samples

The following procedure was followed for etching of the samples:

1. Open AWS LB-1000 digital scale and turn it on. Place a small glass petri dish on scale and press ZERO.
2. Scoop out CuCl from container with plastic spoon (avoid reaction with metal scoop) and dispense on to the dish until a weight of 0.5g is achieved. Return any excess into the container.
3. Transfer CuCl to 100mL graduated cylinder. With pipette, transfer 10mL of H_2C_5OH into the glass cylinder with the CuCl.
4. Using a different pipette, add 10mL of HCl to the mixture. Stir etchant with a third, separate, pipette to avoid contamination. One pipette is dedicated to alcohol, one to acid, and one to stirring.
5. Pour mixture into new petri dish until the bottom surface is covered. etchant is dispensed as needed in the dish to avoid waste. Cover the 100mL cylinder that contains the rest of the etchant and set to the side.
6. Start timer and pick up sample to be etched. With a cotton swab, repeatedly dab into the etchant and immediately apply to the bottom half of the specimen's top surface while it is held at a slight angle. This will force etchant to fall to the lower region of the surface to create the over-etched region, also leaving the upper surface untouched and the middle surface etched adequately.
7. Rotate the swab between applications to allow for fresh etchant to be applied to the swab.
8. Continue applying etchant for 3-4 minutes. When the desired time is reached, stop the timer, and immediately apply water to the specimen surface to halt the etching.

9. Inspect surface on optical microscope to check status of etching. Different heat treatment strategies will result in different resistance to the etchant.
10. If necessary, repeat Steps 6-9 in cycles of 3-4 minutes until the desired surface properties are visible under OM inspection for all specimens. Table 3.9 Cumulative etching time for different heat treated samples shows the total etching times used for the samples.
11. After etching, clean all samples with isopropyl alcohol and dry with compressed air.

Table 3.9 Cumulative etching time for different heat treated samples

Sample	Cumulative Etching Time (min)
AP	8
HG	10
HG+HIP	15
HG+HIP+SA	15
HIP	17
HIP+SA	17

3.8.3. Optical Microscopy

The microstructures of the samples were studied under the Olympus STM6 optical microscope (Figure 3.6).

The following procedure was followed for OM microstructure analysis:

1. Turn on the microscope and microscope light and start the computer program. Place sample under the lens.
2. With the lowest magnification (5x), the computer is set on live mode to view a real-time image of the sample surface.

3. Use the black knob wheel on the control panel to focus the lens image with coarse or fine adjustments.
4. Specimen surface is observed in 5x until a defect is identified. To further inspect the defect, magnification is changed to 10x, 20x, and/or 50x. Adjust the scale as needed, it will not update automatically when switching between lenses.
5. For inspection of void and porous defects, the z-axis on the monitor was set to zero and the focus was adjusted so that the center of the identified defect was clear. If the resulting z-axis location is negative, the defect was properly identified as a void/pore. If the value is positive, the defect was falsely identified and is just surface contamination or an external burr. Surface should be recleaned if contamination is identified.
6. Once a defect is identified, images are captured on the computer software for further analysis.
7. Steps are repeated as needed to capture images of grain boundaries in samples.

3.8.4. Gold Coating

After molding samples in epoxy, the material is no longer conductive. To analyze under the SEM, the material must be conductive, so each molded pair was coated with a thin layer of gold. The Cressington 108 Auto Sputter Coater was used for gold coating operations (Figure 3.15a).

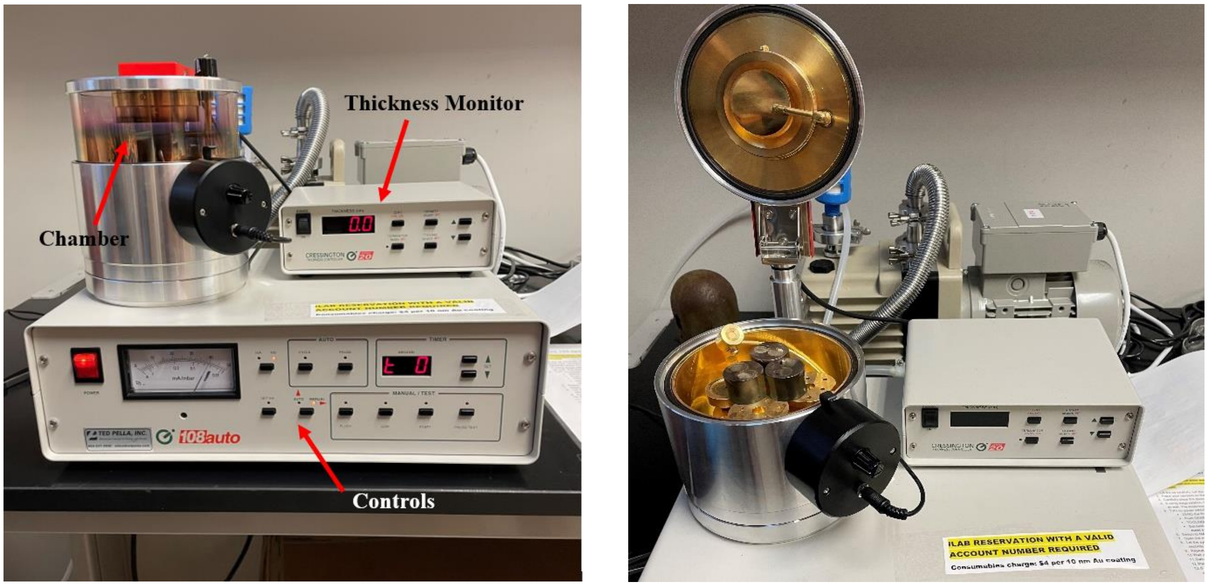

a) b)

Figure 3.15 a) Cressington 108 Auto Sputter Coater used for gold coating in experiment and b) sample placement in coater chamber

The following procedure was followed for gold coating:

1. Lift the lid and glass of the coater chamber and place molded samples on the clean stage (Figure 3.15b). Place glass back on the coater and gently close the lid.
2. If stage rotation is to be used, tilt the stage 30º to achieve coating on the sides of the specimen. The thickness monitor should point up to the center of the samples.
3. Turn on the power for main unit and thickness monitor. On the thickness monitor, first ZERO the monitor, then select DENSITY and set to 19.3 for gold. TOOLING should be set to 1.
4. Desired thickness can be set by holding TERMINATOR and setting a value between 5 and 20 nm. 10 nm was used for this experiment.

5. Switch mode to MANUAL and open the valve for the Argon gas cylinder. When the system pumps down to 0.1 mbar, push the FLUSH button, and wait 30 seconds. Turn off FLUSH and repeat once.
6. Wait until the vacuum reaches 0.02 mbar and switch mode to AUTO. Make sure the paddle shutter in the chamber lid is open and check that the samples are not tall enough to crash into the thickness monitor during rotation.
7. Turn on TERMINATOR and push Auto-Cycle. Two auto flush cycles will be performed by the machine automatically and will begin sputter coating process.
8. Once complete, turn OFF both of the power switches, stop the stage rotation, and set the tilt back to 0º if adjusted for coating. Close the paddle shutter.
9. When the chamber is vented, remove the glass covering and lift the lid. Remove samples and replace the glass and lid.

3.8.5. SEM and EDS Microstructure Analysis

Vega 3 Tescan microscope was used for SEM analysis while Oxford Instruments x-act was used for EDS as shown in Figure 3.16a and Figure 3.16d, respectively. The following procedure was followed for microstructural analysis:

1. Gas cylinders were turned on to provide the SEM machine with pressurized gas necessary for maintaining a vacuum inside the measuring chamber.
2. On the computer screen, the VegaTC software (Figure 3.17a) was used to control the SEM. The vent button was pressed on the screen to vent the vacuum from the chamber (Figure 3.17b).

3. The chamber door was opened, and the sample is fixed appropriately on the bed using a conducting tape as shown in Figure 3.16b. Care shall be taken that no non-conducting substance is in contact with the sample to avoid interference in the SEM recordings.

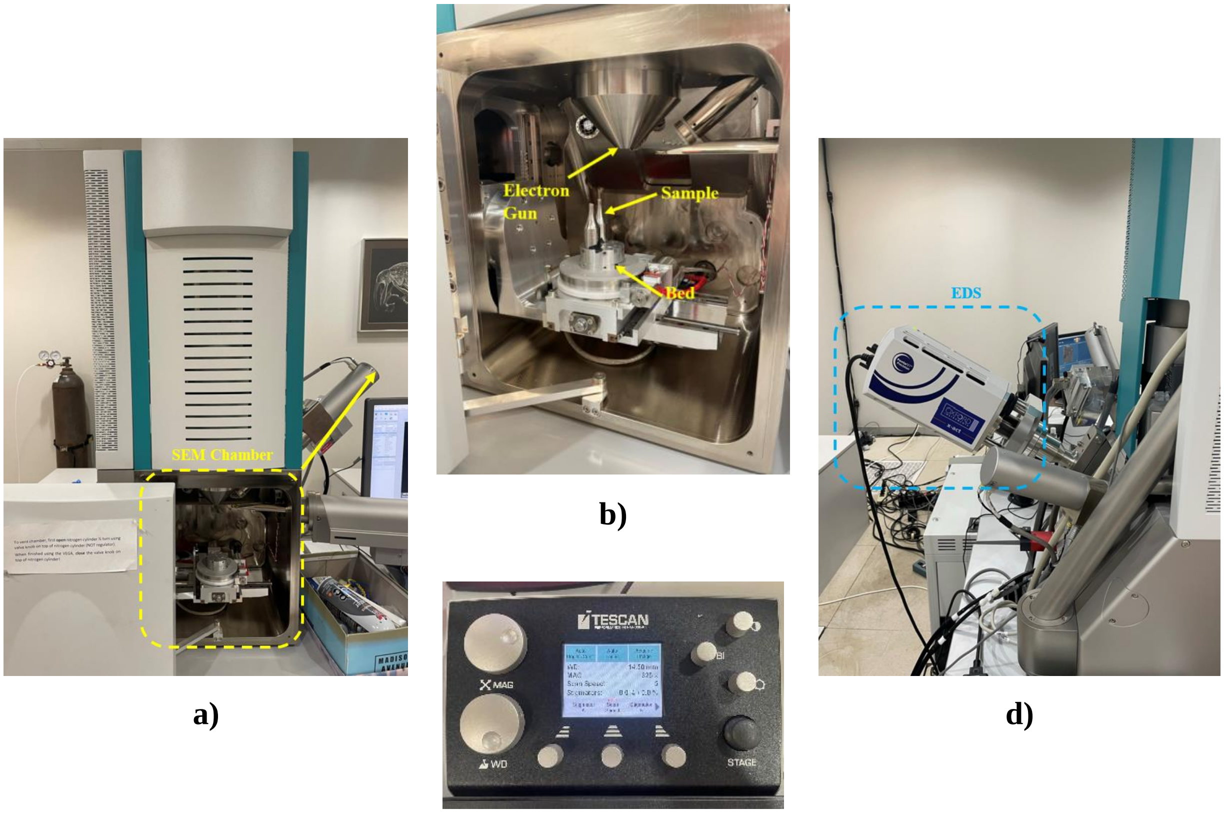

a)

b)

c)

d)

Figure 3.16 a) Vega 3 Tescan SEM, b) sample placed inside SEM chamber, c) SEM controller, and d) Oxford Instruments X-Act EDS System

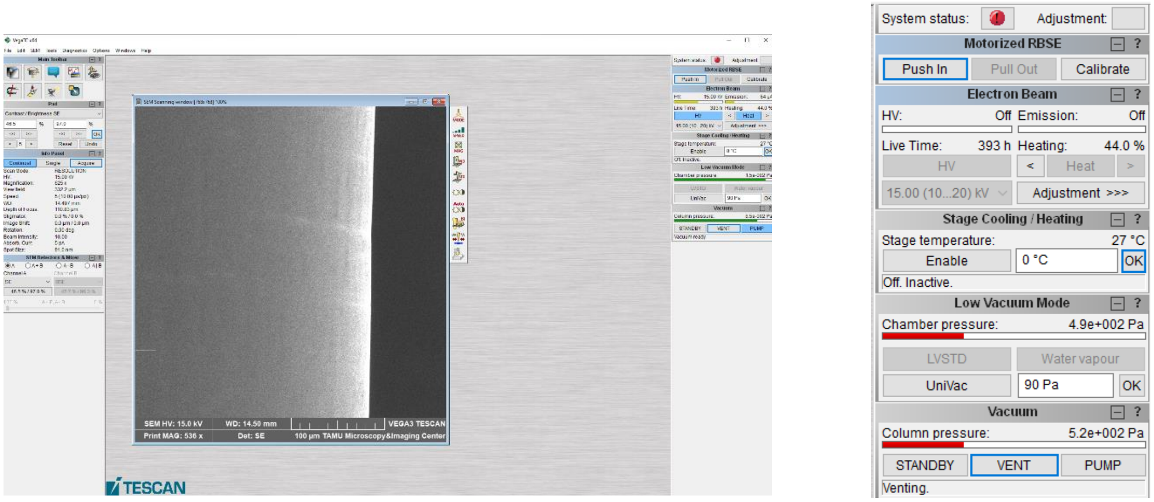

HV: Off
Emission: Off
Live Time: 393 h
Heating: 44.0 %
15.00 (10...20) kV
Stage temperature: 27 °C
0 °C
Off. Inactive.
Chamber pressure: 4.9e+002 Pa
90 Pa
Column pressure: 5.2e+002 Pa
Venting.

a)

b)

Figure 3.17 a) VegaTC software screen and b) chamber controls

4. Chamber is closed and the vacuum is pumped in the chamber using the pump on the computer screen. SEM is ready for operation once the chamber pressure reaches 10^{-2} Pa.
5. The electron gun is turned on to initiate scanning by pressing the HV button and setting the initial voltage at 15kV. If the image is unclear, the voltage can be further increased as per requirement.
6. Using the carousel on the screen and the controller (Figure 3.16c), surface of interest is brought under the electron beam path.
7. MAG and WD scrolls on the controller are used to adjust the vertical distance of the sample surface from the electron beam gun until the image is clear and in focus. WD is recommended to be set at 9mm for the best results. The brightness and contrast of the SEM image can be adjusted using three buttons on the top right of the controller.

8. Once the required surface is identified, the Acquire button can be pressed to capture the image of the surface microstructure.
9. To identify the chemical composition of a site on the sample surface, the SEM is adjusted over the required site. EDS software AZtec (Figure 3.18) is used to control the EDS detector. The data acquisition settings were set as 10keV energy range, 1024 channel resolution, 4 min process time, and 50 sec live acquisition time (Figure 3.19).

Figure 3.18 AZtec EDS Software Screen

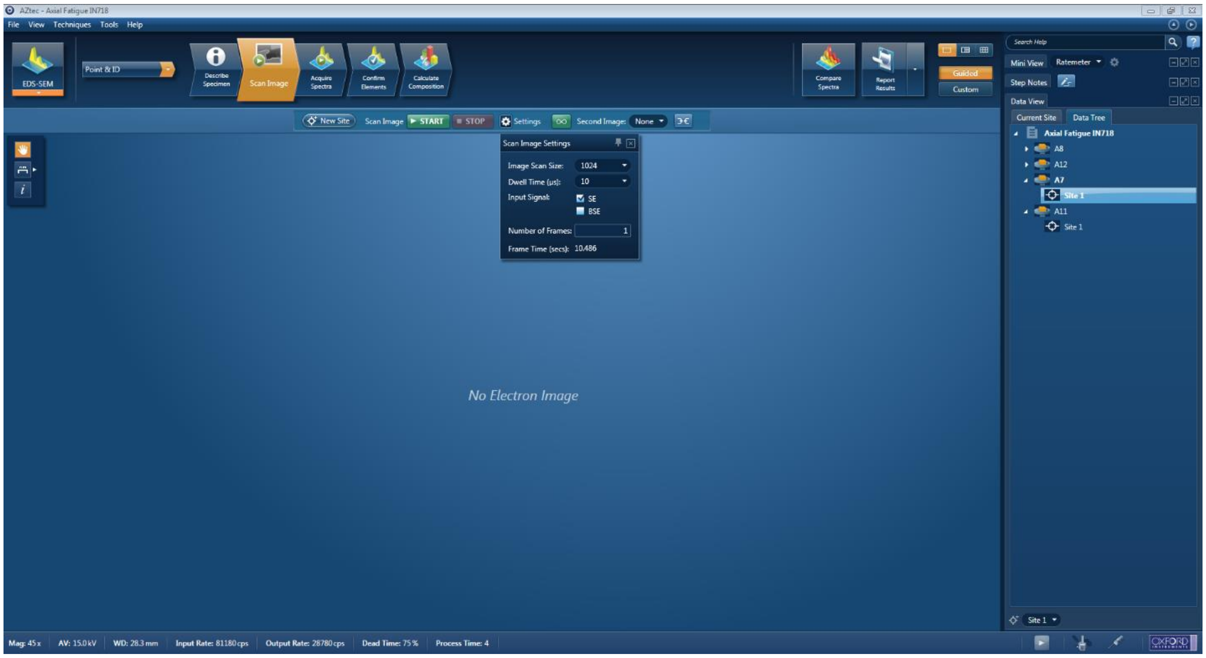

Scan Image Settings
Image Scan Size: 1024
Dwell Time (µs): 10
Input Signal: ☑ SE ☐ BSE
Number of Frames: 1
Frame Time (secs): 10.486

Mag: 45 x | AV: 15.0 kV | WD: 28.3 mm | Input Rate: 81180 cps | Output Rate: 28780 cps | Dead Time: 75 % | Process Time: 4

Figure 3.19 Proper EDS System Settings

10. Before beginning analysis, enter in specimen coating information on the "Describe Specimen" tab to filter out the coating material from composition plots (Figure 3.20).

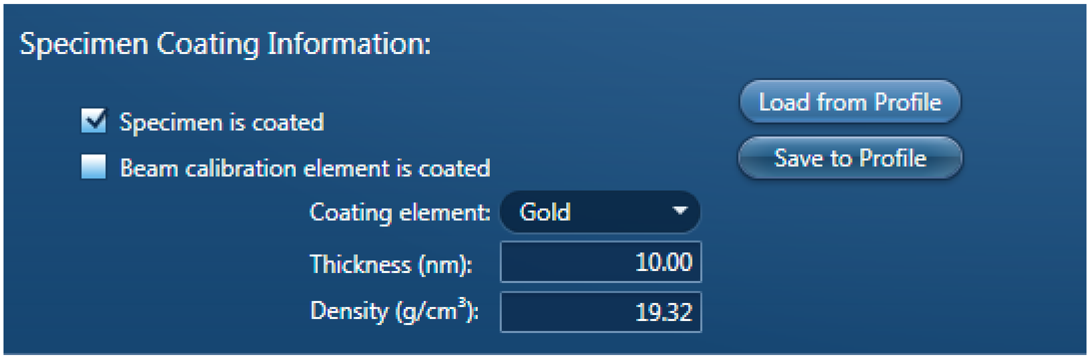

Specimen Coating Information:

☑ Specimen is coated
☐ Beam calibration element is coated
Coating element: Gold
Thickness (nm): 10.00
Density (g/cm^3): 19.32

Figure 3.20 EDS specimen coating information input

11. The detector was turned on using the bottom right corner button on the software screen (Figure 3.18). EDS has two main modes (Figure 3.21): Analyzer mode – to identify the

general composition of a site and Point&ID mode – to identify chemical composition at a specific point in a site.

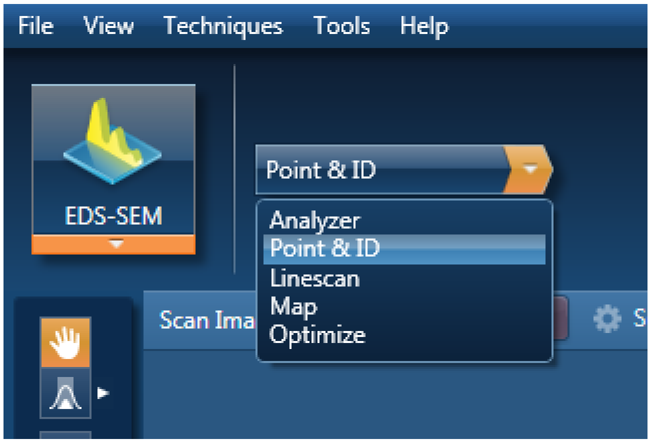

Figure 3.21 Available EDS data modes

12. In Analyzer mode, spectrum is directly acquired using Start Button on the software screen (Figure 3.22) for the site set on the SEM screen. In Point&ID mode, the image of the site is first captured using the scan image window and then selecting the start button. Then mouse cursor can be moved over the scanned image after selecting the ‘Acquire Spectra’ window at the top of the screen and placed at a point where the spectrum is to be acquired.

Figure 3.22 EDS screen in Analyzer mode

13. In the Data Tree on the right side of the screen, the spectrum will fill with a green bar when scanning to show progress (Figure 3.23). It will return to a normal color when complete.

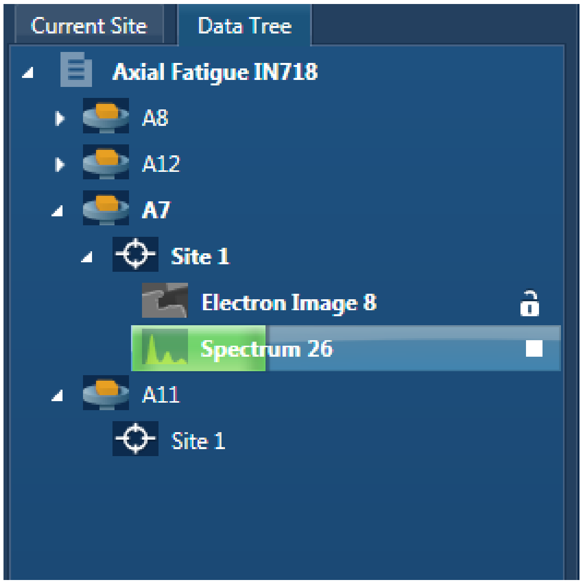

Figure 3.23 Point&ID data collection in progress

14. Detected elements can be confirmed in the ‘Confirm Elements’ window. Spectral data and the scanned images can be saved for further analysis by selecting ‘Save Results/Report Results’ in the top right of the screen (Figure 3.24).

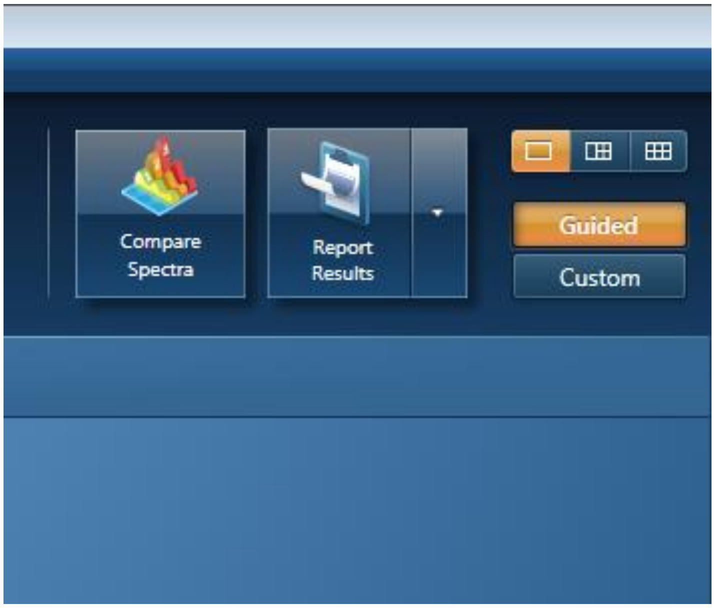

Figure 3.24 EDS Report Results Button

15. If continuing to collect data for the same specimen, keep the result report file open on the computer and select to “Append Results” to add additional data to the report (Figure 3.25).

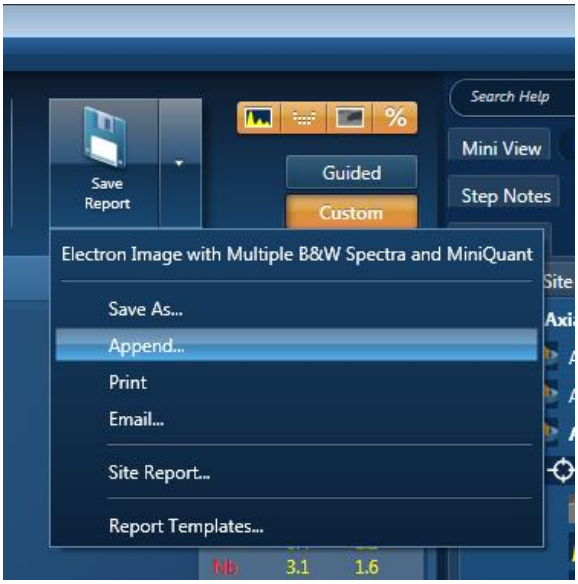

Figure 3.25 EDS append results

16. For formatting the spectral plots, right-click in the plot area and select ‘Noise Peak’ and then ‘Hide’ to correct the scaling on the plot. This hides the initial noise peak and allows for better analysis of the data points (Figure 3.26).
17. Spectra plot data can be exported as EMSA data which will save the results as a .txt file that can be opened and analyzed further in Excel for replotting (Figure 3.27).

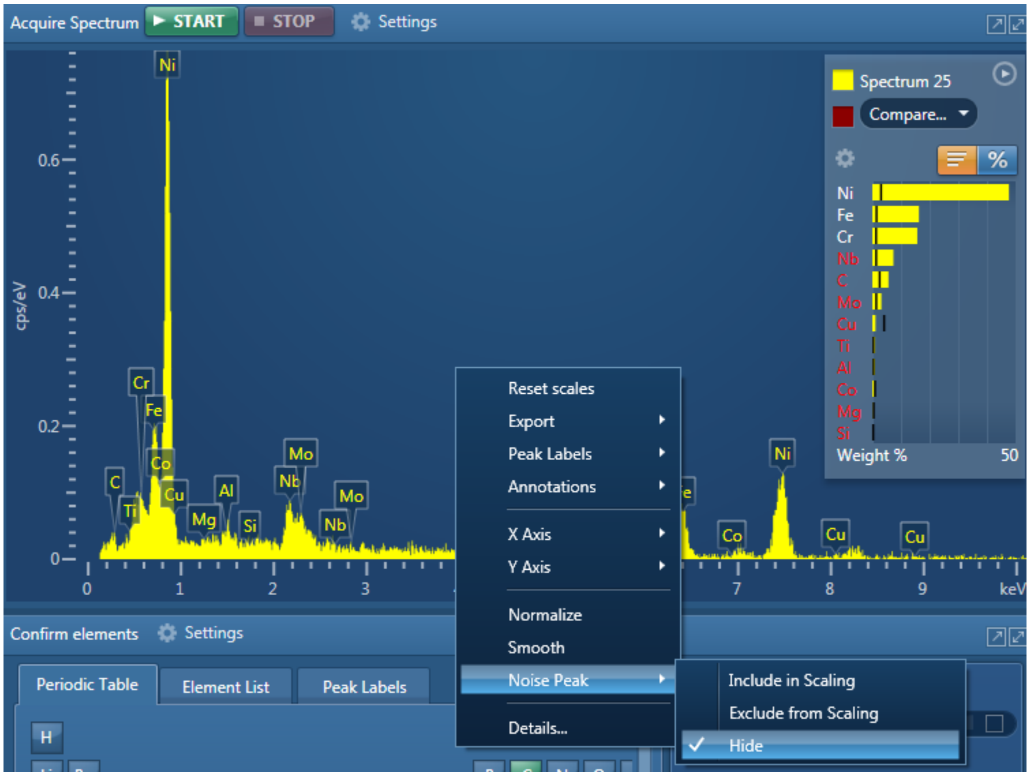

Figure 3.26 Hide Noise Peak in EDS for Plot Scaling

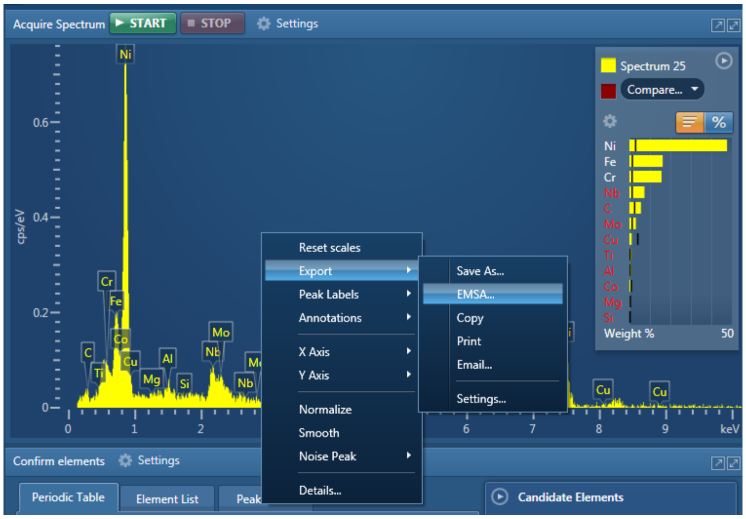

Figure 3.27 Export spectra plot data

18. Once the desired spectra data is acquired for the first site, multiple sites can be taken as data points for each specimen. Return to the ‘Scan Image’ window and select ‘New Site’ in Point&ID mode. This will allow for a rescan of a different site selected on the SEM screen.
19. To report data for a new specimen, save all previous data in a report and select ‘File’ at the top left of the screen and then select ‘Add’. This will provide multiple options, but ‘New Specimen’ should be selected. This will allow for the data to be saved under a new specimen for organizational purposes.
20. If at any point during the spectral analysis a chemical component appears that is determined to be a misidentification, that element can be excluded from the spectra in the “Confirm Elements” window (Figure 3.28).

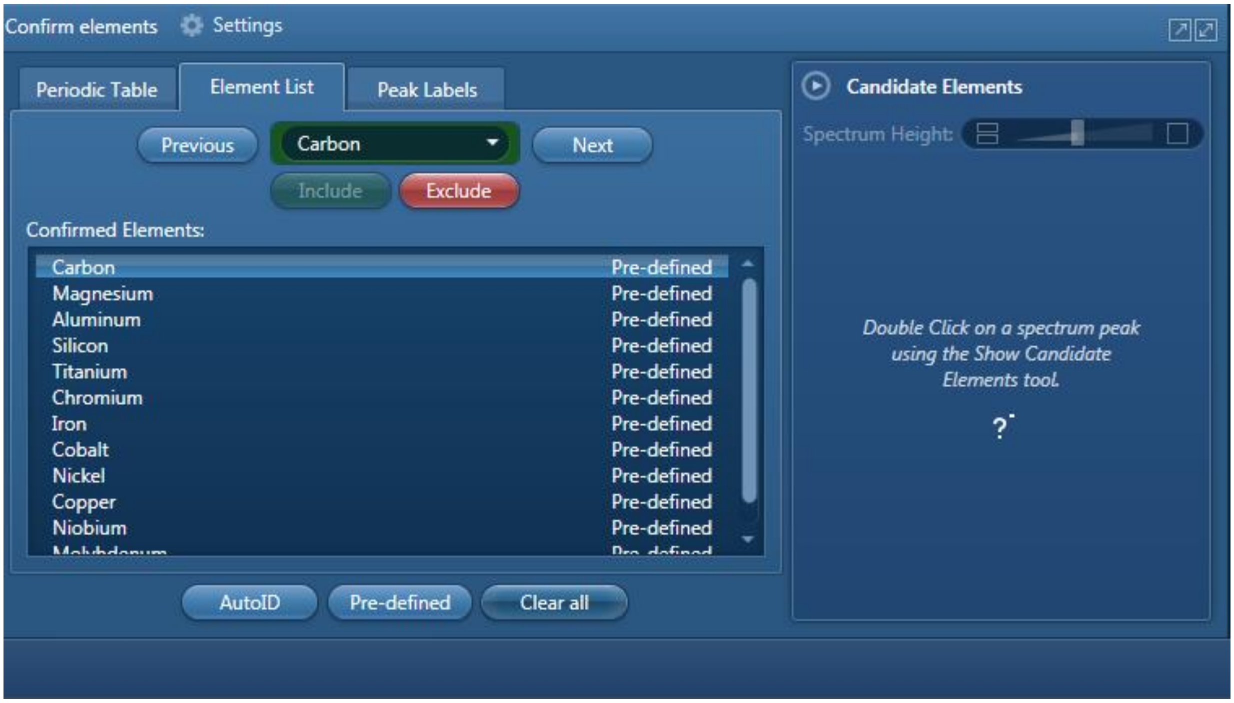

Confirmed Elements:

Carbon	Pre-defined
Magnesium	Pre-defined
Aluminum	Pre-defined
Silicon	Pre-defined
Titanium	Pre-defined
Chromium	Pre-defined
Iron	Pre-defined
Cobalt	Pre-defined
Nickel	Pre-defined
Copper	Pre-defined
Niobium	Pre-defined

Double Click on a spectrum peak using the Show Candidate Elements tool.

Figure 3.28 Exclude elements command in EDS software

3.9. L-PBF and Post Processing for Fatigue Samples

Fatigue tests were conducted in a parallel study using the L-PBF parameters and heat treatment strategy combination that were determined to provide optimal sample microstructure by this study. The print parameters chosen were a scanning speed of 1250 mm/s with energy density of 54.5 J/mm^3. The heat treatment strategy employed was the HIP+SA combination. The exact values for L-PBF and heat treat parameters for HIP and SA can be found in Table 3.1, Table 3.5, and Table 3.6, respectively. Specimen were printed with geometry that complied with ASTM E466 standard for force-controlled constant amplitude axial fatigue testing.

3.10. Fatigue Testing

Fatigue testing was performed on the MTS 100KIP UTM Fatigue System according to the ASTM E466 standard for force-controlled constant amplitude axial fatigue testing. Twelve samples were produced and were labeled A1-A12. Table 3.10 contains the loads and frequencies used for the range of axial fatigue experiments.

Table 3.10 Axial fatigue testing parameters

Load (MPa)	Frequency (Hz)
246	30
422	30
528	30
563	30
598	30
633	30
668	30

Two samples were broken at each load except for the lowest loads of 246 MPa and 422 MPa. Fracture surfaces were analyzed using SEM and EDS systems and preliminary results were reported for this study with the purpose of validating the microstructure study.

4. RESULTS AND DISCUSSION

4.1. Porosity

The amount of porosity was observed on the polished and unetched surface of each of the even labeled samples. Referring to Figure 4.1, the AP samples exhibited the largest amounts of porosity forming all across the samples. Higher pore density around the edges of the parts was expected due to the rapid cooling rates during the print process as well as insufficient energy that failed to melt and join a molten metal bead with previously printed layers [5–7]. The incipient melting temperature (IMT) was reported in the range of 1160-1180ºC for IN718 [34–36]. The HG treatment at 980ºC did not allow the temperature of the material to reach this range to completely re-melt porosities; however, a reduction of porosity was observed in the HG samples since the homogenizing temperature was higher than half of the melting temperature (1703ºK) that facilitated diffusion and closure of small pores. The sample center zones, of samples subjected to HIP, were virtually free of porosities under optical microscope as reported from published literature [29,30]. The HIP temperature of 1163ºC, exceeding the IMT of IN718, allowed diffusion and local melting at defects, such as pores or shrinkage cavities, and reduced porosity.

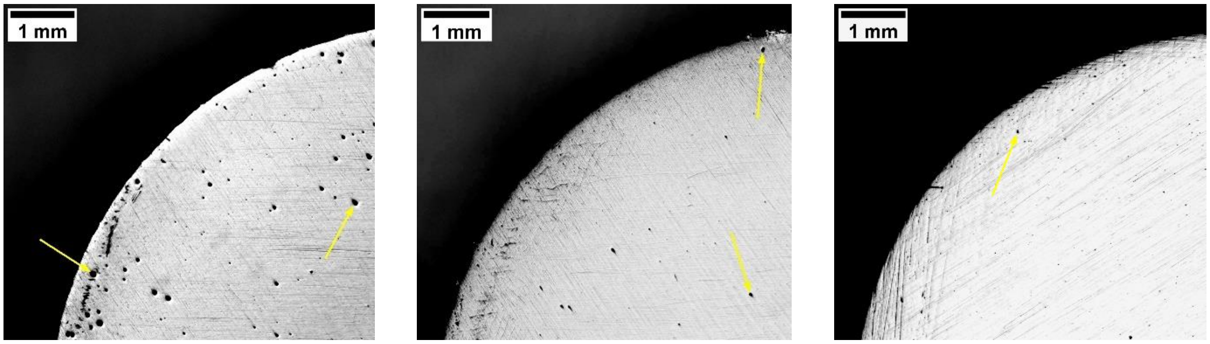

(a) AP **(b) HG** **(c) HG+HIP**

Figure 4.1 Porosity at the edge and center of 45.5 J/mm^3, 1500mm/s samples a) A2, b) A4, and c) A6 with arrows to represent typical pores

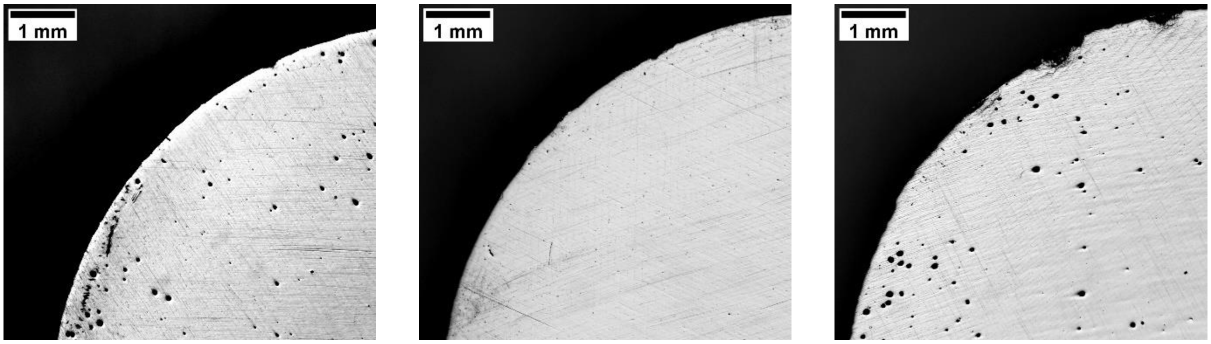

(a) 45.5 J/mm^3, 1500mm/s **(b) 54.5 J/mm^3, 1250mm/s** **(c) 68.2 J/mm^3, 1000mm/s**

Figure 4.2 Effect of energy density on pore distribution of samples a) A2, b) B2, and c) C2

The effects of the varying print parameters, specifically the scanning speed and energy density, were observed in terms of the porosity present in the samples (Figure 4.1). Due to the HIP process removing the visual porosities, the effects of the print parameters on the porosity were mainly studied in the AP and HG sample groups.

- Referring to Figure 4.2a, the samples in group A with the lowest energy density (45.5 J/mm^3) exhibited the largest amount of visual surface porosity. The faster scanning speed of 1500 mm/s on sample A2 (i) caused fast cooling of a molten bead, (ii) trapped pores in the liquid state, therefore resulted in more pores. The faster cooling rate near the edges enhanced this process and produced more pores near the edges.

- Referring to Figure 4.2b, the samples in group B, subjected to higher energy density (54.5 J/mm^3), showed significant pore reduction, and agreed with published literature that concluded an increase in the energy density would reduce the porosity density [8,9]. The higher energy and slower scanning speed allowed larger molten beads to join different layers; the slower cooling rate allowed voids to escape in the molten pool.
- Referring to Figure 4.2c, the samples in group C, subjected to the largest energy density (68.2 J/mm^3) but resulted in more pores compared to the sample B in Figure 4.2b. The slower scanning speed of 1000 mm/s created longer exposure to the laser which melted and boiled the molten bead below the laser beam, the additional voids (keyholes) were trapped in metal upon solidification.

Large energy density values are associated with the reintroduction of porosities, but this value for energy density was well below the values in previous studies that saw increased porosity [8,9]. This could be due to the varying of other printing parameters that affect energy density in those studies, where all parameters outside of scanning speed were held constant in this study. Though group C samples had a lower energy density value than other studies, the other print parameters that were altered in those studies could be responsible for the changes in porosity, not simply the energy density. The formation mechanisms of these spherical porosities stem from the entrapped gases in the molten pool that are a direct result of excessive energy input and other unstable process conditions [5]. By holding all parameters constant other than scanning speed, this study decreased the possibility of unstable conditions allowed for better understanding of the effects of the speed parameter. Gong et al. discussed a speed window for L-PBF'ed Ti-6Al-4V parts in which there were no apparent porosities in samples printed at speeds within 600mm/s to 1600mm/s. Samples printed with a speed below 600mm/s exhibited pores due to an over exposure to the laser which caused boiling in the metal where speeds above 1600mm/s resulted in pores caused by the faster cooling rates of the metal [6]. Though a different material, this trend was present in this study as the 1500mm/s scanning speed in group A samples did not provide sufficient energy density to fuse any present voids and the 1000mm/s speed in group C resulted in over exposure to the higher energy density that only accelerated pore formation as the material released more gases.

Statistical analysis was performed to characterize the porosity. The distributions of pores for all samples in groups A, B, and C and the effect of printing parameters are shown in Figure 4.3. Table 4.1 lists the total pore area, percentage porosity (calculated using Equation 3), average pore diameter, and the total mean of the pore diameters for each group (Figure 4.4a). The probability densities of pore diameters in Figure 4.3 allowed for a more in-depth understanding of the pores present in each sample group. Before HIP, the large majority of porosities in group B samples (54.5 J/mm^3) fell into the range of 15-20µm where groups A and C samples (45.5 J/mm^3 and 68.2 J/mm^3, respectively) contained pores reaching well over 100µm in diameter. This was further reinforced in the data shown in Figure 4.4a which was obtained by calculating the mean of the average pore diameter values of the samples within their respective energy density group (Table 4.1), as well as their standard deviation values. Print parameter B samples contained the smallest mean pore diameter (15.58µm) as well as the smallest deviation (5.16µm) which supported that the optimized energy density value of 54.5 J/mm^3 should be used for minimization of pores.

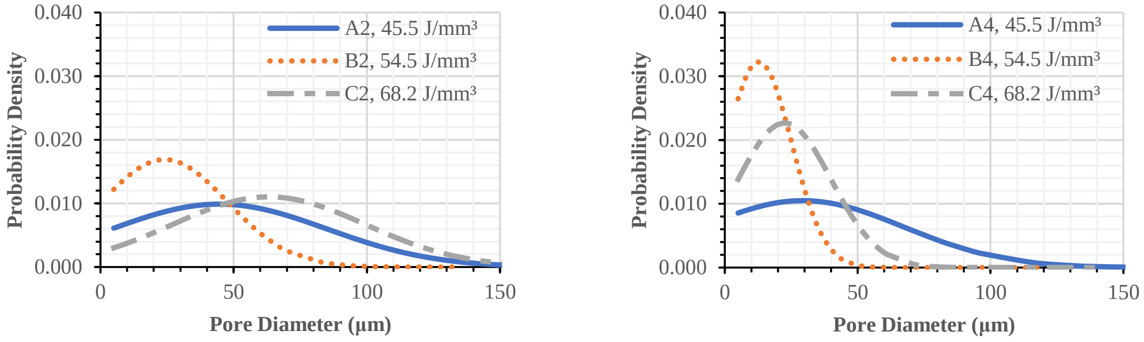

(a) AP **(b) HG**

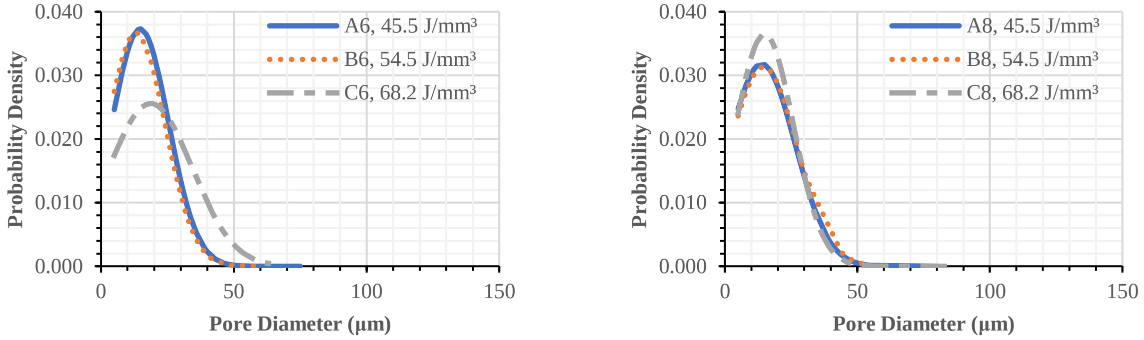

(c) HG+HIP **(d) HG+HIP+SA**

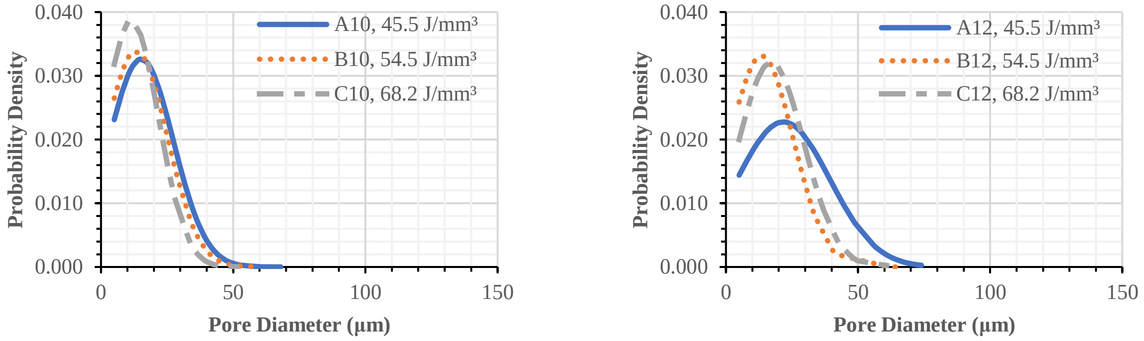

(e) HIP **(f) HIP+SA**

Figure 4.3 Effect of post processing on pore diameter distribution

Table 4.1 Porosity data for each sample grouped by energy density during print process

Sample	Energy Density (J/mm^3)	Total Pore Area (mm^2)	% Porosity	Average Pore Diameter (μm)
A2	45.5	0.864	0.742	44.60
A4		0.226	0.234	29.33
A6		0.085	0.088	14.75
A8		0.023	0.022	13.91
A10		0.056	0.060	15.15
A12		0.051	0.064	12.90
B2	54.5	0.114	0.098	26.05
B4		0.099	0.100	12.81
B6		0.025	0.030	13.29
B8		0.011	0.011	14.58
B10		0.020	0.028	13.29
B12		0.020	0.027	13.45
C2	68.2	1.277	1.108	63.24
C4		0.129	0.140	22.49
C6		0.050	0.051	18.67
C8		0.064	0.060	14.98
C10		0.020	0.029	11.45
C12		0.022	0.025	17.09

Wang et al. studied L-PBF’ed IN718 and used Equation (2) to study the effects of linear energy density on porosity density and found that a power of 276W and a scanning speed of 786mm/s were the optimal values in reducing porosity [7]. These values produced a LED value of 0.35 J/mm which, assuming the same hatch distance (0.11mm) and thickness (0.06mm) in this study and using Equation (1), would be equivalent to an energy density value of 53.2 J/mm^3 which was similar to the group B parameter of 54.5 J/mm^3 used in this study.

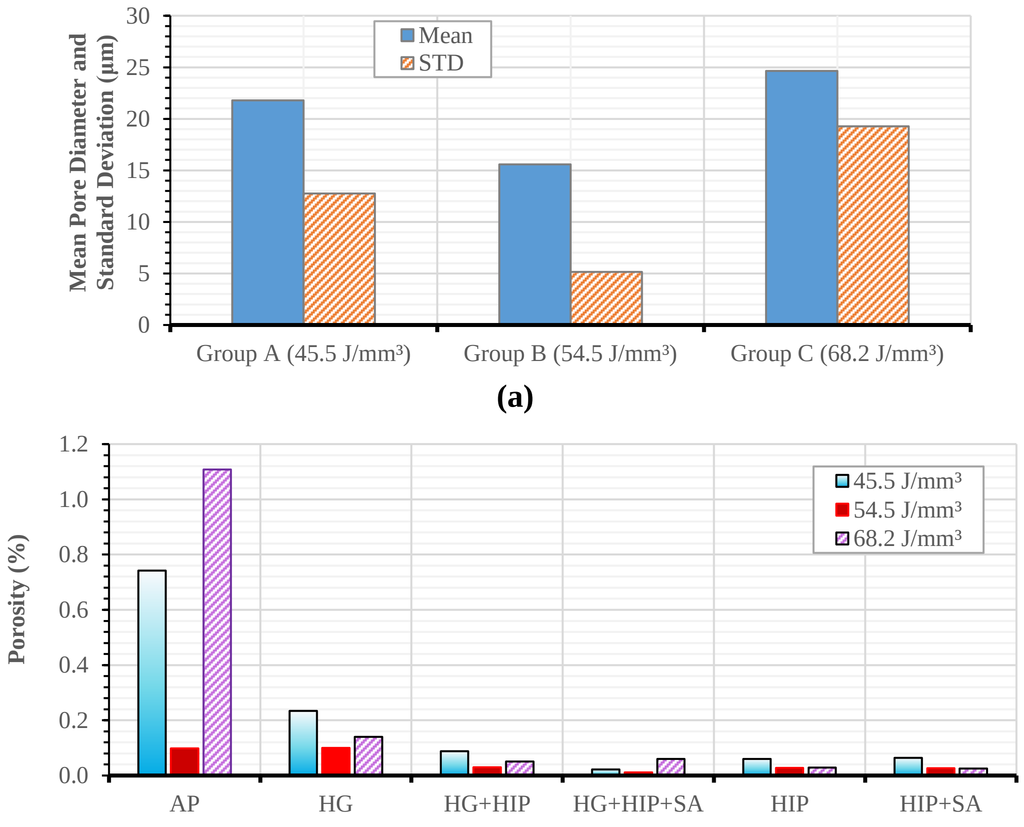

(a)

(b)

Figure 4.4 Porosity resulted from (a) energy density, and (b) post processing

Sample C2 exhibited the largest values for porous area (1.277 mm^2), % porosity (1.108%), and the average pore diameter (63.24µm) as shown in Figure 4.2 and Table 4.1. Homogenization reduced the average pore diameter for the samples the % porosity (Figure 4.4b). With the introduction of the HIP process (samples A6, B6, and C6), there was a reduction in both total pore area and % porosity of nearly 60% across all samples. Any sample which included HIP in its heat treatment strategy exhibited consistent results but print group B achieved the lowest values for total pore area and % porosity through all treatment processes. This trend was observed in another study as well [18]. Popovich et al. [28] found that the porosity of SLM IN718 decreased significantly for samples after HIP. For samples subjected to only heat treatment at 850ºC after printing, porosity was found to be 0.15% and 0.29% after scanning with laser power at 250 and 950 W, respectively. HIP of these samples reduced the porosity further to 0.02% and 0.06% respectively [28]. Table 4.1 shows % porosity values after HG treatment at 980ºC being 0.234%, 0.100% and 0.140% for print groups A, B, and C, respectively. With the introduction of HIP, those values decreased to 0.088%, 0.030%, and 0.051% and remained around these values for all subsequent heat treat groups that included HIP (Figure 4.4b). Because the HIP process was conducted at 1163ºC, which is within the IMT range of 1160-1180ºC for IN718 [34–36], most pores/voids still present after printing or HG treatment were able to close. In all heat treatment groups outside of the HG+HIP+SA and HIP samples had the largest proportion of pores measuring less than ~15µm. The HG and HIP+SA processes affected print group A the most negatively while the AP and HG+HIP processes had this effect on print group C. The highest probability density for group B remained near 15µm for each treatment strategy after printing with an additional reduction in the max pore diameter observed after any post processing treatment. Based on porosity alone, group B showed the lowest amount of surface porosity while also exhibiting the smallest and most consistent pore size when printing with energy density at 54.5 J/mm^3.

4.2. Microhardness

Vickers microhardness (VH) test locations were chosen randomly away from the edges of the cylindrical samples. The microhardness data along with the Rockwell B (RB) hardness data are shown in Figure 4.5.

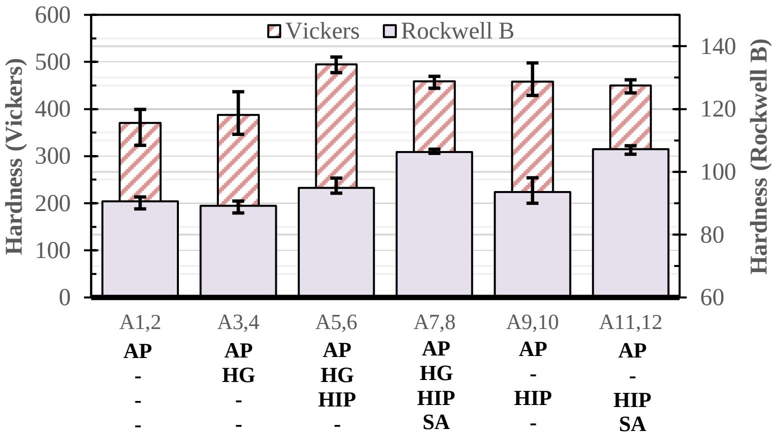

(a) Group A (45.5 J/mm^3)

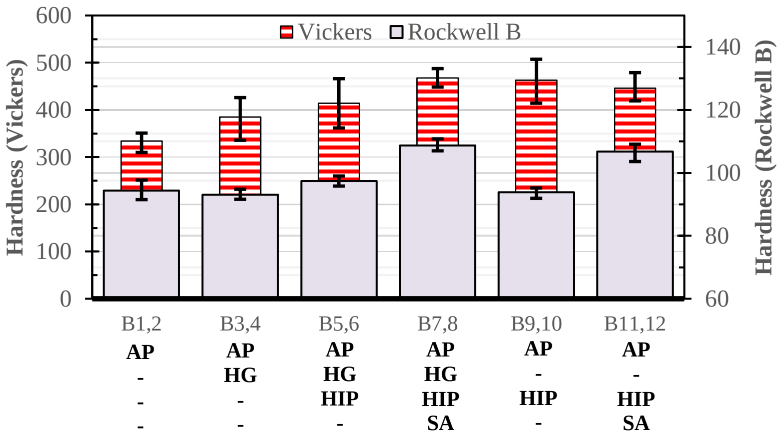

(b) Group B (54.5 J/mm^3)

Figure 4.5 Effects of energy density and post processing on hardness of L-PBF IN718

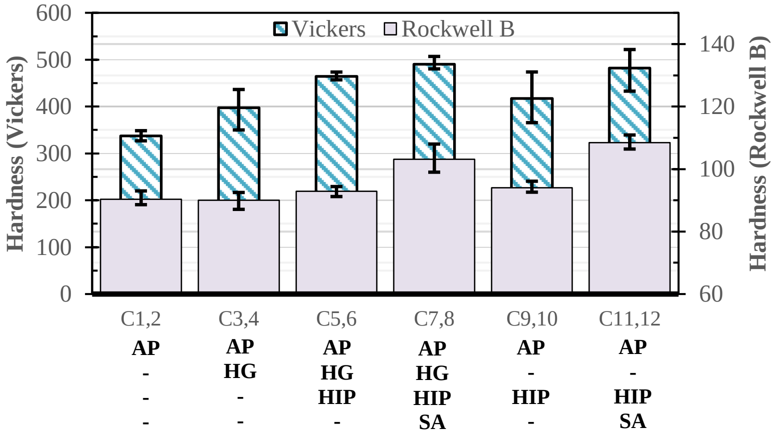

(c) Group C (68.2 J/mm^3)

Figure 4.5 (Continued) Effects of energy density and post processing on hardness of L-PBF IN718

Similar trends were seen for data in both VH and RB scale. HG+HIP+SA samples exhibited the largest hardness values of 468 ± 13 HV and 494 ± 5 HV across groups B and C, respectively. The same result was observed in another study where values of 468 HV and 451 HV were observed for samples fabricated by laser power at 250W and 950W, respectively [28]. The complete hardness data for each sample can be found in Table 5.1 in the Appendix B. For AP samples, only sample A2 (389 ± 5 HV) was able to exceed previous hardness values for cast or wrought IN718 (353 HV) [37,38]. Though higher values were achieved in groups A and C, group B was still chosen as the optimal print parameter group as such high values could be responsible for creating a brittle material and a reduction in elongation % below the ASTM standard as observed in a previous study with hardness values nearing 500 HV [39].

There were not significant differences among data for the different print parameter groups and all followed similar trends in increasing values which showed the energy density has little to no effect on the microhardness. This was supported in other studies who also observed no significant change in hardness values across differing energy density values [8,18]. Samples 7,8 and 11,12 for all print parameter groups exhibited the highest RB values (Table 5.1). Mean RB values for samples 7,8 and 11,12 for all print groups were calculated to be 106.1 ± 1.4 and 107.6 ± 0.6, respectively, with the HIP+SA treatment producing the higher and more consistent RB value. VH and RB are both measures of the same hardness, they differ in their penetration depth during testing. VH is a shallow measurement and is dependent on the surface of the sample, meaning that the value could change based on the surface quality. RB values result from a deeper test penetration and are therefore more representative of the material's properties. Heat treated samples in group B showed superior hardness values, without signs of becoming an overly brittle material, to those of cast and wrought IN718 [37,38].

4.3. Microstructure

Both optical and electron microscopy were used to observe the microstructure and effect of post processing. The etching gradient on the surface of the samples (with none or light etching at the top of the surface, very heavy over-etching at the bottom, and standard etching in between) caused certain elements of the microstructure to be more apparent. In the over-etched region on the AP samples, precipitates on the surface had been removed by the etchant and much deeper pores and void defects were revealed (Figure 4.6a and Figure 4.6b). Grain boundaries appeared much thicker and almost uneven as the etchant partially etched certain grains more than others in this region (Figure 4.6c). Near the top of the surface and into the standard etched area, the grain boundaries and precipitates were observed for all of the samples (Figure 4.7). OM images of the AP samples showed a large number of defects all throughout the surface of the samples, which was expected based on the presence of porosity before etching, while also having the smallest grain size (~10-20 μm).

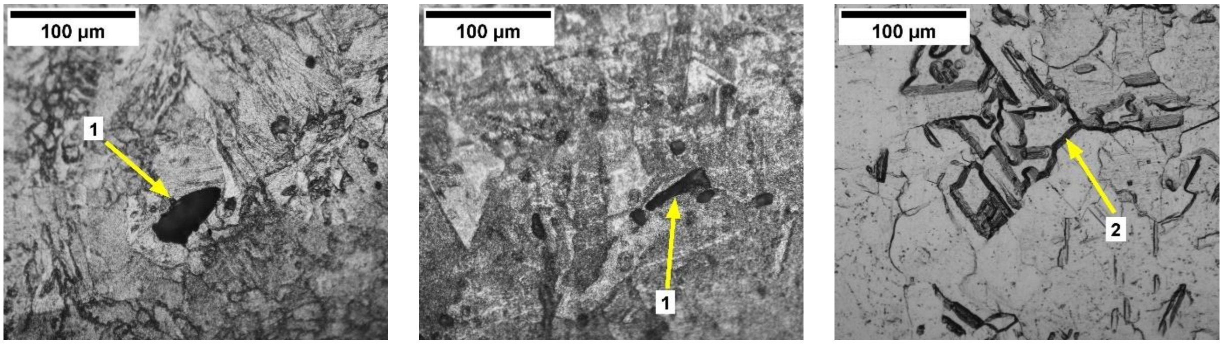

(a) AP **(b) HG** **(c) HG+HIP**

Figure 4.6 Optical images of etched group B (54.5 J/mm^3) samples with (1) surface void defects and (2) uneven grain boundaries due to etching time

HG samples exhibited larger grains (~30μm) but a similar number of void defects as the AP samples, though not as large (Figure 4.7b). With the addition of the HIP process, the majority of the circular pores were removed as expected along with many of the large nonuniform defects. Grains grew closer to 50μm after HG+HIP treatment and exhibit more clear boundaries (Figure 4.7c). Defined grain boundaries (grain size of ~60-80μm) and very few defects were observed in the microstructure of the HG+HIP+SA samples (Figure 4.7d). Where the HG and HIP treatments have the greater effect on the fusion of pores and defects, the solution treatment effects were more apparent in the strengthening of the grain boundaries and grain growth. This idea was supported in the HIP samples, as it was observed that the microstructure returned to a similar state as the HG+HIP samples and the reintroduction of the solution treatment in the HIP+SA samples showed much larger grains reaching over 100μm (Figure 4.7e and Figure 4.7f). The HG+HIP+SA and HIP+SA samples provided the best microstructural results under the OM inspection, but it is necessary to investigate deeper than on the visual level.

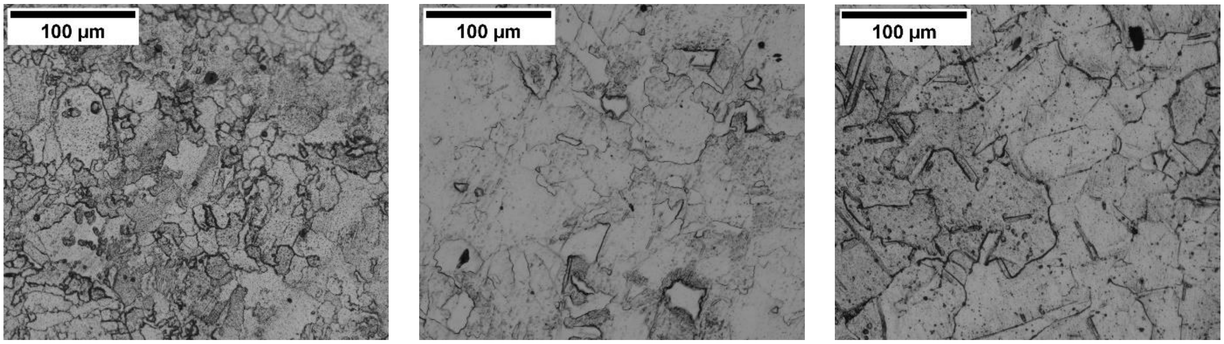

(a) AP **(b) HG** **(c) HG+HIP**

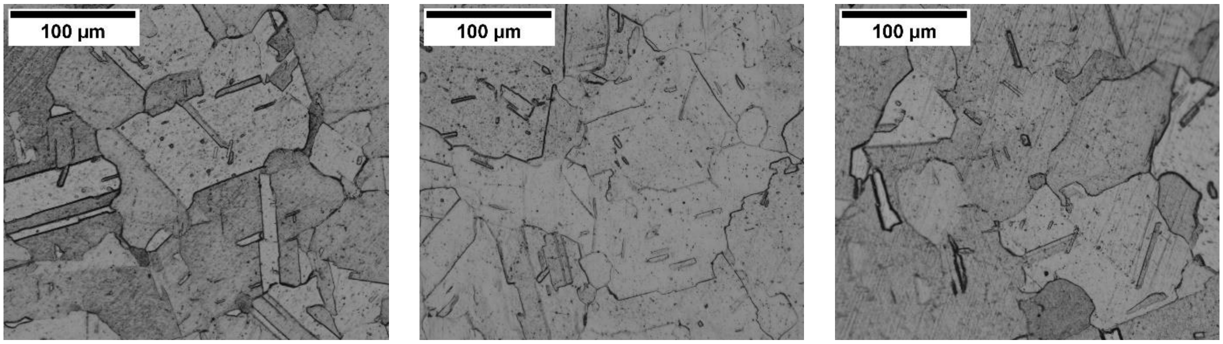

(d) HG+HIP+SA **(e) HIP** **(f) HIP+SA**

Figure 4.7 Optical image of microstructure and grain growth after heat treatment in etched group B (54.5 J/mm^3) samples

In comparing the number of defects visible under the OM for each of the sample groups, the theory established in the porosity and microhardness studies was only supported further showing that the print parameters for group B samples would produce the smallest number of surface defects. After subsequent HIP treatments, all of the sample groups exhibited similar numbers of surface defects and the microstructures after the other heat treat strategies for each A, B, and C group were similar. This meant that the distinguishing factors could only be observed in the AP and HG samples, in which the print parameter group B exhibited the optimal results. Based on this observation, the group B samples were chosen for further SEM analysis.

Through SEM and EDS analysis, the AP sample showed a large amount of Laves phase precipitates distributed nonuniformly around the surface of the part (Figure 4.8). These phases were identified through EDS analysis of Nb content at the specified locations which matched values previously reported (~10-20wt% Nb) [28,36].

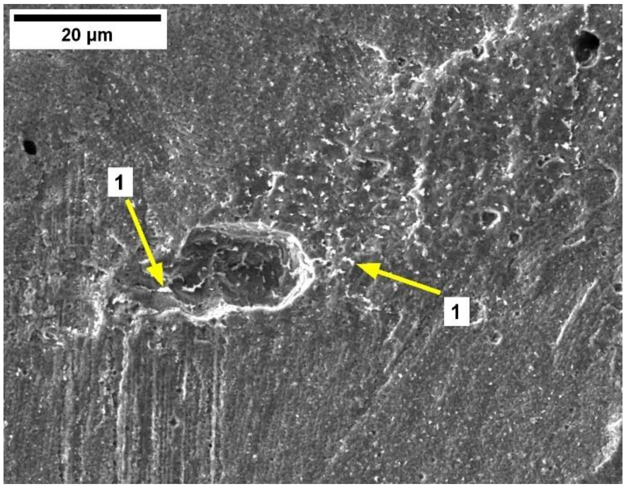

Figure 4.8 Nonuniform distribution of (1) Laves phase in AP sample B1 (54.5 J/mm^3)

Many previous studies found Laves phase in as-printed samples that in turn weakened the mechanical properties of the material [13,36,40,41]. These detrimental particles were accompanied by a large amount of Al_2O_3 defects ranging from 15-20μm (Figure 4.9). Brittle oxide formations were previously reported in another study [28]. The formation of these oxides is a result of difficult to control factors in the L-PBF environment ranging from oxides in recycled powder, or oxide formation on the build plate. The substantial amounts of porosity that were observed under the OM were again observed under the SEM, only supporting that data. The chemical composition of the oxide defect along with the matrix from Figure 4.9 is listed in Table 4.2. Elemental wt% for Al, O, and Ti in the oxide reached values of 41.4%, 31.9%, and 12.7%, respectively, compared to the matrix values of 0.7%, 0%, and 1.1%. These values were fairly consistent among all oxide defects. EDS spectra data for points of interest in the AP sample also produced weight values for carbon that were well over the standard (<0.8%) for IN718 material. In the matrix, the carbon wt% reaches a value of ~10%. This trend is evident in all other data points, including Al_2O_3 defects, and is an area of concern in the accuracy of the EDS system. Due to the consistency of the high carbon measurements throughout all of the samples, it was ignored as it did not hinder the ability to identify the defects and phases present in the matrix.

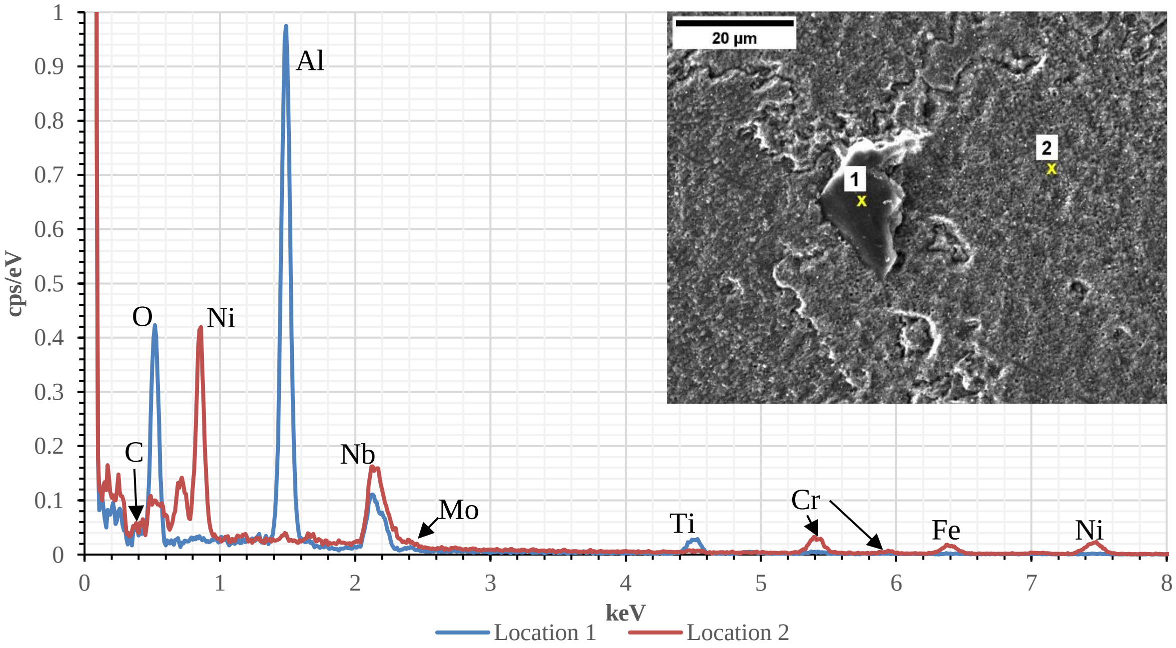

Figure 4.9 EDS spectra data of (1) particle and (2) surrounding matrix in AP B1 sample (54.5 J/mm^3)

Table 4.2 Chemical composition of Al_2O_3 defect compared to matrix in AP sample and IN718 powder [33] (from Figure 4.9)

	Element (wt%)								
	Ni	**Cr**	**Fe**	**C**	**Nb**	**Mo**	**Al**	**O**	**Ti**
Matrix	44.9	16.4	16.1	6.3	5.2	5.2	0.7	0.0	1.1
Particle	3.3	3.3	1.3	4.7	0.0	1.0	41.4	31.9	12.7
IN718	52.0	18.6	19.7	0.02	5.17	3.02	0.49	0.0	0.99

HG sample showed lower amounts and sizes for Al_2O_3 defects and pores were still present, but almost complete dissolution of Laves phase particles was observed with minor precipitates still visible. With the dissolution of the Laves phase precipitates, more uniform Nb-rich carbides were introduced in the matrix in high numbers (Figure 4.10a). A comparison between the Laves phase composition and that of the Nb-rich carbides is shown in Table 4.3 with similar values being reported in a previous study [28]. EDS analysis allowed for the identification between Laves and carbides, as it was difficult to identify them visually. Based on the EDS data in Table 4.3, the carbides differentiated themselves from Laves phases (from Figure 4.10a) with greater increases in wt% of Nb, C, and Ti (46.7wt%, 35.1wt%, and 5.4wt%, respectively) while also exhibiting a drop in Ni composition (5.4wt%). Though the homogenization almost completely dissolved the Laves phases, this heat treatment alone is not sufficient enough to form uniform grains and precipitate carbides evenly in the matrix. A large number of pores were observed along the edges of the cylindrical sample in the area of heavy etching, which was expected due to the extensive time that this part of the sample was subject to the etchant.

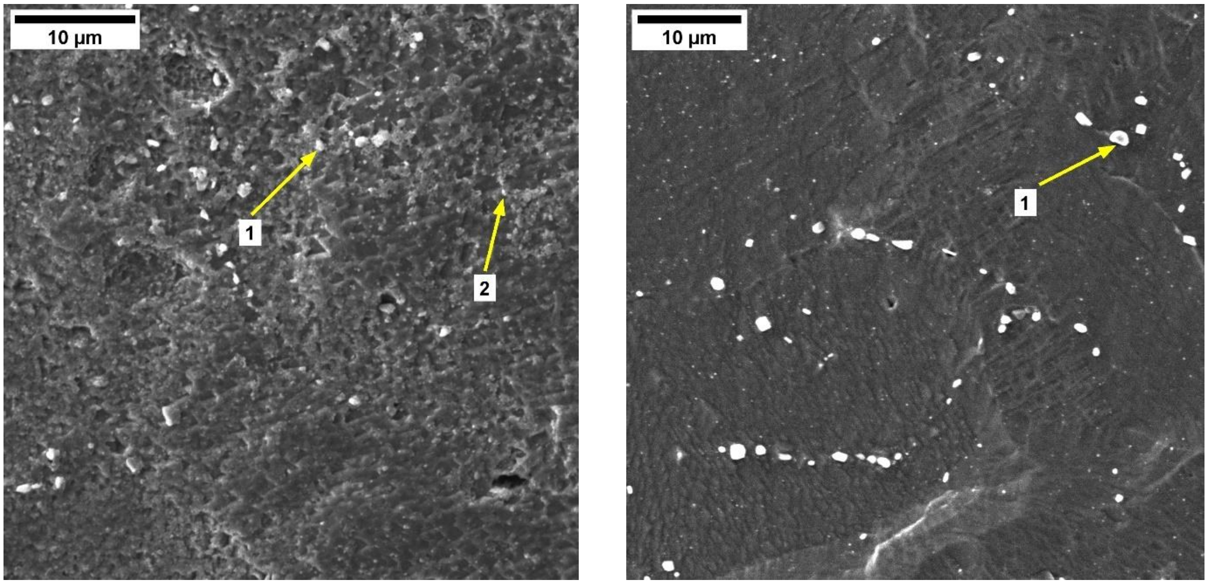

(a) (b)

Figure 4.10 a) (1) Nb-rich carbides and (2) small remaining Laves phase particles in HG B3 sample (54.5 J/mm^3) b) (1) Nb-rich carbide precipitation along grain boundary in HG+HIP B5 sample (54.5 J/mm^3)

Table 4.3 Laves and Nb-rich carbide wt% comparison with IN718 powder [33] (from Figure 4.10a)

	Element (wt%)					
	Ni	**Cr**	**Fe**	**Nb**	**C**	**Ti**
Laves	29.0	10.0	8.6	13.8	20.7	0.8
Nb-rich Carbide	5.4	2.3	1.8	46.7	35.1	5.4
IN718	52.0	18.6	19.7	5.17	0.02	0.99

The HG+HIP sample exhibited comparable results as seen in HG samples but due to the addition of the HIP process, the circular pore defects were no longer present. The reintroduction to a high temperature process also removed any remaining Laves phase particles that were visible in previous samples. Along with the closure of the voids and pores, the size of the defects still present in the sample was reduced to roughly 10µm. The Nb-rich carbides were still present in the matrix, but in smaller amounts and along the grain boundaries (Figure 4.10b). Carbides along the grain boundary provide strength to the material if they are not present in excess [22]. The HG+HIP+SA sample continued the trend of reduction in size and amount of the visible defects with defect sizes around 5-10μm (Figure 4.11). With the addition of the solution and aging treatments, more carbides were observed around the grain boundary and an introduction of δ phases was seen (Figure 4.12). These phases slightly differ in their composition (Table 4.4) but are mainly identified by the rod-like shape. δ phase particles precipitate around the grain boundary and can be beneficial in terms of strength, but the particles were present in high numbers and surrounding grain boundaries which will lead to dislocations in the material during tensile load [15]. The increase in Nb-rich carbides and the excessive amount of δ phase particles proved the sample to be over-heat treated and very brittle, which supports such high hardness values observed in the microhardness study.

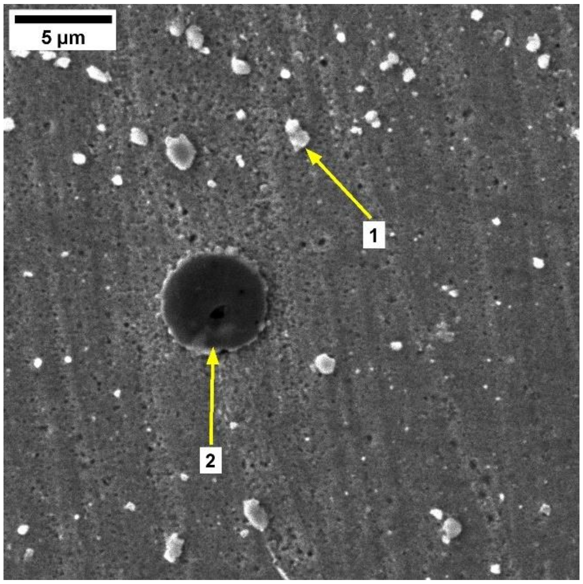

Figure 4.11 Microstructure of B7 sample (54.5 J/mm^3) after HG+HIP+SA showing (1) carbide and (2) aluminum oxide

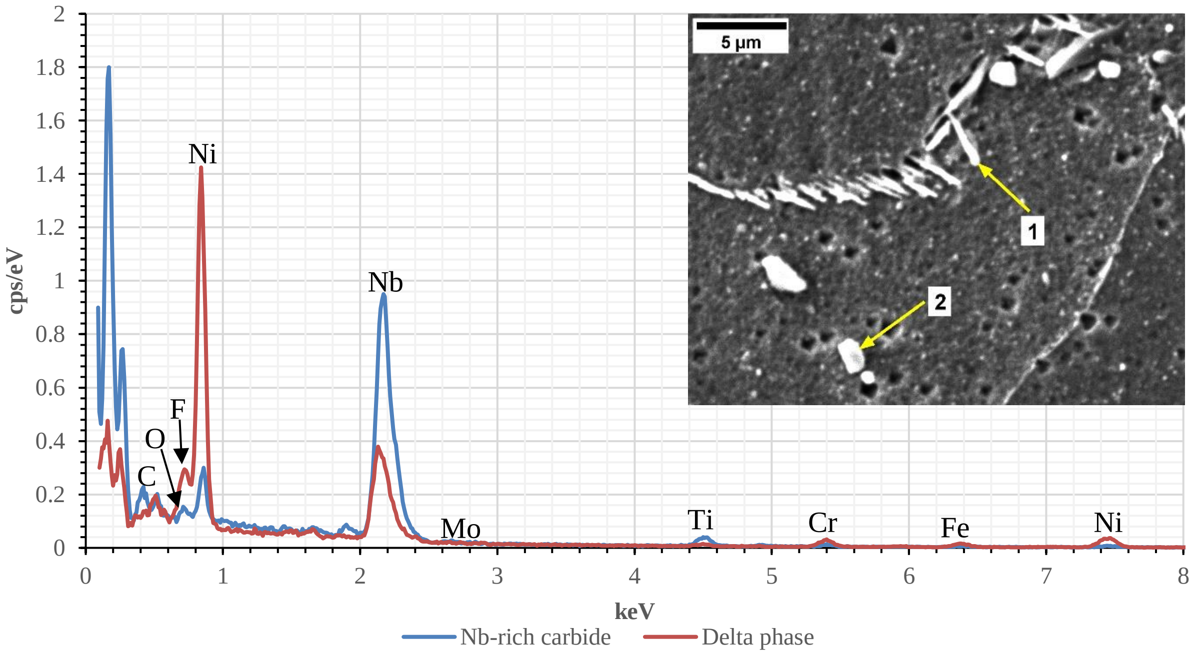

Figure 4.12 EDS spectra for delta particle (1) and carbide (2) in HG+HIP+SA sample

Table 4.4 Composition comparison of Nb-rich carbides, delta phase particles, and IN718 powder [33] (from Figure 4.12)

	Element (wt%)					
	Ni	**Cr**	**Fe**	**Nb**	**C**	**Ti**
Nb-rich Carbide	5.4	2.2	1.9	47.1	32.8	5.6
Delta	45.3	8.7	8.0	13.4	12.7	1.5
IN718	52.0	18.6	19.7	5.17	0.02	0.99

Though two heat treatments were not conducted, the HIP sample was still able to show the same limited number of pores/voids as the previous samples while keeping the size of the present defects around 5-10µm. Around the lower edge of the sample, large porous defects were observed. These porosities were a result of excessive exposure to the etchant as they were only present at the lower edge, not at the top where no etching was done. The number of Nb-rich precipitates did increase however (Figure 4.13a), though there was no presence of Laves phase, showing that the HIP process alone is capable of dissolving Laves in the matrix. HIP can be used to dissolve Laves phases, but it is still necessary to have additional heat treatments to aid in the more uniform distribution of the Nb-rich carbides.

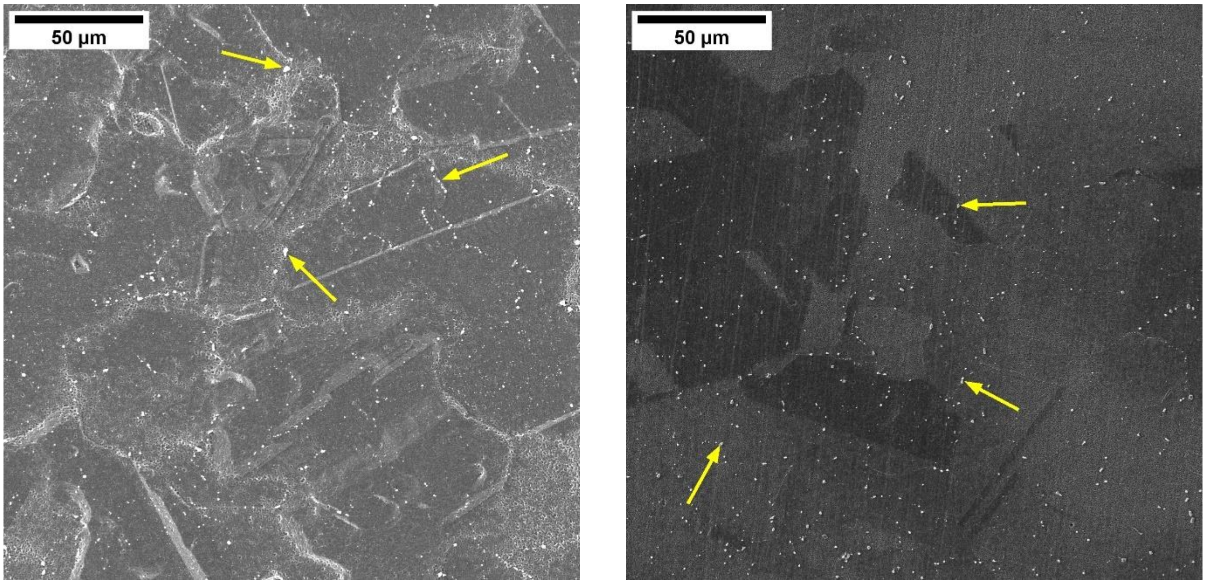

(a) **(b)**

Figure 4.13 Carbide distribution (denoted by arrows) in matrix of a) HIP sample and b) HIP+SA sample

The lowest number of visual defects was observed in the HIP+SA sample. The HIP process closed any circular pores and other voids that were present while also dissolving the Laves phase particles. With the addition of the solution and aging treatments, the Nb-rich carbides were more uniformly distributed around the grain boundaries (Figure 4.13b). Al_2O_3 defects were still present but were greatly reduced in size (roughly 5µm) and number. Based on the number and size of visual defects, the ability to close pores and voids after the L-PBF process, and evenly distribute the strengthening particles around the grain boundaries, the HIP+SA sample exhibited the optimal results when compared to the other combinations of heat treatments.

4.3.1. Recommendation

Based on the porosity analysis, the L-PBF print parameters of 1250 mm/s scanning speed and an energy density value of 54.5 J/mm^3 were chosen to provide the lowest amount of porosity as well as porosity with the smallest average diameter when present. The hardness study and microstructure with SEM/EDS analysis allowed for a better understanding of the effects of the employed heat treatment strategies. The results from these studies showed that the HIP+SA treatment would allow for the optimal microstructure in the L-PBF IN718. Homogenization provided porosity values that were similar to those of HIP samples, but the addition of the solution and aging that provided the additional strengthening of the grain boundaries was necessary to increase strength properties of the material and the only the HIP process was directly paired with SA. Therefore, the L-PBF parameters mentioned above, and the heat treatment strategy proven to produce optimal microstructure were used in the fabrication and post processing for fatigue specimen in the final stages of this experiment.

4.4. Fatigue

Fatigue data validated the print parameter and post processing recommendations that stemmed from the microstructure study. Results reported in this study were intended to be preliminary, so the nature/cause of fracture in the samples was not covered. Full analysis of the fatigue of L-PBF IN718 after the HIP+SA treatment was completed by another student in a concurrent study.

New L-PBF IN718 samples, following the print parameters of group B (1250 mm/s scanning speed and 54.5 J/mm^3 energy density), were subject to the HIP+SA treatment after printing and showed significant improved axial fatigue life when compared to the performance of the AP L-PBF samples. Figure 4.14 shows the compared fatigue performance of the HIP+SA samples with the L-PBF samples in their AP state at increasing axial loads.

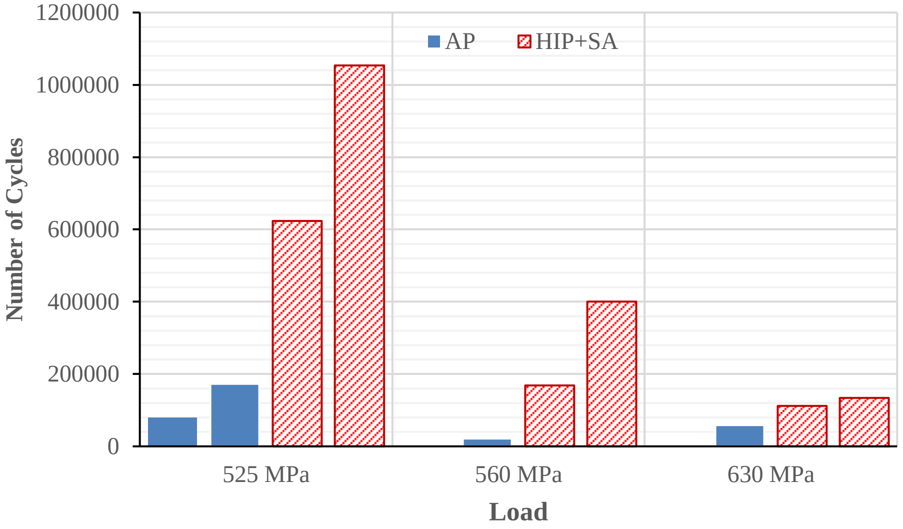

Figure 4.14 Fatigue performance of HIP+SA samples compared to AP samples [16] at loads of 525MPa, 560MPa, and 630MPa

In typical fatigue testing, samples that reached over one million cycles were considered "runout" at stress level below fatigue endurance limit. At 525 MPa, the fatigue life increased 260% after implementing the HIP+SA treatment strategy. At 630 MPa, the fatigue life improved by nearly 128%. An improvement in fatigue performance after appropriate post printing heat treatment was also observed by others [31,42]. It was the thermal-induced microstructural changes that affected the alloy's mechanical properties, therefore, fatigue properties. The S-N curve for all twelve fatigue samples can be found in Figure 4.15 below.

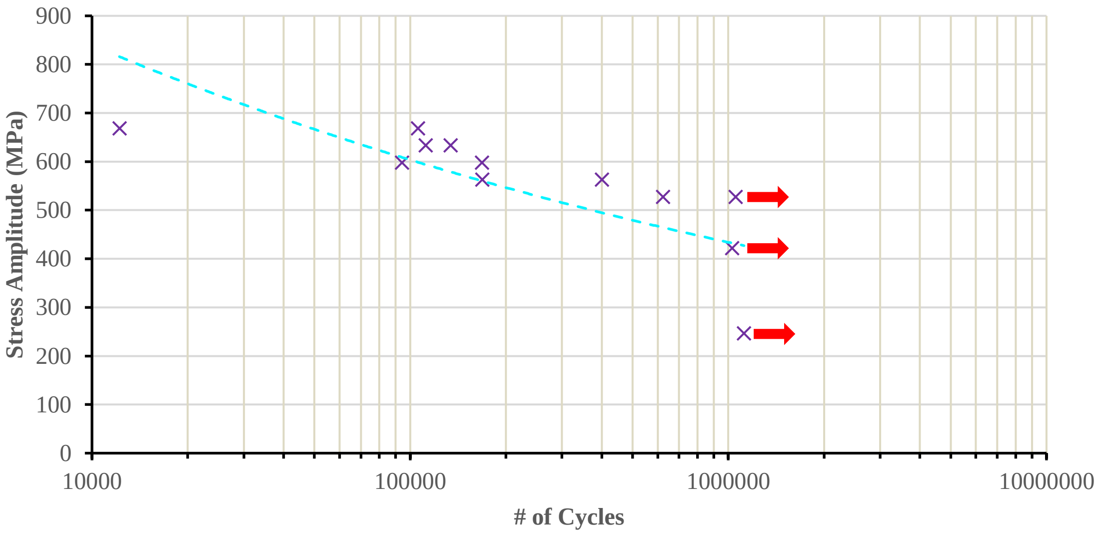

Figure 4.15 S-N curve for HIP+SA L-PBF IN718 fatigue samples

All samples were able to exceed the fatigue performance for L-PBF IN718 samples in their AP state. Samples A1, A2, and A9, reached 10^6 cycles which was established as the runout (indicated by the arrows in Figure 4.15).

The microstructure of the fractured samples showed comparable results to those observed in the initial microstructure study. Since Laves phases were not found in the HIP+SA fatigue samples, this suggested that the combination of HIP and solution heat treat was sufficient to dissolve the Laves phases. Although carbides particles were not found on some fatigue samples, but spherical Al_2O_3 particles identified by EDS were still present nearing ~5µm (Figure 4.16).

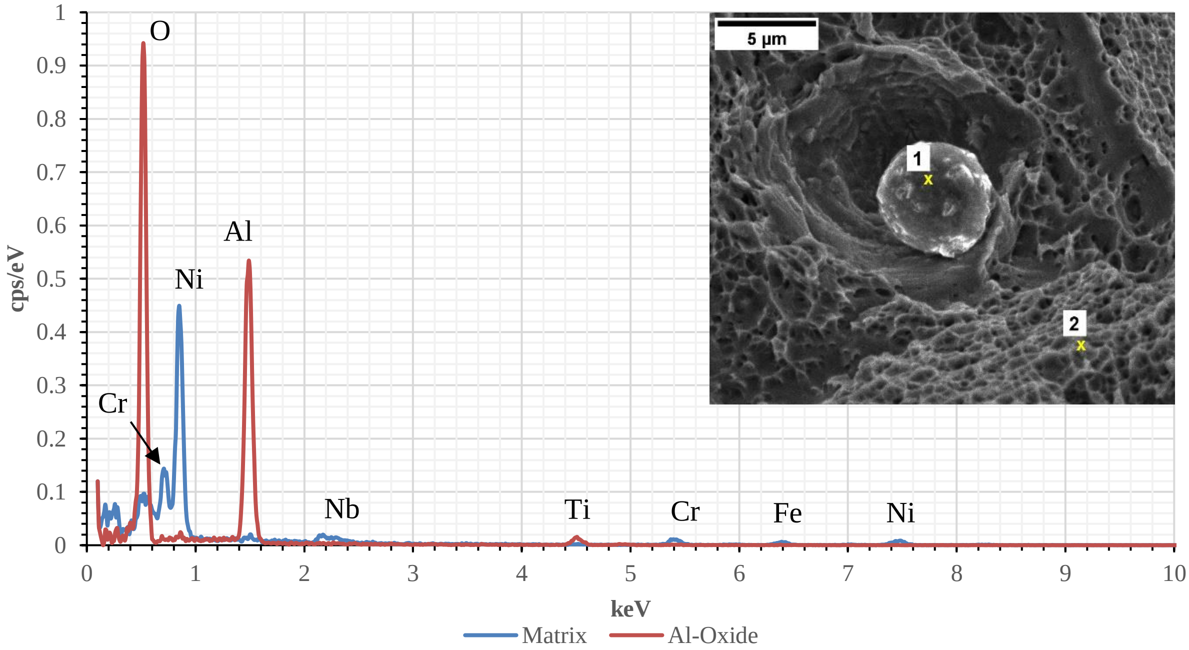

Figure 4.16 EDS spectra data of (1) spherical inclusion and (2) surrounding matrix. Sample A12, 630 MPa, HIP+SA treatment.

These oxides, that de-bonded from the matrix, were responsible for initial crack formation and propagation that eventually fractured a fatigue specimen. The crack fronts propagated but were hindered by entangled dislocations at the γ' and γ'' precipitates in the matrix. Uniform distribution and optimal size of these precipitates effectively slowed down the crack growth rate and enhanced the fatigue performance of additively manufactured IN718.

5. CONCLUSIONS

Different combinations of prominent heat treatment process were executed on samples of IN718 that were fabricated using varying L-PBF print parameters to achieve optimal fatigue performance. This study showed:

1) Operating the L-PBF process with a scanning speed of 1250 mm/s and energy density of 54.5 J/mm^3 provided the lowest amount of surface porosities while having the smallest pore diameters across samples. Printing below or above the optimal energy density resulted in an increase in the number and size of pores in the samples.
2) The combination of homogenization, hot isostatic pressing, solution treating, and aging minimized Laves phases while increasing hardness from 93 to 109 Rockwell B. Comparable results, however, were obtained without the homogenizing step while reducing the growth of the δ precipitates in the grain boundaries.
3) Both hardness and preliminary fatigue testing validated the expected microstructure and mechanical performance of the optimal post process (isostatic pressing, solution and aging) on 3D printed IN718. Although Laves phases were minimized after the optimal thermal treatment, some detrimental carbides and aluminum oxides were still present in the microstructure.

REFERENCES

[1] Voort, G. Vander, 1991, *Inconel 718 (Alloy) and Modified Inconel 718*.

[2] Deng, D., 2018, *Additively Manufactured Inconel 718: And Microstructures Mechanical Properties*.

[3] Sali, A. R., Patel, V., Hyder, J., Hyder, D., Corliss, M., and Hung, W., 2021, "Electron-Beam Welding of Laser Powder-Bed-Fused Inconel 718," International Journal of Engineering Materials and Manufacture, **6**(3), pp. 209–224.

[4] Jain, S., Corliss, M., Tai, B., and Hung, W. N., 2019, "Electrochemical Polishing of Selective Laser Melted Inconel 718," Elsevier B.V., pp. 239–246.

[5] Zhang, B., Li, Y., and Bai, Q., 2017, "Defect Formation Mechanisms in Selective Laser Melting: A Review," Chinese Journal of Mechanical Engineering (English Edition), **30**(3), pp. 515–527.

[6] Gong, H., Rafi, K., Gu, H., Starr, T., and Stucker, B., 2014, "Analysis of Defect Generation in Ti-6Al-4V Parts Made Using Powder Bed Fusion Additive Manufacturing Processes," Addit Manuf, **1**, pp. 87–98.

[7] Wang, F., del Bosque, H., Hyder, J., Corliss, M., and Nguyen Hung, W., 2019, *ScienceDirect Experimental Investigation of Porosity Distribution in Selective Laser Melted Inconel 718*.

[8] Caiazzo, F., Alfieri, V., and Casalino, G., 2020, "On the Relevance of Volumetric Energy Density in the Investigation of Inconel 718 Laser Powder Bed Fusion," Materials, **13**(3).

[9] Cherry, J. A., Davies, H. M., Mehmood, S., Lavery, N. P., Brown, S. G. R., and Sienz, J., 2015, “Investigation into the Effect of Process Parameters on Microstructural and Physical Properties of 316L Stainless Steel Parts by Selective Laser Melting,” International Journal of Advanced Manufacturing Technology, **76**(5–8), pp. 869–879.

[10] Carlson, R. G., and Radavich, J. F., 1989, *Microstructural Characterization of Cast 718*.

[11] Patel, V., Sali, A., Hyder, J., Corliss, M., Hyder, D., and Hung, W., 2020, “Electron Beam Welding of Inconel 718,” Elsevier B.V., pp. 428–435.

[12] Knorovsky, G. A., Cieslak, M. J., Headley, T. J., Romig, A. D., and Hammetter, W. E., *INCONEL 718 A Solidification Diagram*.

[13] Schirra, J. J., Caless, R. H., and Hatala, R. W., 1991, “The Effect of Laves Phase on the Mechanical Properties of Wrough and Cast + HIP Inconel 718.”

[14] Kuo, Y. L., Horikawa, S., and Kakehi, K., 2017, “The Effect of Interdendritic δ Phase on the Mechanical Properties of Alloy 718 Built up by Additive Manufacturing,” Mater Des, **116**, pp. 411–418.

[15] Gao, Y., Zhang, D., Cao, M., Chen, R., Feng, Z., Poprawe, R., Schleifenbaum, J. H., and Ziegler, S., 2019, “Effect of δ Phase on High Temperature Mechanical Performances of Inconel 718 Fabricated with SLM Process,” Materials Science and Engineering A, **767**.

[16] Balasubramanian, S.-S., Philpott, C., Hyder, J., Corliss, M., Tai, B., and Hung, W. N., 2020, “Testing Techniques and Fatigue of Additively Manufactured Inconel 718 – A Review,” International Journal of Engineering Materials and Manufacture, **5**(4), pp. 156–194.

[17] Balasubramanian, S. S., Philpott, C., Hyder, J., Corliss, M., Tai, B., and Hung, W., 2021, “Novel Fatigue Tester for Additively Manufactured Metals,” *Procedia Manufacturing,* Elsevier B.V., pp. 525–534.

[18] Moussaoui, K., Rubio, W., Mousseigne, M., Sultan, T., and Rezai, F., 2018, “Effects of Selective Laser Melting Additive Manufacturing Parameters of Inconel 718 on Porosity, Microstructure and Mechanical Properties,” Materials Science and Engineering A, **735**, pp. 182–190.

[19] Xia, M., Gu, D., Yu, G., Dai, D., Chen, H., and Shi, Q., 2017, “Porosity Evolution and Its Thermodynamic Mechanism of Randomly Packed Powder-Bed during Selective Laser Melting of Inconel 718 Alloy,” Int J Mach Tools Manuf, **116**, pp. 96–106.

[20] Petkov, V. I., 2018, *Alloy 718 Manufactured by AM Selective Laser Melting Evaluation of Microstructure and Weldability*.

[21] Zhang, Y. N., Cao, X., Wanjara, P., and Medraj, M., 2013, “Oxide Films in Laser Additive Manufactured Inconel 718,” Acta Mater, **61**(17), pp. 6562–6576.

[22] Zhao, Y., Guan, K., Yang, Z., Hu, Z., Qian, Z., Wang, H., and Ma, Z., 2020, “The Effect of Subsequent Heat Treatment on the Evolution Behavior of Second Phase Particles and Mechanical Properties of the Inconel 718 Superalloy Manufactured by Selective Laser Melting,” Materials Science and Engineering A, **794**.

[23] Huang, L., Cao, Y., Zhang, J., Gao, X., Li, G., and Wang, Y., 2021, “Effect of Heat Treatment on the Microstructure Evolution and Mechanical Behaviour of a Selective Laser Melted Inconel 718 Alloy,” J Alloys Compd, **865**.

[24] Zhang, D., Niu, W., Cao, X., and Liu, Z., 2015, “Effect of Standard Heat Treatment on the Microstructure and Mechanical Properties of Selective Laser Melting Manufactured Inconel 718 Superalloy,” Materials Science and Engineering A, **644**, pp. 32–40.

[25] Cao, M., Zhang, D., Gao, Y., Chen, R., Huang, G., Feng, Z., Poprawe, R., Schleifenbaum, J. H., and Ziegler, S., 2021, “The Effect of Homogenization Temperature on the Microstructure and High Temperature Mechanical Performance of SLM-Fabricated IN718 Alloy,” Materials Science and Engineering A, **801**.

[26] Huang, W., Yang, J., Yang, H., Jing, G., Wang, Z., and Zeng, X., 2019, “Heat Treatment of Inconel 718 Produced by Selective Laser Melting: Microstructure and Mechanical Properties,” Materials Science and Engineering A, **750**, pp. 98–107.

[27] Fayed, E. M., Shahriari, D., Saadati, M., Brailovski, V., Jahazi, M., and Medraj, M., 2020, “Influence of Homogenization and Solution Treatments Time on the Microstructure and Hardness of Inconel 718 Fabricated by Laser Powder Bed Fusion Process,” Materials, **13**(11).

[28] Popovich, V. A., Borisov, E. v., Popovich, A. A., Sufiiarov, V. S., Masaylo, D. v., and Alzina, L., 2017, “Impact of Heat Treatment on Mechanical Behaviour of Inconel 718 Processed with Tailored Microstructure by Selective Laser Melting,” Mater Des, **131**, pp. 12–22.

[29] Mostafa, A., Rubio, I. P., Brailovski, V., Jahazi, M., and Medraj, M., 2017, “Structure, Texture and Phases in 3D Printed IN718 Alloy Subjected to Homogenization and HIP Treatments,” Metals (Basel), **7**(6).

[30] Amato, K. N., Gaytan, S. M., Murr, L. E., Martinez, E., Shindo, P. W., Hernandez, J., Collins, S., and Medina, F., 2012, “Microstructures and Mechanical Behavior of Inconel 718 Fabricated by Selective Laser Melting,” Acta Mater, **60**(5), pp. 2229–2239.

[31] Periane, S., Duchosal, A., Vaudreuil, S., Chibane, H., Morandeau, A., Anthony Xavior, M., and Leroy, R., 2021, “Influence of Heat Treatment on the Fatigue Resistance of Inconel 718 Fabricated by Selective Laser Melting (SLM),” *Materials Today: Proceedings*, Elsevier Ltd, pp. 7860–7865.

[32] Wan, H. Y., Zhou, Z. J., Li, C. P., Chen, G. F., and Zhang, G. P., 2018, “Enhancing Fatigue Strength of Selective Laser Melting-Fabricated Inconel 718 by Tailoring Heat Treatment Route,” Adv Eng Mater, **20**(10).

[33] “Luvak Laboratories” [Online]. Available: https://www.luvak.com/. [Accessed: 19-Aug-2020].

[34] Chlebus, E., Gruber, K., Kuźnicka, B., Kurzac, J., and Kurzynowski, T., 2015, “Effect of Heat Treatment on the Microstructure and Mechanical Properties of Inconel 718 Processed by Selective Laser Melting,” Materials Science and Engineering A, **639**, pp. 647–655.

[35] Miao, Z. J., Shan, A. D., Wu, Y. B., Lu, J., Xu, W. L., and Song, H. W., 2011, “Quantitative Analysis of Homogenization Treatment of INCONEL718 Superalloy,” Transactions of Nonferrous Metals Society of China (English Edition), **21**(5), pp. 1009–1017.

[36] Sohrabi, M. J., Mirzadeh, H., and Rafiei, M., 2018, “Solidification Behavior and Laves Phase Dissolution during Homogenization Heat Treatment of Inconel 718 Superalloy,” Vacuum, **154**, pp. 235–243.

[37] Schirra, J. J., 1997, *Effect of Heat Treatment Variations on the Hardness and Mechanical Properties of Wrought Inconel 718*.

[38] Baufeld, B., 2012, “Mechanical Properties of INCONEL 718 Parts Manufactured by Shaped Metal Deposition (SMD),” J Mater Eng Perform, **21**(7), pp. 1416–1421.

[39] Brenne, F., Taube, A., Pröbstle, M., Neumeier, S., Schwarze, D., Schaper, M., and Niendorf, T., 2016, “Microstructural Design of Ni-Base Alloys for High-Temperature Applications: Impact of Heat Treatment on Microstructure and Mechanical Properties after Selective Laser Melting,” Progress in Additive Manufacturing, **1**(3–4), pp. 141–151.

[40] Deng, D., Peng, R. L., Brodin, H., and Moverare, J., 2018, “Microstructure and Mechanical Properties of Inconel 718 Produced by Selective Laser Melting: Sample Orientation Dependence and Effects of Post Heat Treatments,” Materials Science and Engineering A, **713**, pp. 294–306.

[41] Sui, S., Tan, H., Chen, J., Zhong, C., Li, Z., Fan, W., Gasser, A., and Huang, W., 2019, “The Influence of Laves Phases on the Room Temperature Tensile Properties of Inconel 718 Fabricated by Powder Feeding Laser Additive Manufacturing,” Acta Mater, **164**, pp. 413–427.

[42] Pei, C., Shi, D., Yuan, H., and Li, H., 2019, “Assessment of Mechanical Properties and Fatigue Performance of a Selective Laser Melted Nickel-Base Superalloy Inconel 718,” Materials Science and Engineering A, **759**, pp. 278–287.

APPENDIX A

POROSITY

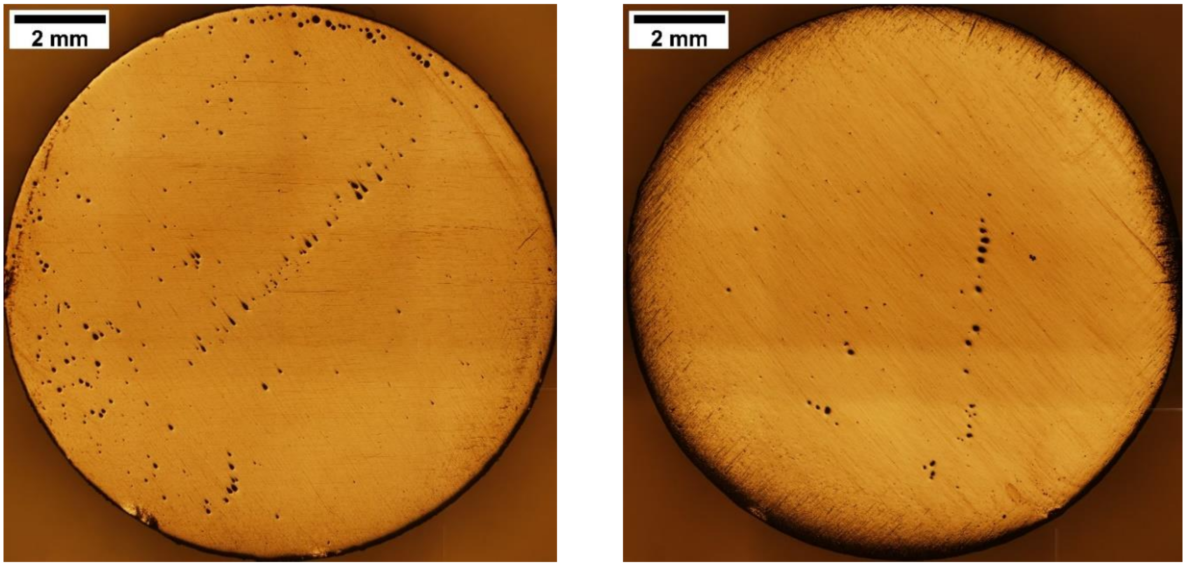

a) b)

Figure 5.1 Surface porosity of A samples (45.5 J/mm^3) a) A2 and b) A4

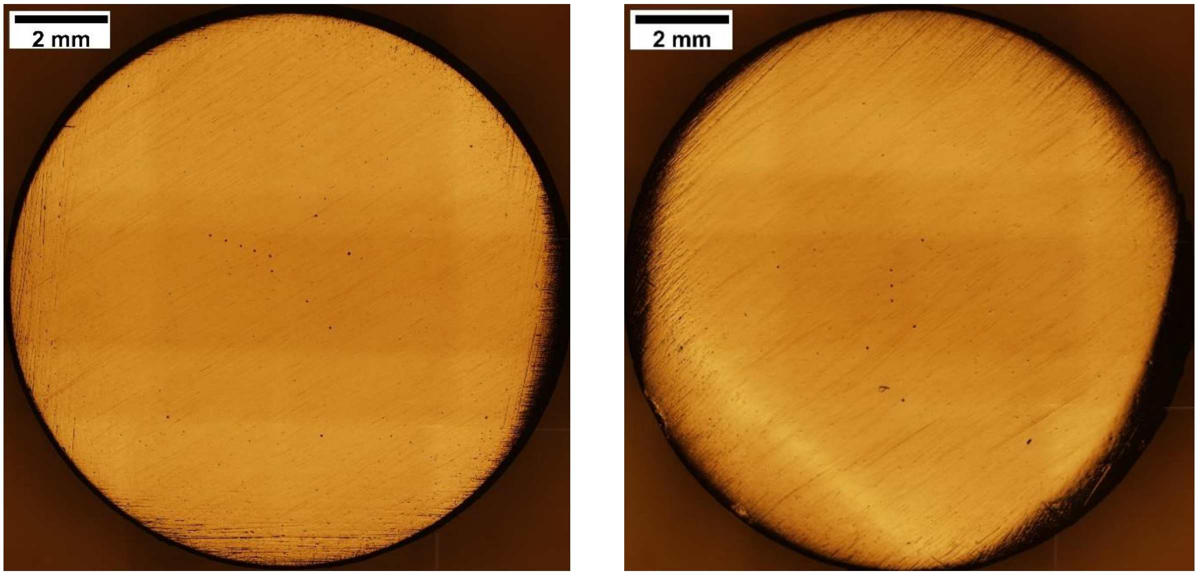

a) b)

Figure 5.2 Surface porosity of A samples (45.5 J/mm^3) a) A6 and b) A8

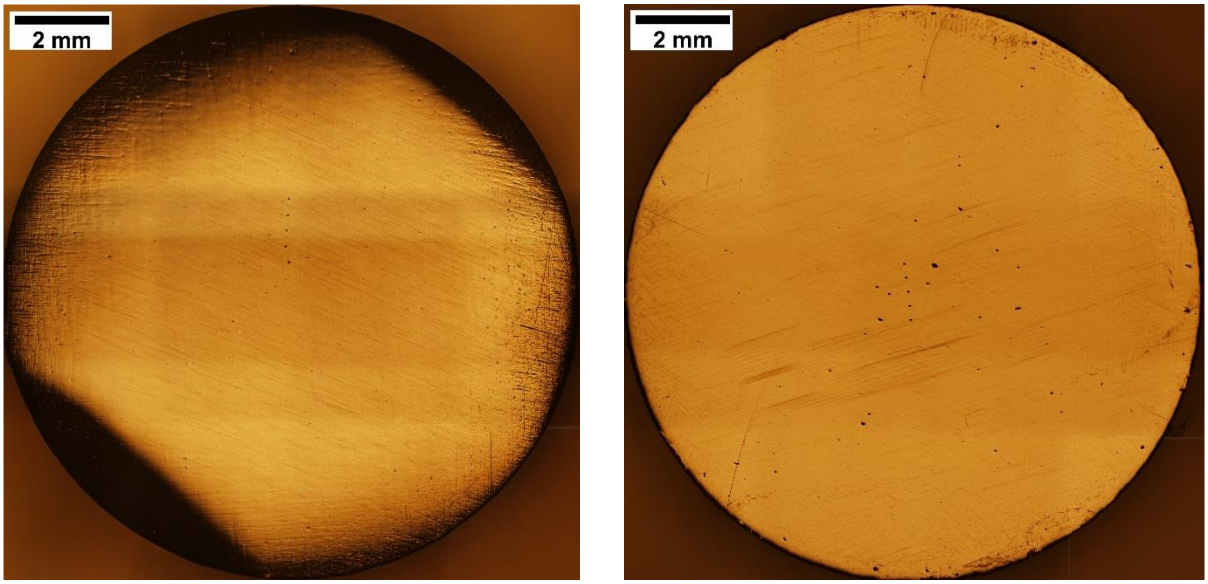

a) **b)**

Figure 5.3 Surface porosity of a) sample A12 (45.5 J/mm^3) and b) sample B2 (54.5 J/mm^3)

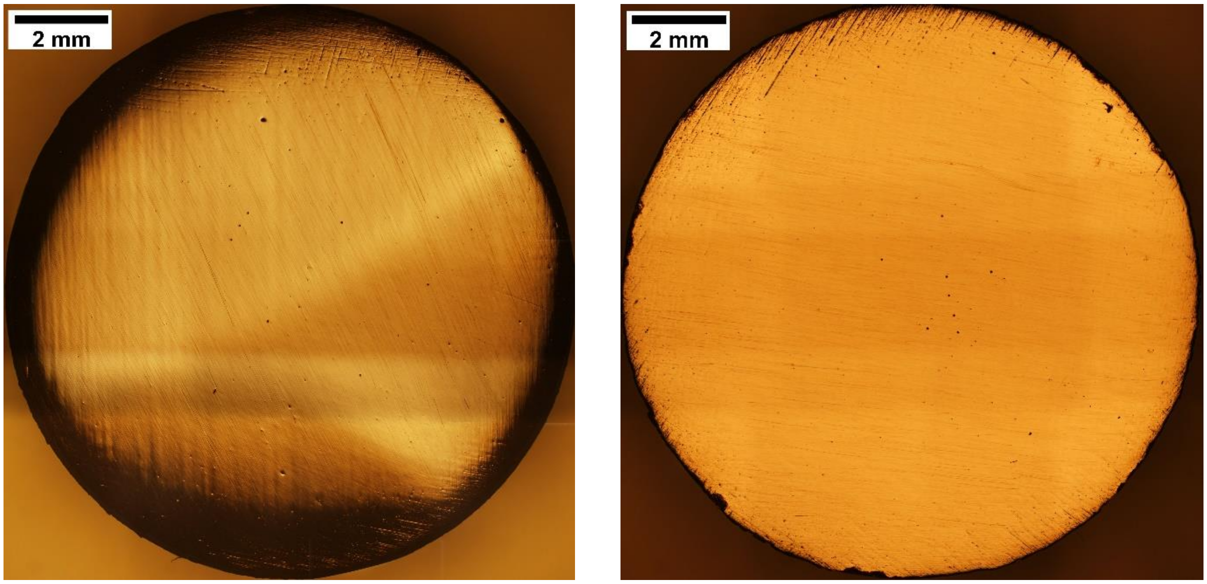

a) **b)**

Figure 5.4 Surface porosity of B samples (54.5 J/mm^3) a) B4 and b) B6

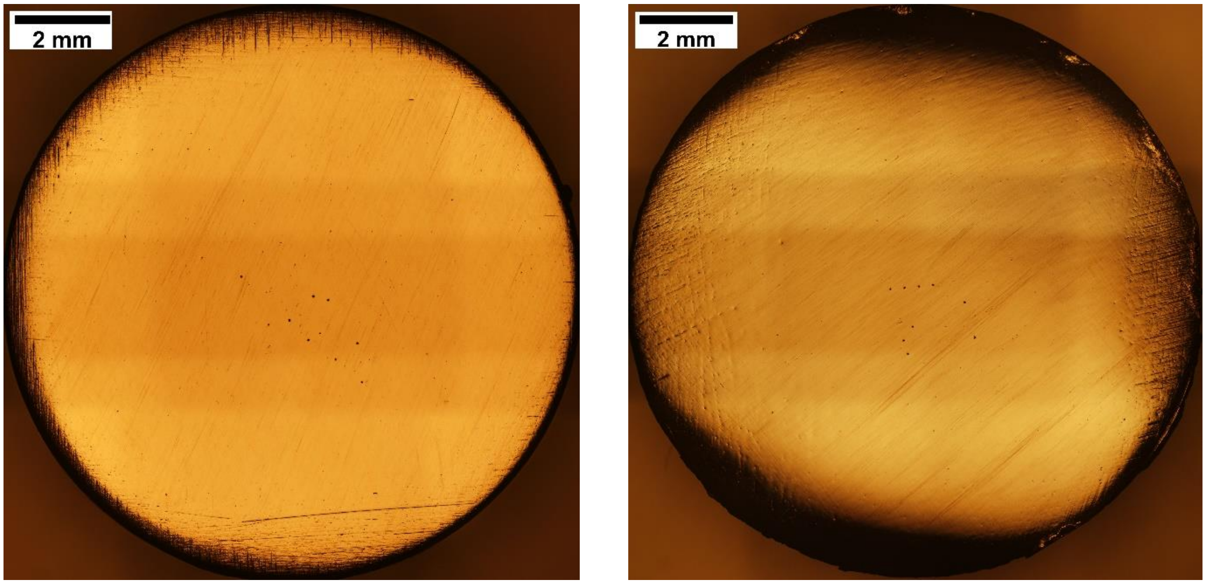

a) b)

Figure 5.5 Surface porosity of B samples (54.5 J/mm^3) a) B8 and b) B10

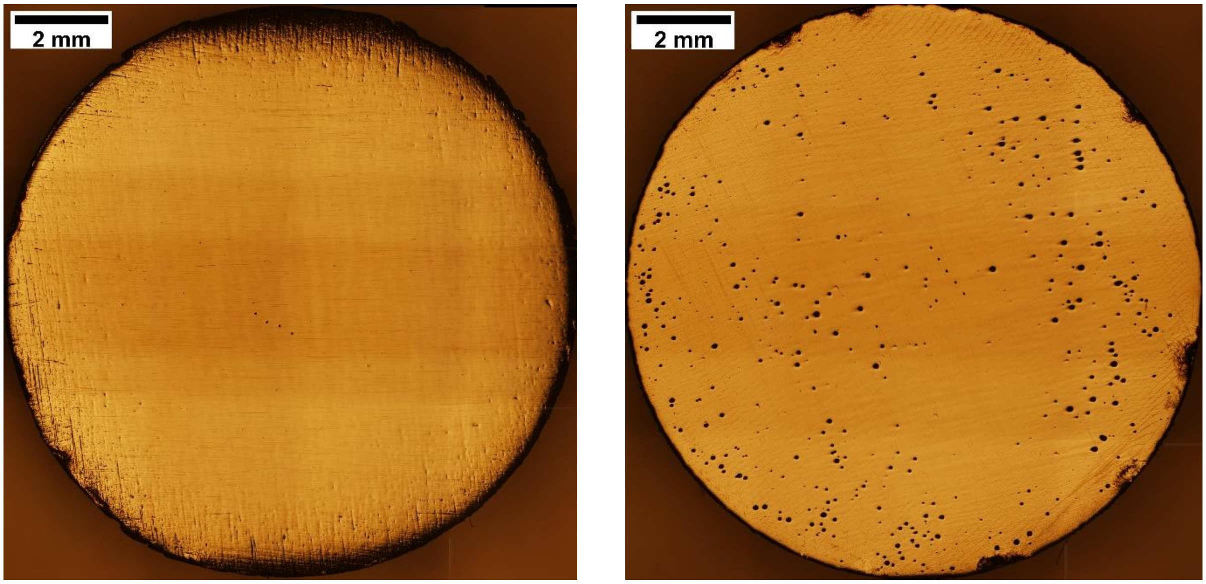

a) b)

Figure 5.6 Surface porosity of a) sample B12 (54.5 J/mm^3) and b) sample C2 (68.2 J/mm^3)

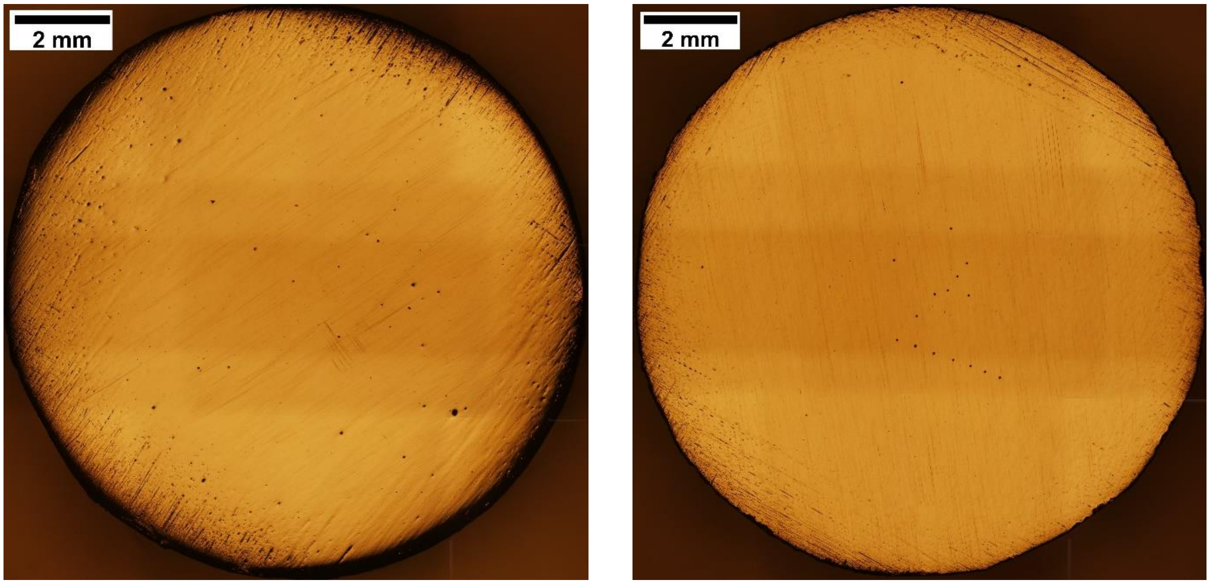

a) **b)**

Figure 5.7 Surface porosity of C samples (68.2 J/mm^3) a) C4 and b) C6

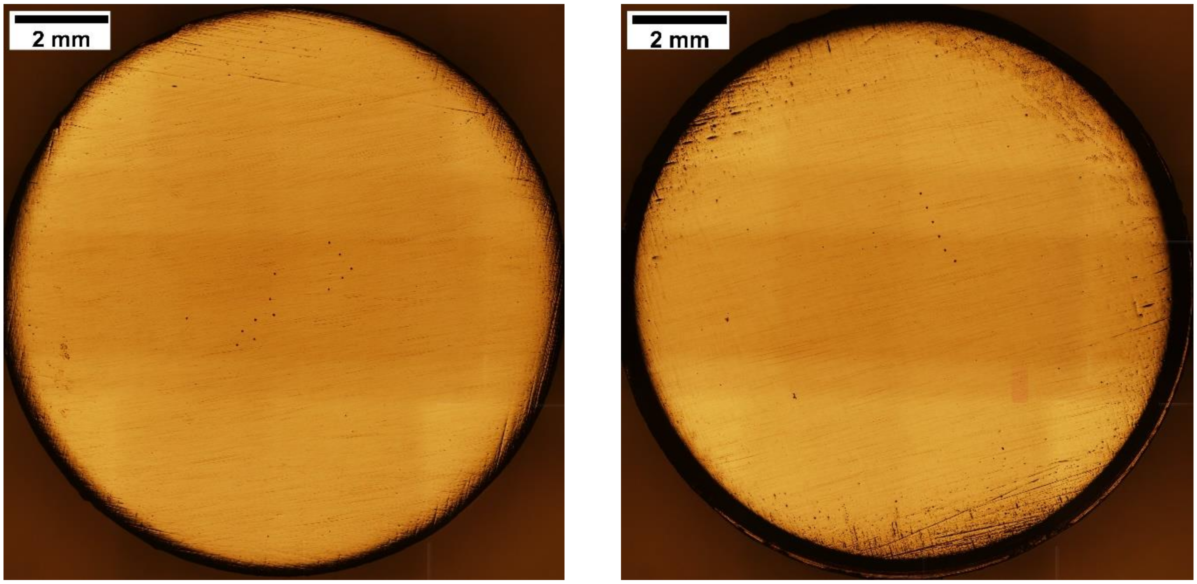

a) **b)**

Figure 5.8 Surface porosity for C samples (68.2 J/mm^3) a) C8 and b) C12

APPENDIX B

HARDNESS

Table 5.1 Complete Hardness Data

Sample	Energy Density (J/mm^3)	Heat Treatment Strategy	Hardness Values			
			Microhardness, HV	Mean, HV	Rockwel l B	Mean, RB
A1	45.5	As Printed	322.9 386.4 346.3	351.9 ± 18.5	89.3 92.0 91.7	91.0 ± 0.9
A2	45.5	As Printed	383.2 385.3 399.2	389.2 ± 5.0	91.1 91.4 88.2	90.2 ± 1.0
A3	45.5	Homogenization	400.1 436.7 418.2	418.3 ± 10.6	88.3 86.9 90.2	88.5 ± 1.0
A4	45.5	Homogenization	365.7 358.7 346.3	356.9 ± 5.7	89.9 90.7 89.2	89.9 ± 0.4
A5	45.5	Homogenization + HIP	498.7 501.5 510.4	503.5 ± 3.5	90.4 93.2 94.6	92.7 ± 1.2
A6	45.5	Homogenization + HIP	483.2 498.8 477.3	486.4 ± 6.4	96.4 98.0 96.8	97.1 ± 0.5
A7	45.5	Homogenization + HIP + Solution Aging	454.1 444.1 469.4	455.9 ± 7.4	104.5 105.9 107.2	105.9 ± 0.8
A8	45.5	Homogenization + HIP + Solution Aging	467.8 469.4 446.8	461.3 ± 7.3	106.3 107.1 107.0	106.8 ± 0.3

Table 5.1 Complete Hardness Data (Continued)

A9	45.5	HIP	428.9	430.9 ± 1.7	91.0	90.6 ± 0.3
			434.2		90.7	
			429.6		90.0	
A10	45.5	HIP	481.7	485.5 ± 6.4	95.2	96.6 ± 0.8
			476.9		98.1	
			497.9		96.4	
A11	45.5	HIP + Solution Aging	454.9	453.7 ± 5.2	107.2	106.9 ± 0.7
			462.0		108.0	
			444.2		105.6	
A12	45.5	HIP + Solution Aging	452.1	446.6 ± 6.2	108.3	108.2 ± 0.1
			453.6		108.2	
			434.2		108.1	
B1	54.5	As Printed	332.7	342.0 ± 5.3	94.0	96.2 ± 1.1
			350.9		97.7	
			342.4		96.8	
B2	54.5	As Printed	309.8	325.8 ± 9.5	91.5	92.5 ± 0.5
			342.6		93.0	
			325.1		93.0	
B3	54.5	Homogenization	335.7	348.8 ± 6.6	92.8	93.1 ± 0.9
			356.6		91.6	
			354.2		94.8	
B4	54.5	Homogenization	421.4	420.9 ± 3.2	94.1	92.9 ± 0.6
			415.2		92.6	
			426.1		92.1	
B5	54.5	Homogenization + HIP	457.1	460.0 ± 3.1	98.2	97.8 ± 0.8
			456.7		96.2	
			466.2		99.0	
B6	54.5	Homogenization + HIP	361.7	367.8 ± 4.7	97.2	97.0 ± 0.6
			364.8		98.0	
			377.0		95.8	

Table 5.1 Complete Hardness Data (Continued)

B7	54.5	Homogenization + HIP + Solution Aging	487.5 469.0 477.2	477.9 ± 5.4	108.0 109.2 110.8	109.3 ± 0.8
B8	54.5	Homogenization + HIP + Solution Aging	448.4 463.0 462.7	458.0 ± 5.8	107.0 109.2 108.1	108.1 ± 0.6
B9	54.5	HIP	501.5 507.3 504.7	504.5 ± 1.7	95.0 94.2 91.9	93.7 ± 0.9
B10	54.5	HIP	414.2 415.3 435.3	421.6 ± 6.9	95.2 94.5 92.2	94.0 ± 0.9
B11	54.5	HIP + Solution Aging	479.0 459.0 475.9	471.3 ± 6.2	106.9 109.1 108.8	108.3 ± 0.7
B12	54.5	HIP + Solution Aging	419.1 421.4 419.9	420.1 ± 0.7	104.9 103.6 107.0	105.2 ± 1.0
C1	68.2	As Printed	346.6 348.5 332.7	342.6 ± 5.0	89.0 88.6 91.2	89.6 ± 0.8
C2	68.2	As Printed	335.9 334.7 326.9	332.5 ± 2.8	89.6 90.3 93.0	91.0 ± 1.0
C3	68.2	Homogenization	376.5 350.1 380.0	368.9 ± 9.4	89.3 90.7 87.1	89.0 ± 1.0
C4	68.2	Homogenization	436.4 409.8 429.9	425.4 ± 8.0	89.4 92.5 91.2	91.0 ± 0.9

Table 5.1 Complete Hardness Data (Continued)

C5	68.2	Homogenization + HIP	459.9	466.5 ± 4.0	93.4	93.3 ± 0.7
			465.9		92.1	
			473.6		94.4	
C6	68.2	Homogenization + HIP	457.0	461.8 ± 4.5	91.2	92.5 ± 0.6
			457.7		93.1	
			470.8		93.1	
C7	68.2	Homogenization + HIP + Solution Aging	482.5	484.1 ± 2.8	99.9	99.4 ± 0.3
			489.6		99.0	
			480.3		99.4	
C8	68.2	Homogenization + HIP + Solution Aging	506.9	496.4 ± 7.9	108.0	106.9 ± 1.0
			481.0		105.0	
			501.4		107.7	
C9	68.2	HIP	366.0	366.6 ± 0.8	93.0	93.0 ± 0.9
			365.6		93.5	
			368.3		92.6	
C10	68.2	HIP	469.0	467.8 ± 3.8	95.1	94.9 ± 0.8
			473.8		93.5	
			460.7		96.1	
C11	68.2	HIP + Solution Aging	521.7	510.1 ± 7.3	110.9	109.6 ± 1.0
			512.1		110.2	
			496.6		107.6	
C12	68.2	HIP + Solution Aging	466.3	453.8 ± 10.5	108.8	107.4 ± 0.7
			432.9		107.0	
			462.2		106.4	

APPENDIX C

MICROGRAPHS

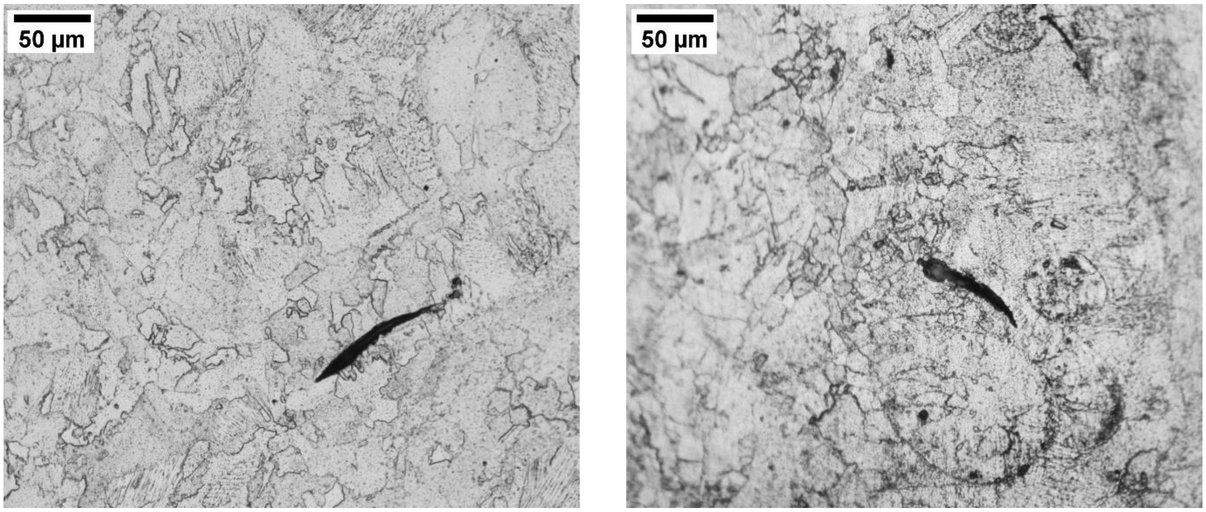

a) **b)**

Figure 5.9 Void defects in AP samples a) A1 and b) B1

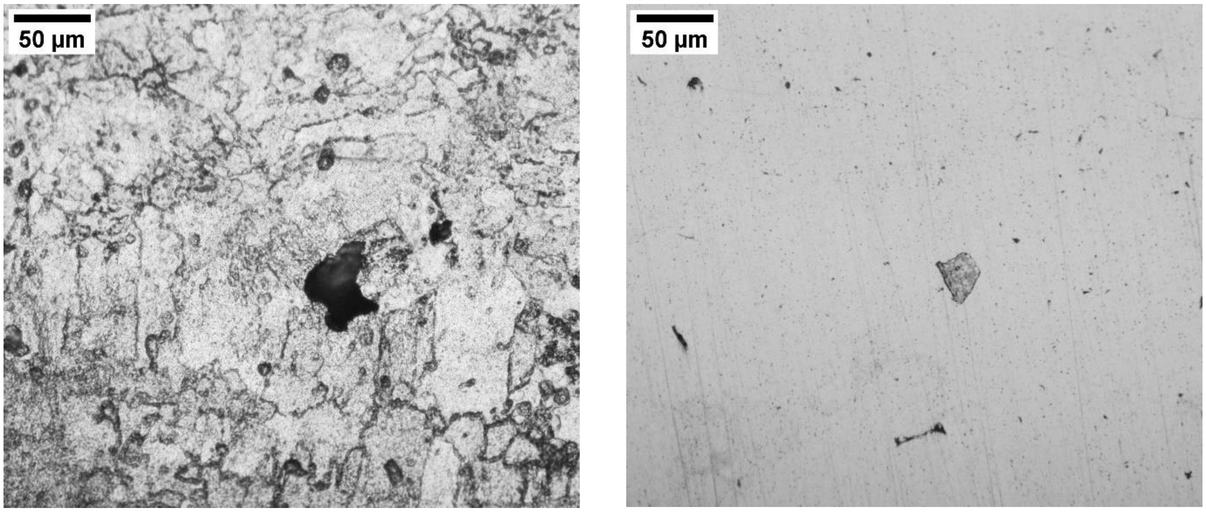

a) **b)**

Figure 5.10 a) Void defect and b) surface defect in AP B1 sample

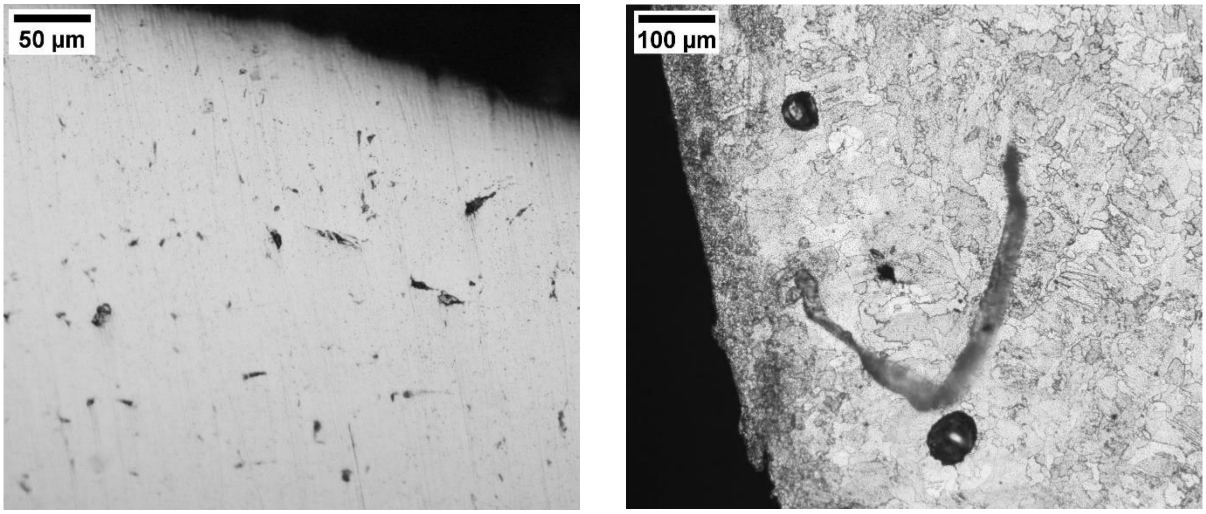

a) b)

Figure 5.11 a) Surface defects and b) large void and pore defects in AP B1 sample

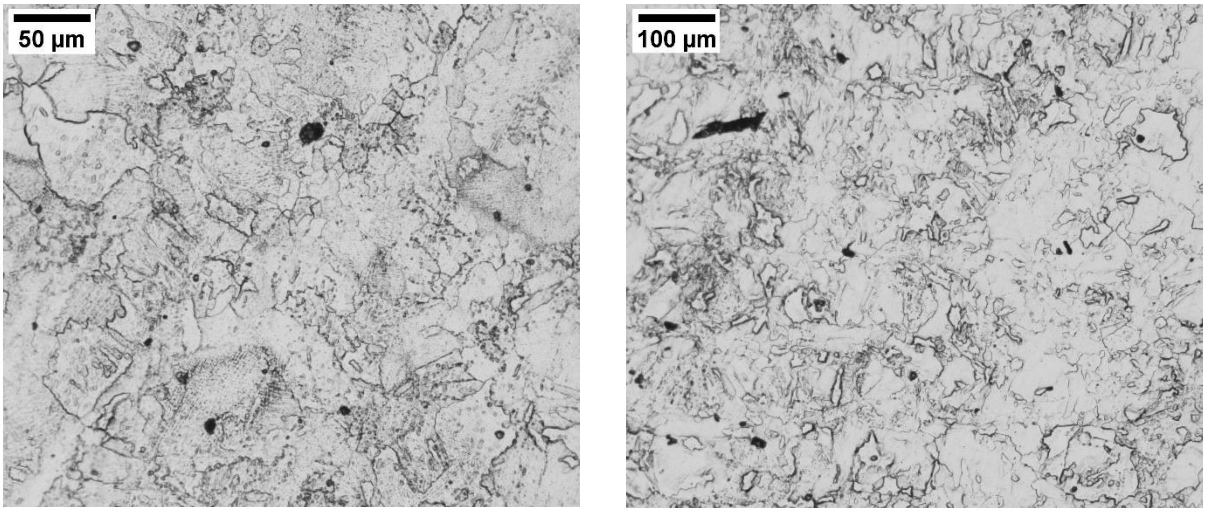

a) b)

Figure 5.12 a) Pore defects in AP C1 sample and b) multiple void defects in HG A3 sample

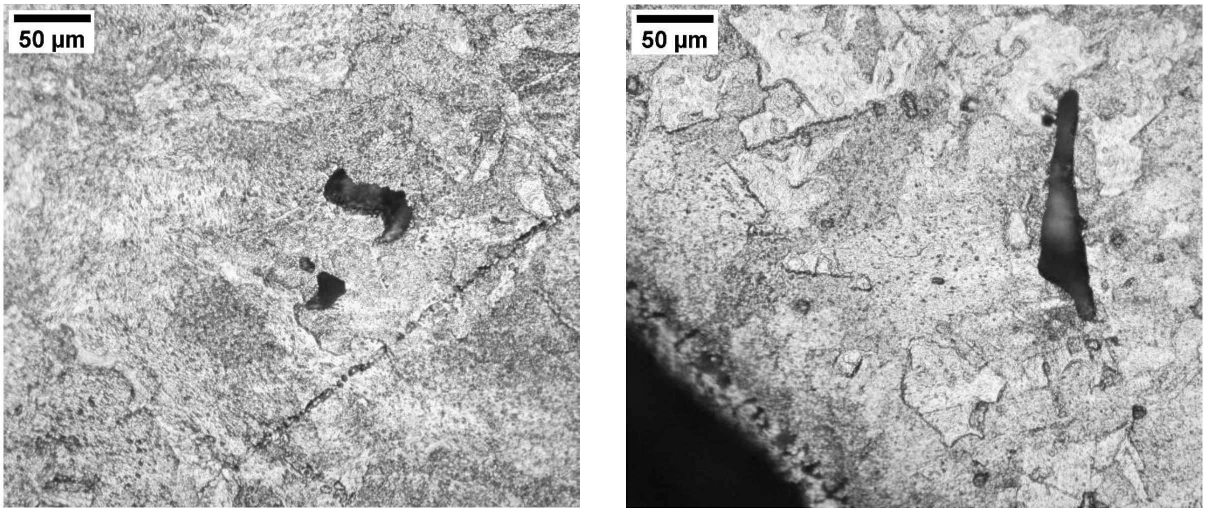

a) b)

Figure 5.13 Void defects in HG B3 sample

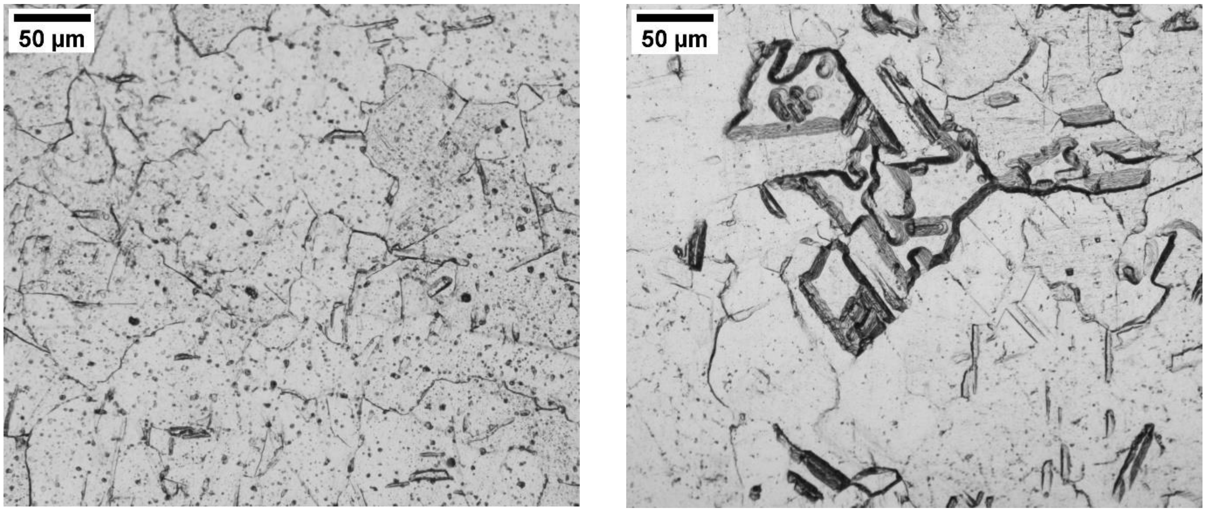

a) b)

Figure 5.14 a) Etch spot staining on HG+HIP A5 sample and b) uneven grain boundaries in over-etched HG+HIP B5 sample

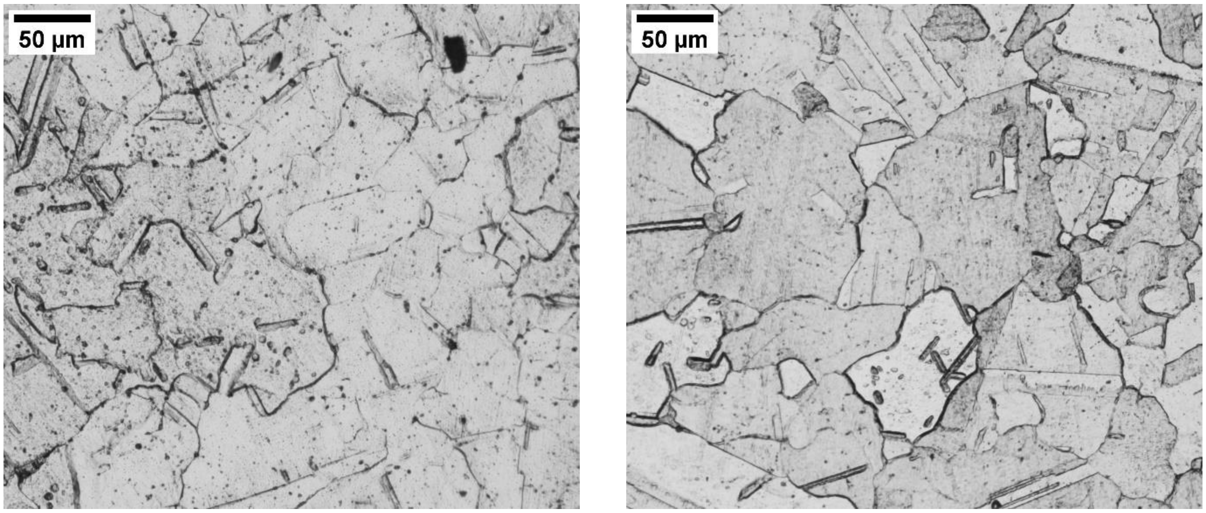

a) b)

Figure 5.15 a) Grain boundaries and large void defect in HG+HIP B5 sample and b) grain boundary development in HG+HIP+SA A7 sample

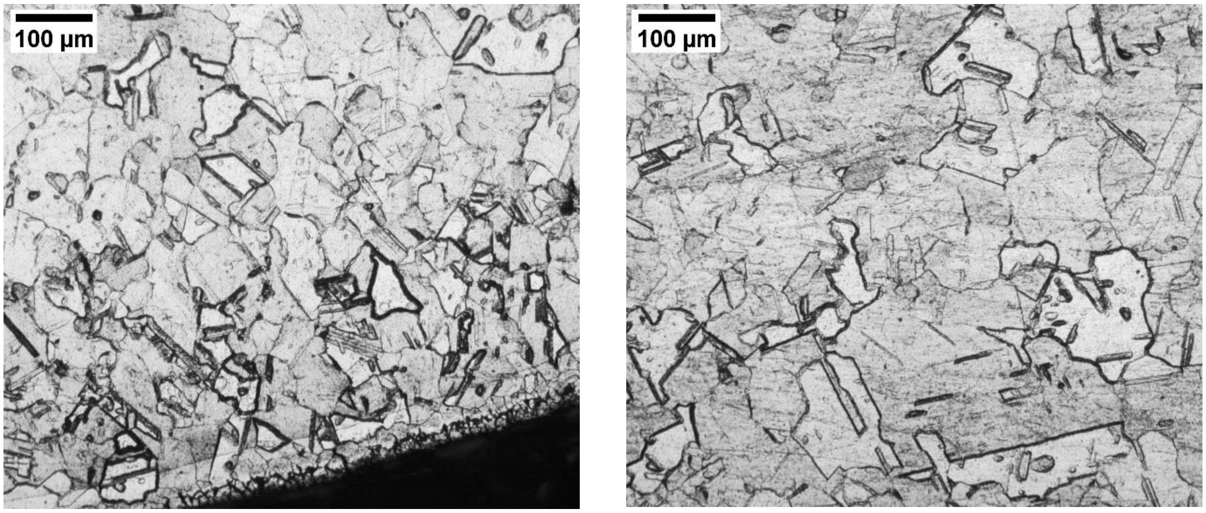

a) b)

Figure 5.16 Uneven grain boundaries in over-etched region of HG+HIP+SA B7 sample

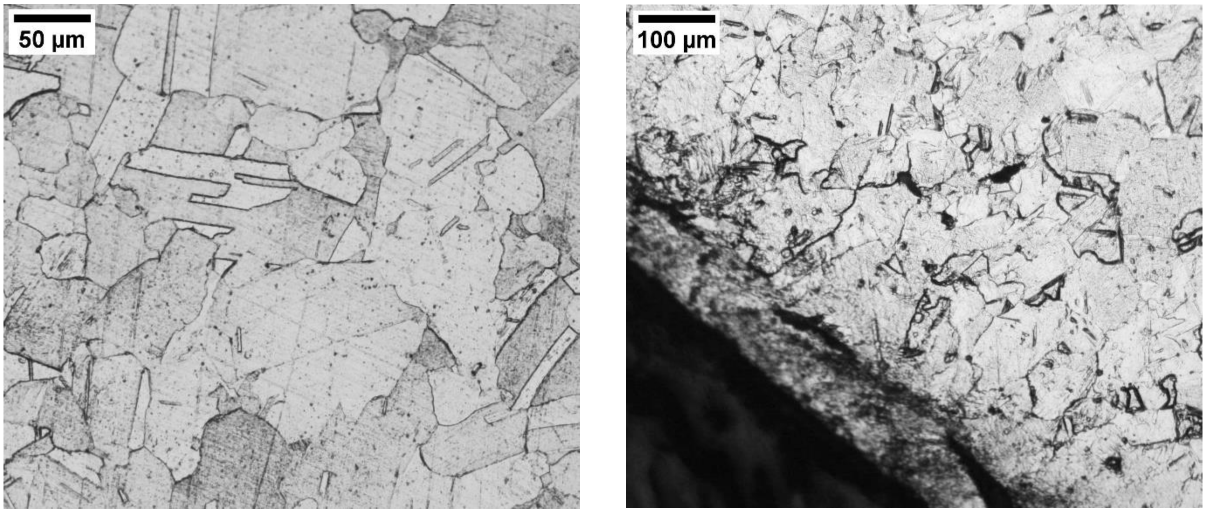

a) b)

Figure 5.17 a) grain boundaries in HG+HIP+SA C7 sample and b) void defects in over-etched region of HIP B9 sample

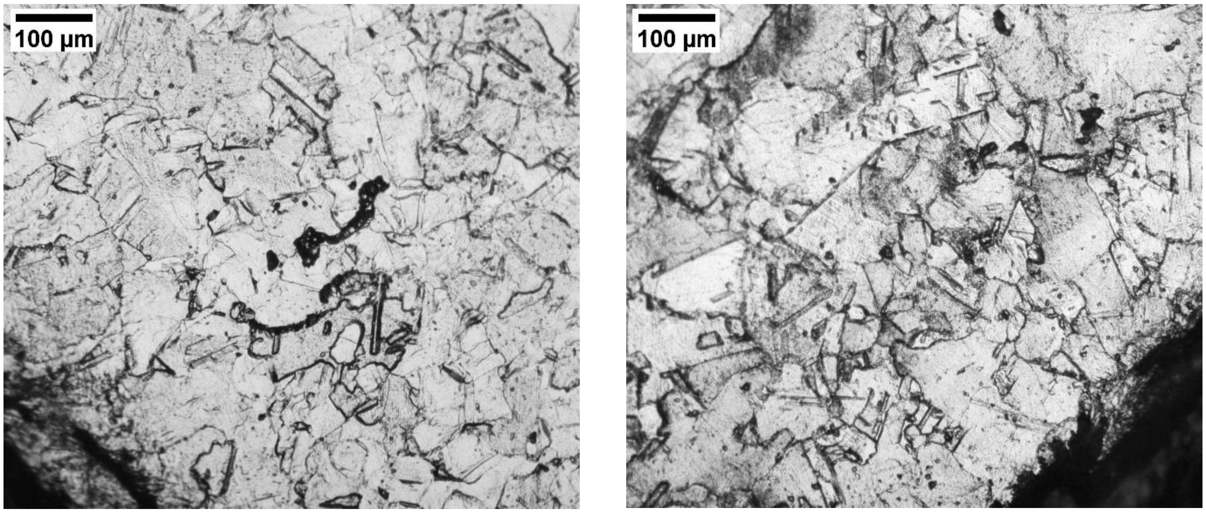

a) b)

Figure 5.18 Void defects in over-etched region of a) HIP B9 sample and b) HIP+SA B11 sample

APPENDIX D

SCANNING ELECTRON MICROSCOPY

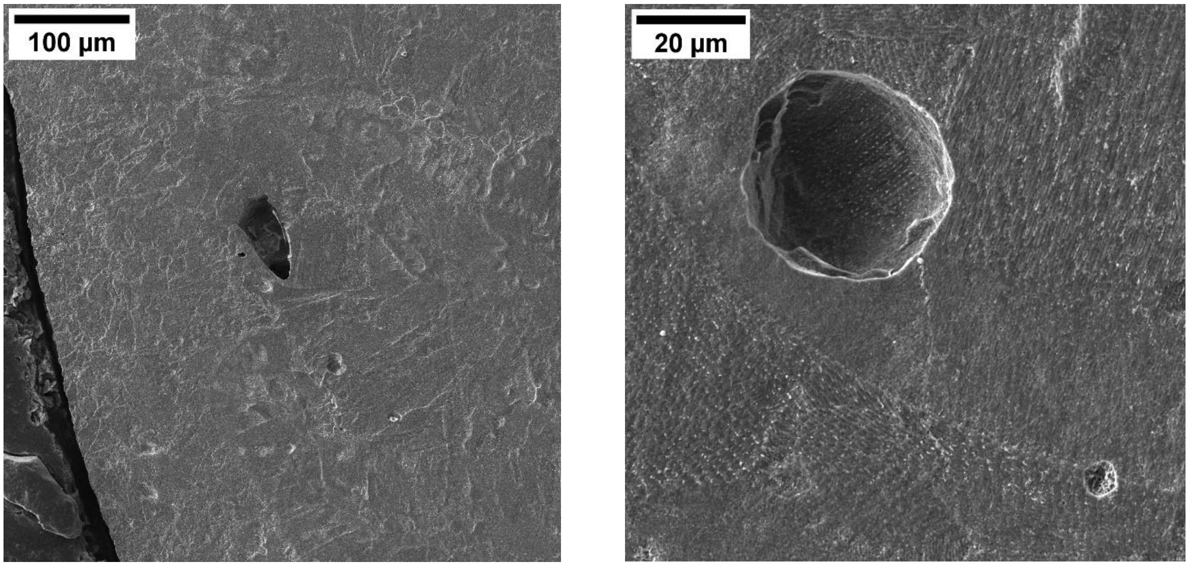

a) b)

Figure 5.19 Void defects in AP sample B1 (54.5 J/mm^3)

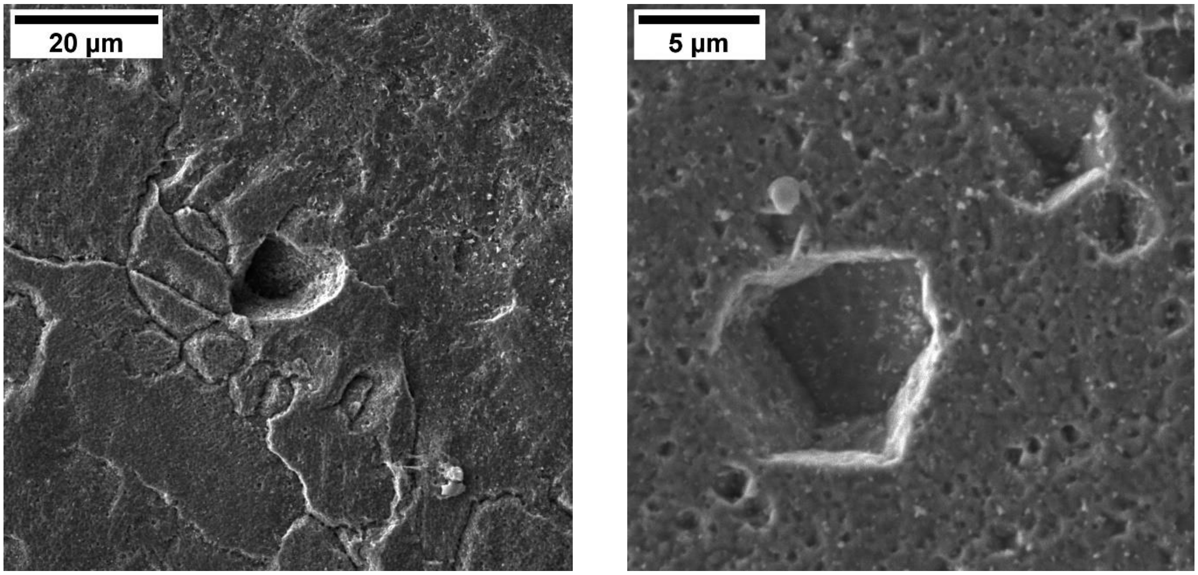

a) b)

Figure 5.20 Void defects in AP sample B1 (54.5 J/mm^3)

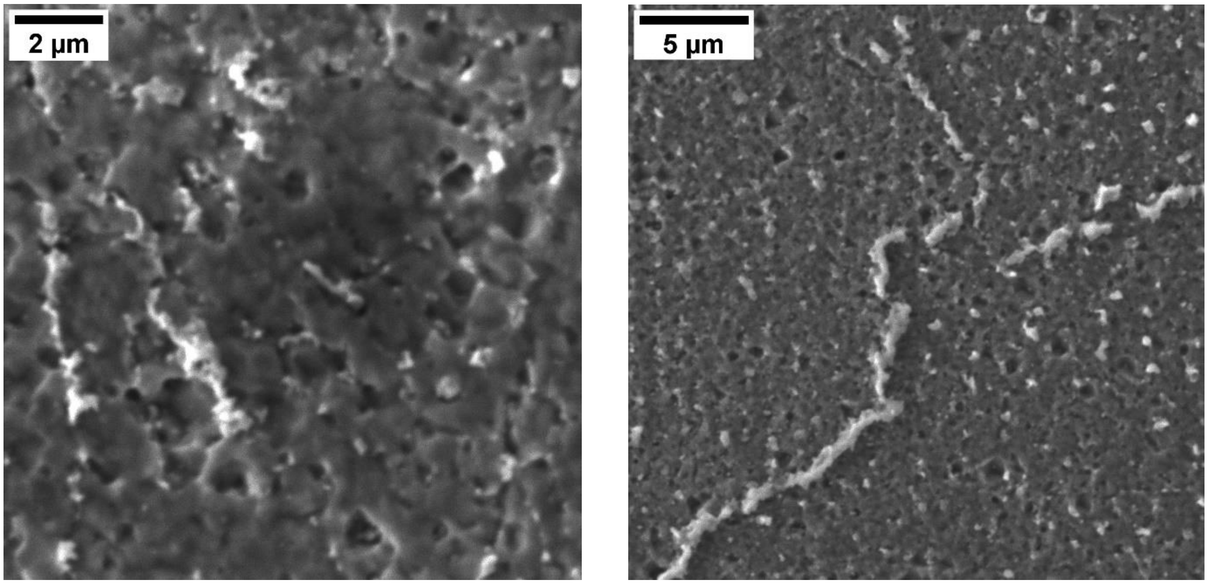

a) b)

Figure 5.21 Laves phase particles in AP sample B1 (54.5 J/mm^3)

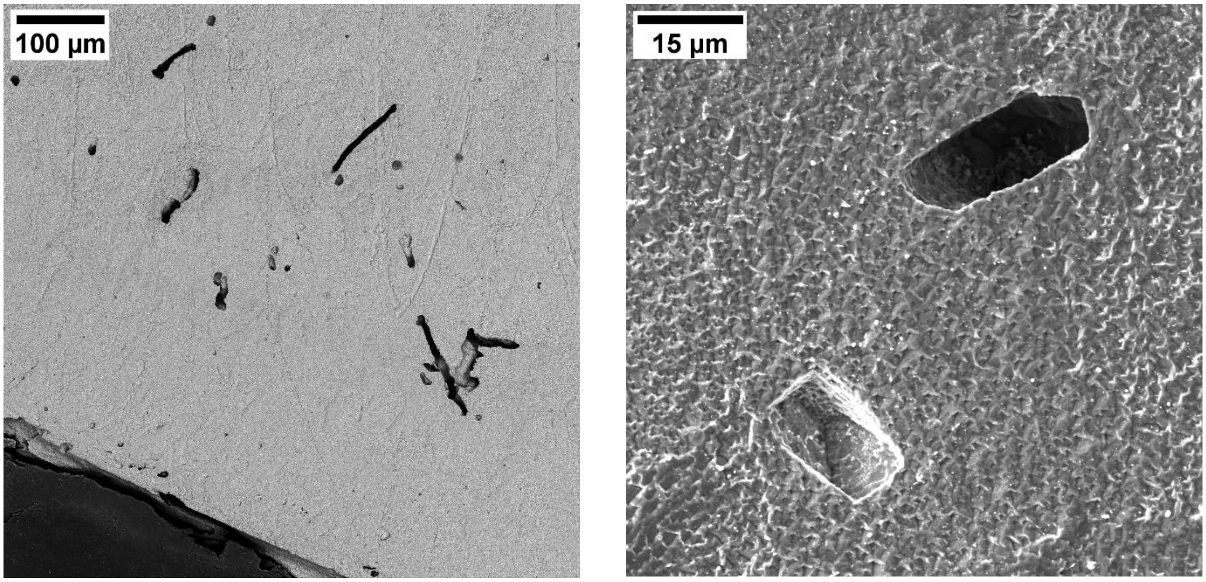

a) b)

Figure 5.22 Void defects in HG sample B3 (54.5 J/mm^3)

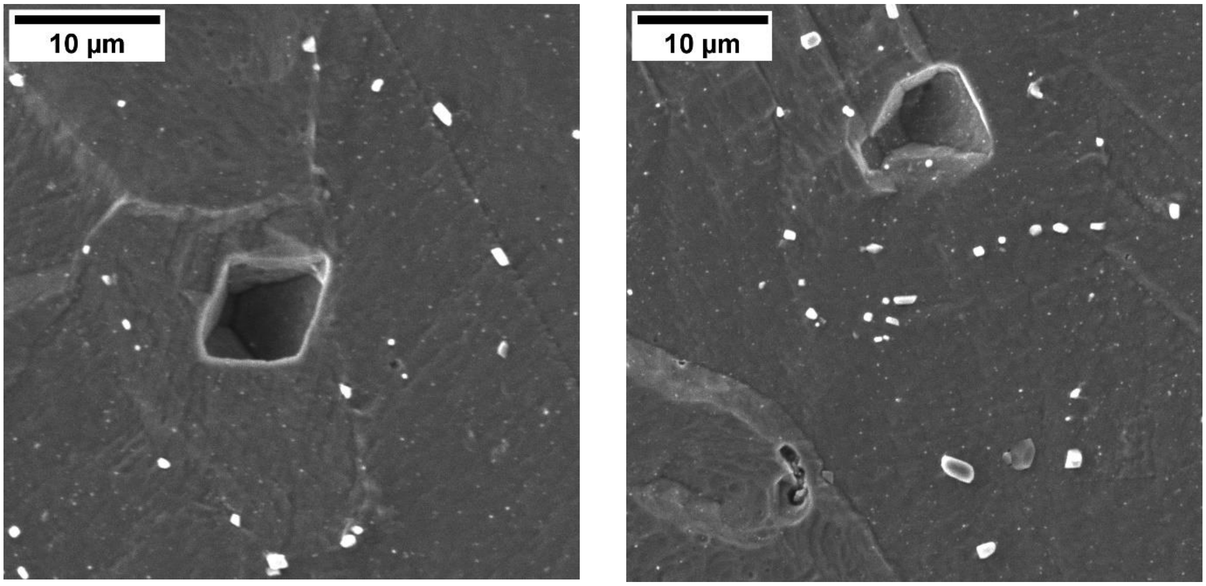

a) b)

Figure 5.23 Void defects and Nb-rich carbide distribution in HG+HIP sample B5 (54.5 J/mm^3)

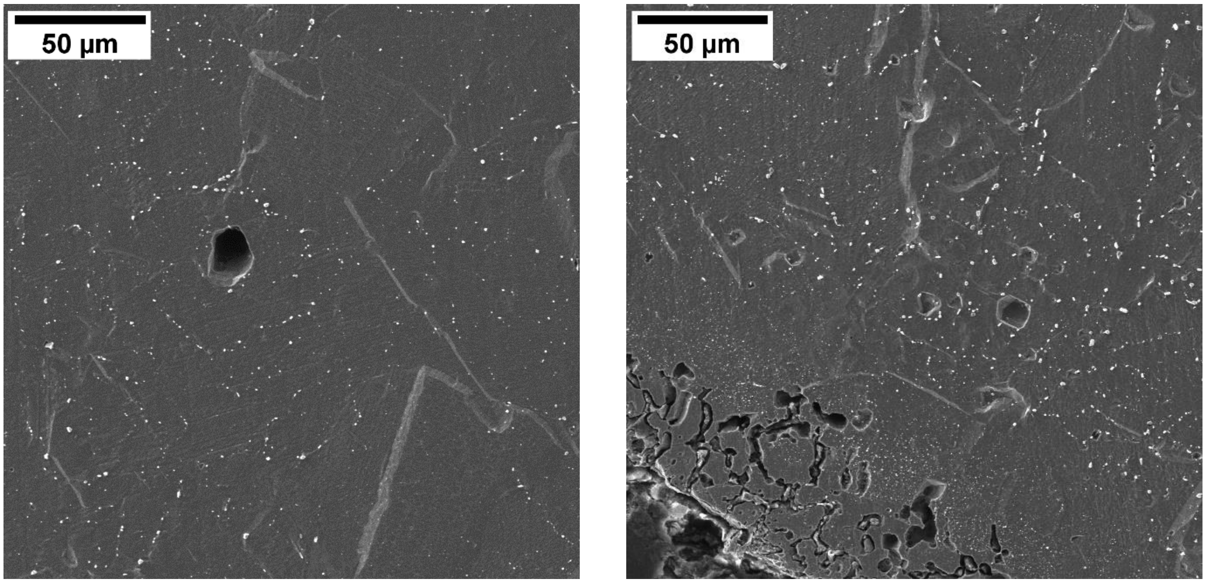

a) b)

Figure 5.24 Void defects and Nb-rich carbide distribution in HG+HIP sample B5 (54.5 J/mm^3)

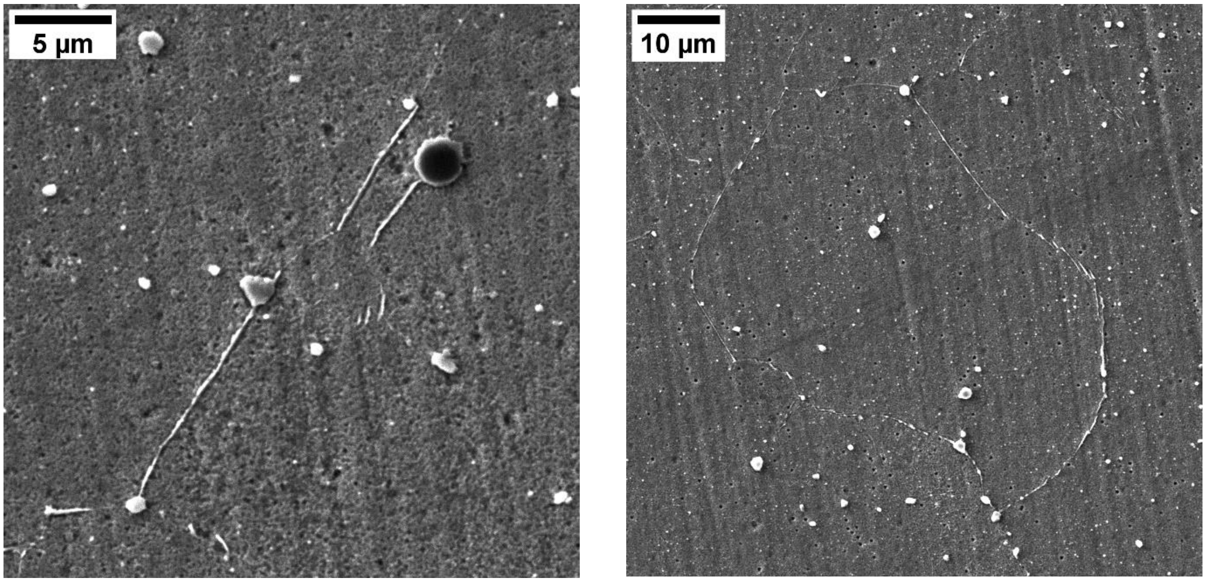

a) b)

Figure 5.25 Carbide and delta phase distribution in HG+HIP+SA sample B7 (54.5 J/mm^3)

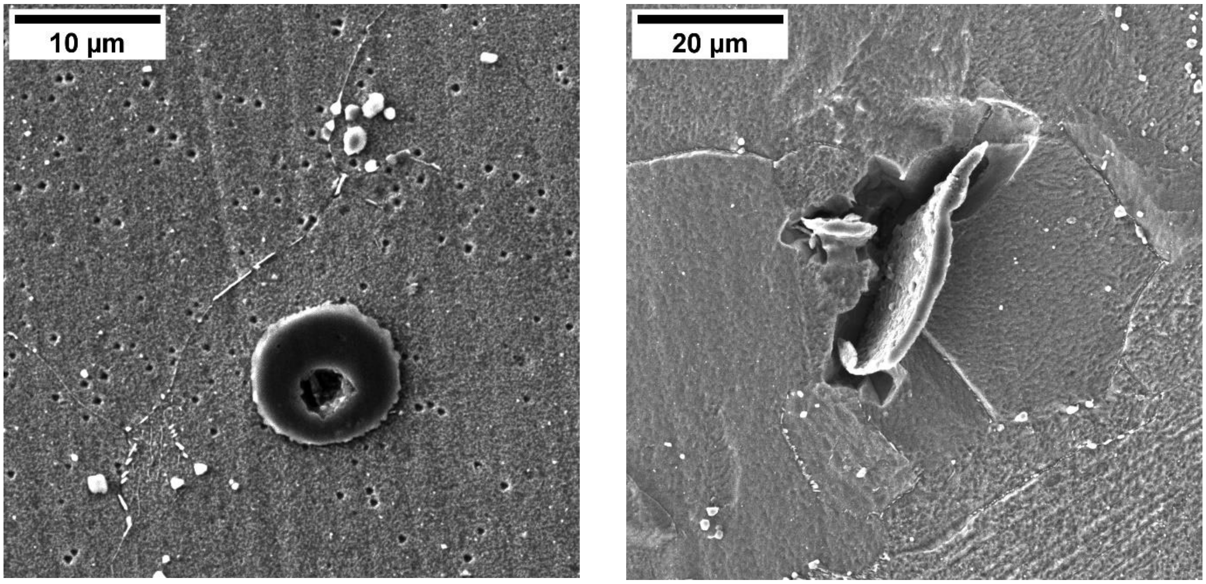

a) b)

Figure 5.26 Carbide, delta phase, and Al-oxide defects present in HG+HIP+SA sample B7 (54.5 J/mm^3)

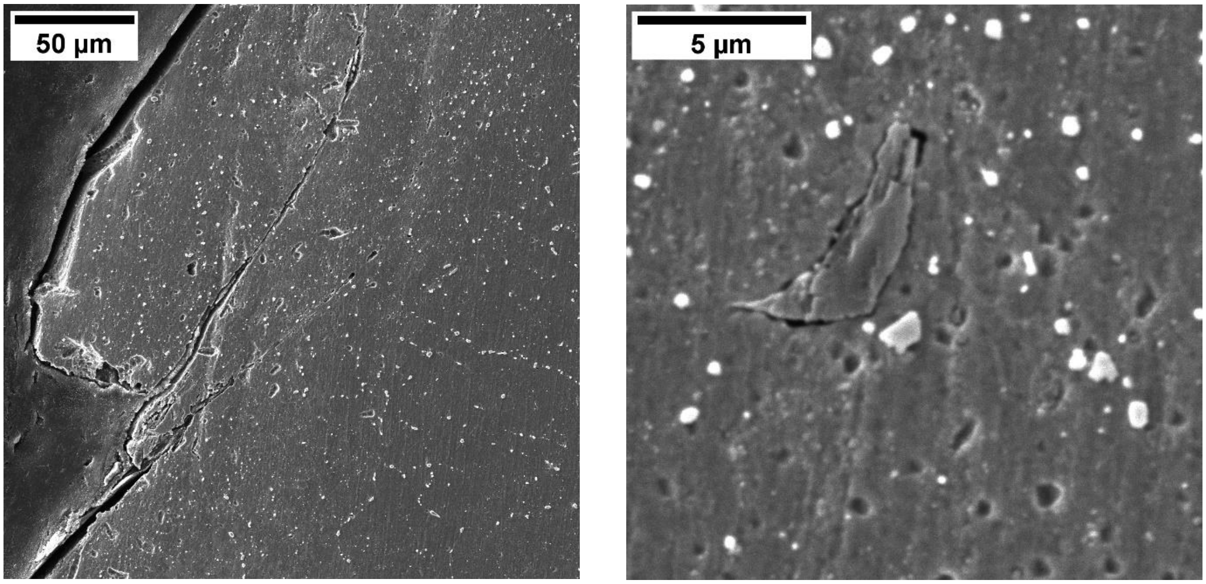

a) b)

Figure 5.27 Carbide distribution in HIP sample B9 (54.5 J/mm^3)

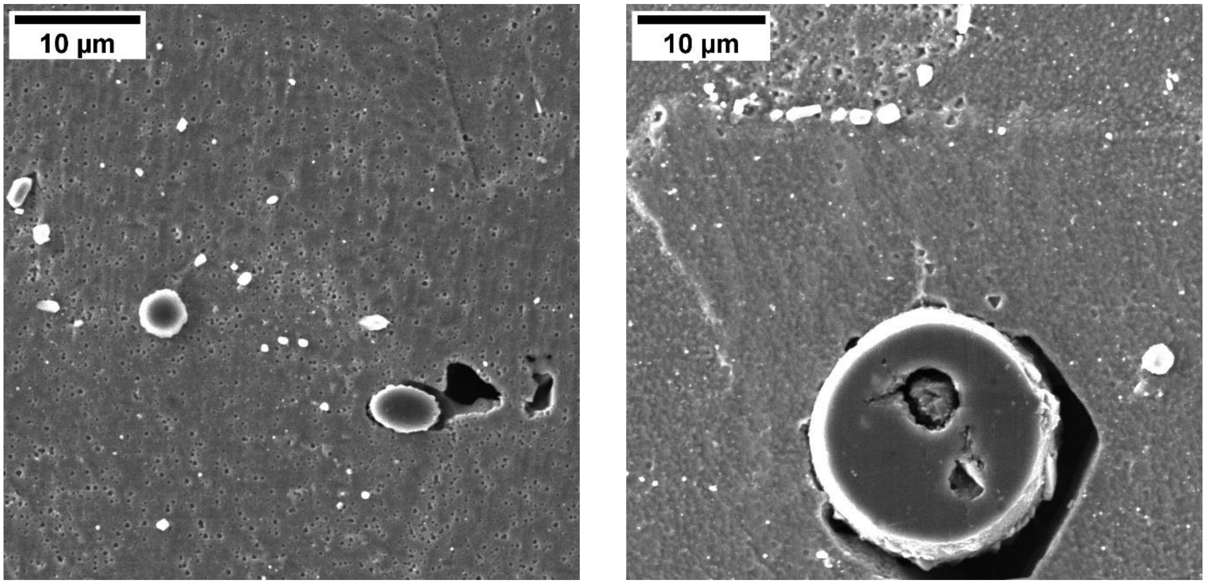

a) b)

Figure 5.28 Carbide distribution and Al-oxide defects in HIP sample B9 (54.5 J/mm^3)

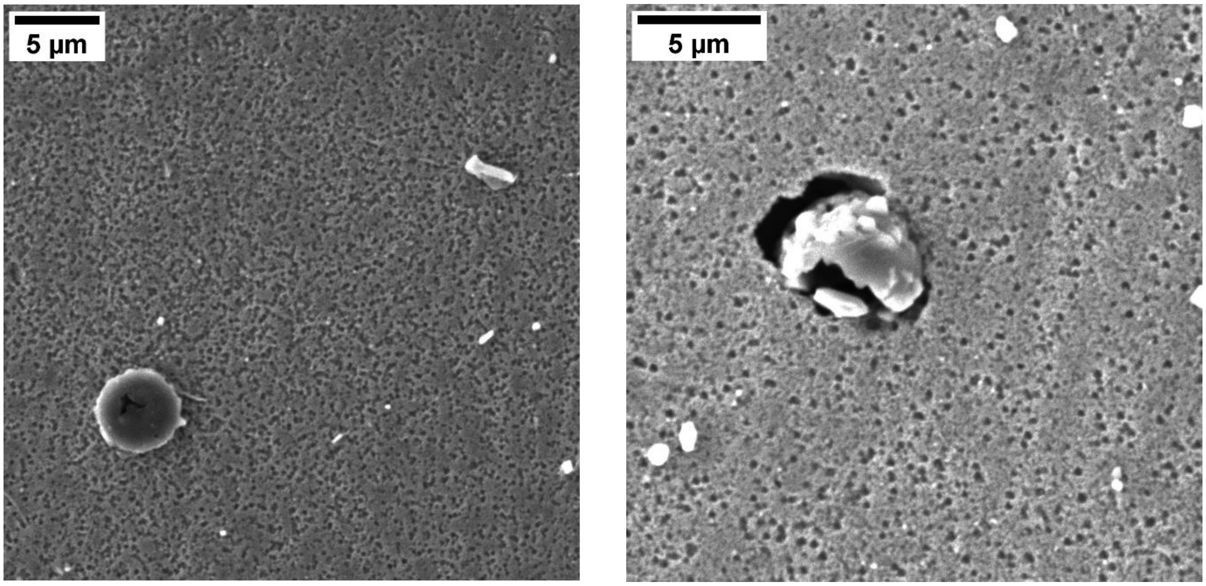

a) **b)**

Figure 5.29 Al-oxide and carbide distribution in HIP+SA sample B11 (54.5 J/mm^3)

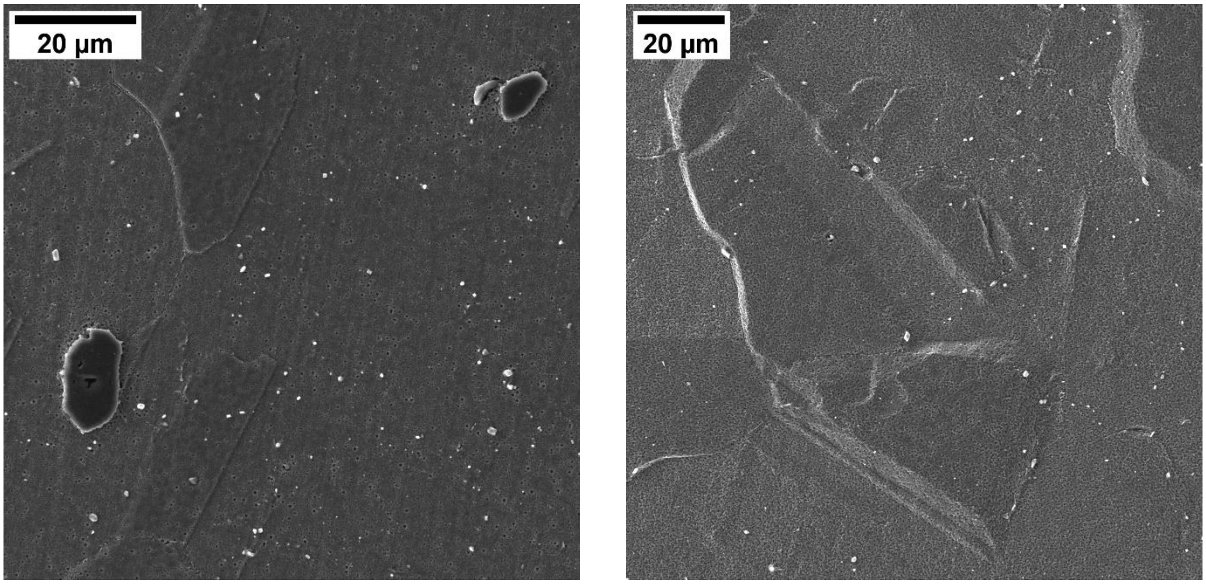

a) **b)**

Figure 5.30 HIP+SA sample B11 (54.5 J/mm^3) with a) Al-oxide defect and b) carbide distribution

APPENDIX E

ENERGY DISPERSIVE SPECTROSCOPY

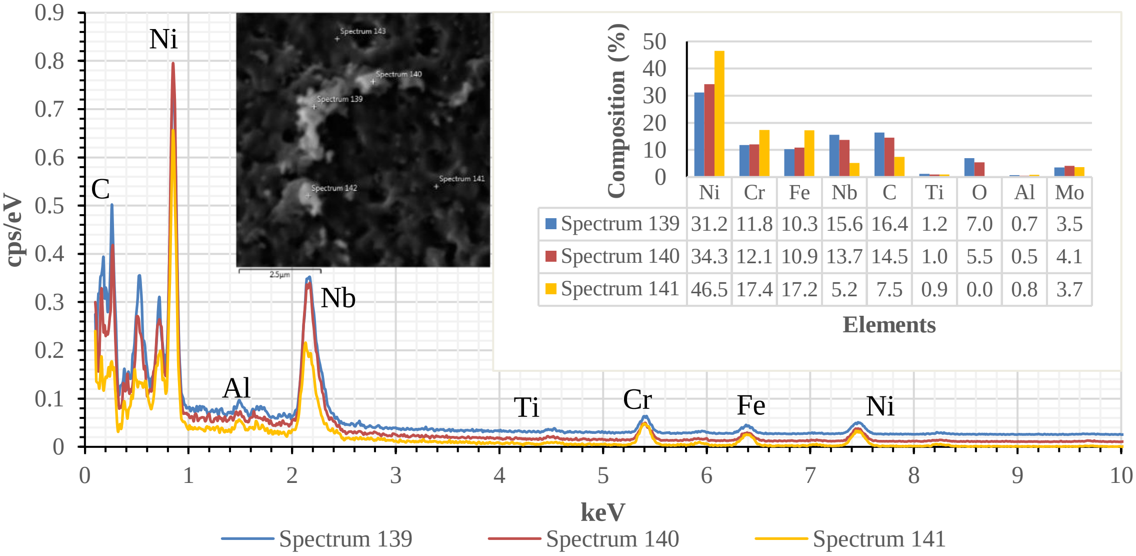

	Ni	Cr	Fe	Nb	C	Ti	O	Al	Mo
Spectrum 139	31.2	11.8	10.3	15.6	16.4	1.2	7.0	0.7	3.5
Spectrum 140	34.3	12.1	10.9	13.7	14.5	1.0	5.5	0.5	4.1
Spectrum 141	46.5	17.4	17.2	5.2	7.5	0.9	0.0	0.8	3.7

Figure 5.31 EDS of Laves phase in AP sample B1 (54.5 J/mm^3)

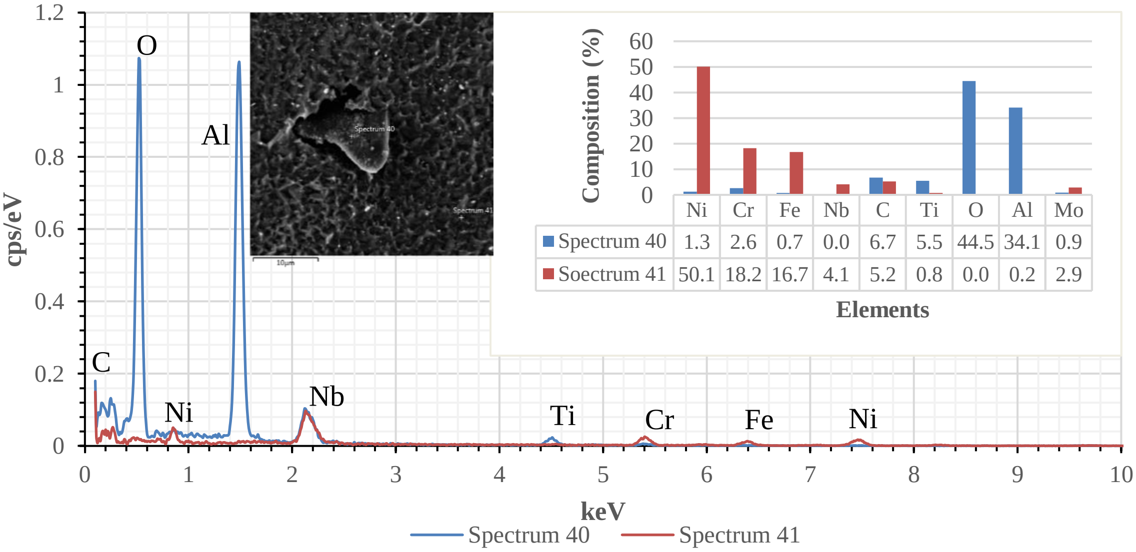

	Ni	Cr	Fe	Nb	C	Ti	O	Al	Mo
Spectrum 40	1.3	2.6	0.7	0.0	6.7	5.5	44.5	34.1	0.9
Soectrum 41	50.1	18.2	16.7	4.1	5.2	0.8	0.0	0.2	2.9

Figure 5.32 EDS of Al-oxide defect in HG sample B3 (54.5 J/mm^3)

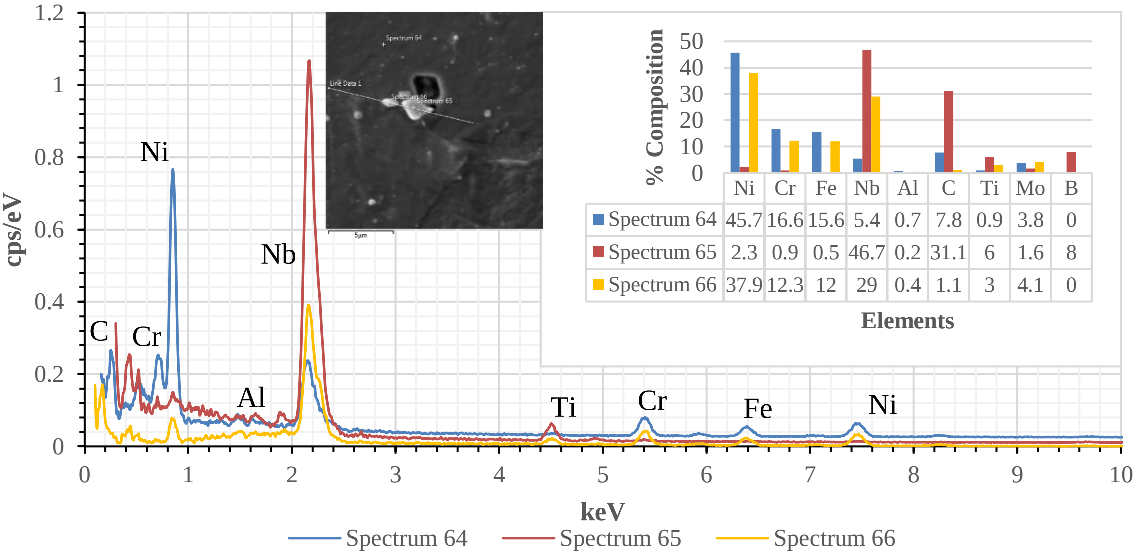

	Ni	Cr	Fe	Nb	Al	C	Ti	Mo	B
■ Spectrum 64	45.7	16.6	15.6	5.4	0.7	7.8	0.9	3.8	0
■ Spectrum 65	2.3	0.9	0.5	46.7	0.2	31.1	6	1.6	8
■ Spectrum 66	37.9	12.3	12	29	0.4	1.1	3	4.1	0

Figure 5.33 EDS of Nb-rich carbides in HG+HIP sample B5 (54.5 J/mm^3)

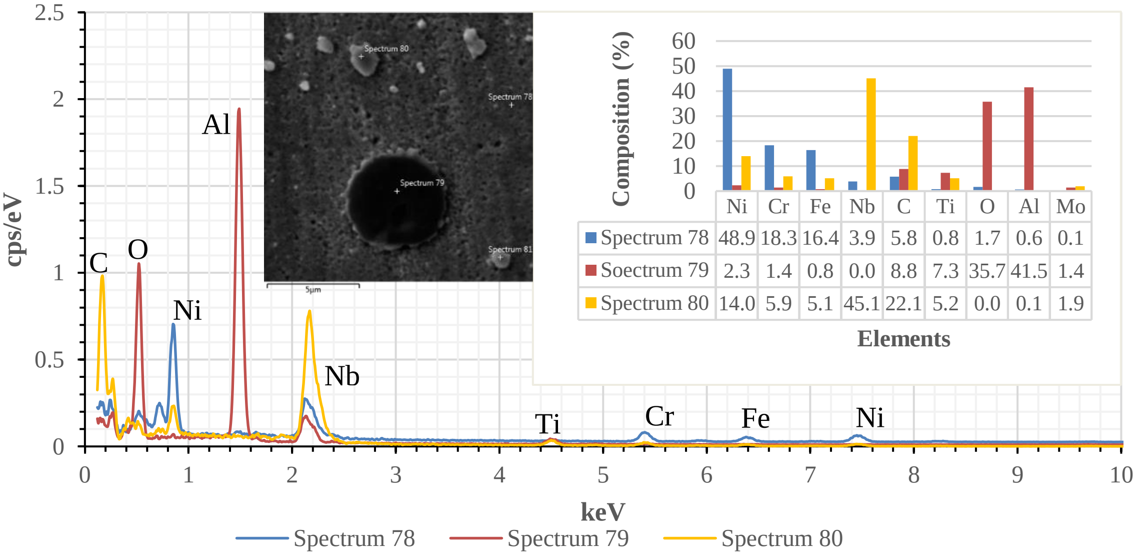

	Ni	Cr	Fe	Nb	C	Ti	O	Al	Mo
■ Spectrum 78	48.9	18.3	16.4	3.9	5.8	0.8	1.7	0.6	0.1
■ Soectrum 79	2.3	1.4	0.8	0.0	8.8	7.3	35.7	41.5	1.4
■ Spectrum 80	14.0	5.9	5.1	45.1	22.1	5.2	0.0	0.1	1.9

Figure 5.34 EDS of Al-oxide and carbides in HG+HIP+SA sample B7 (54.5 J/mm^3)

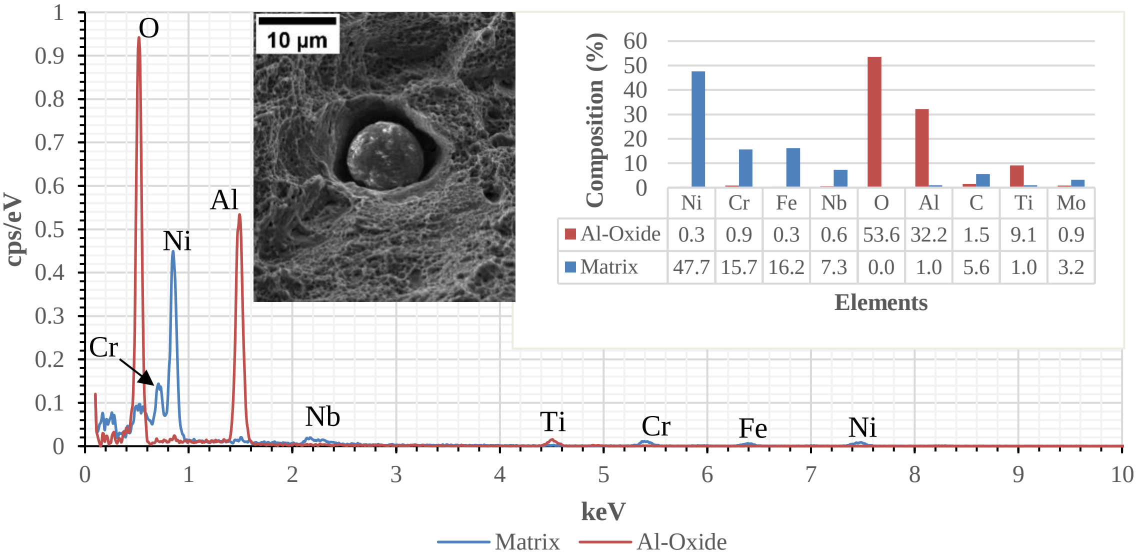

	Ni	Cr	Fe	Nb	O	Al	C	Ti	Mo
🟥 Al-Oxide	0.3	0.9	0.3	0.6	53.6	32.2	1.5	9.1	0.9
🟦 Matrix	47.7	15.7	16.2	7.3	0.0	1.0	5.6	1.0	3.2

Figure 5.35 EDS of Al-oxide defect in fatigue sample A12